Development and Fabrication of Silver Composite PEEK to Prevent Microbial Attachment and Periprosthetic Infection

A Dissertation

Submitted to the Faculty

of

Drexel University

by

David Joseph Jaekel

in partial fulfillment of the

requirements for the degree

of

Doctor of Philosophy

July 2012

Dedication

This dissertation is dedicated to my parents for always supporting my academic endeavors and making me the person I am today.

Acknowledgements

Special thanks to Dr. Noreen Hickok, Helen Davidson, and their lab at Thomas Jefferson University for their advice, assistance, and welcoming me with open arms.

I would also like to thank my adviser, Dr. Steven Kurtz, for his guidance and mentorship over the past 5 years. The lessons I have learned have built me into a better engineer.

Thanks to Dr. Marcolongo and her lab for helping with all of my early testing and providing instrumental support with my initial composite manufacturing.

I would also like to acknowledge Dr. Judd Day for constantly having his door open to discuss my research and always being a valued source of information and advice.

Thanks to my committee members, Dr. Greg Fridman, Dr. Kenneth Barbee, and Dr. Yinghui Zhong for their significant insight and constructive criticism that has greatly improved the quality the work performed.

Finally, I would like to thank everyone who has been a part of the Drexel Implant Research Center. In particular, my fellow graduate students, Dan MacDonald, Ryan Baxter, Doruk Baykal, and Steve Rundell who over the years have not only added support to my work but provided me with the most valuable ship there is, friendship.

Table of Contents

List of Tables

List of Figures

Dissertation Abstract

Development and Fabrication of Silver Composite PEEK to Prevent Microbial Attachment and Periprosthetic Infection
David Joseph Jaekel
Steven M. Kurtz, Ph.D.

Periprosthetic infection is a rare, yet devastating, and sometimes life-threatening complication to medical device implantation and is associated with increased hospital cost, length of hospitalization, and multiple surgical interventions. Since the early 1990s, the utilization of polyetheretherketone (PEEK) has been rising across the spine and orthopaedic industries, and therefore, their protection from infection becomes a high priority. Because Ag particulates have well-established antimicrobial properties and thermal stability, the feasibility of creating Ag-PEEK composites with nano-scale Ag (nanoAg), micro-scale porous Ag (μAg), and Ag-phosphate (Zr2K) particulates for infection control was examined. To analyze and predict Ag^+ release, an analytical model for the release of Ag^+ from the composite materials was also developed. The PEEK matrix was loaded with target filler ratios of 2, 5, and 10 w/w% of Ag particulate; however, particle aggregation occurred as well as lower than expected weight ratios were obtained. When Ag-loaded matrices with up to 5% Ag particulate were incubated with *S. aureus* or *E. coli*, no reduction in surface adherent bacteria was observed as measured by direct counting. When filler ratios were increased to 10%, significant reduction ($p \leq 0.03$) occurred in approximately 5 out of 12 trials for each filler type. In Ag elution trials, nanoAg and μAg PEEK composites sustained linear and long-term release of Ag at inhibitory concentrations for *S. Aureus* and

E. Coli. Zr2k composites released Ag rapidly within the first 48 hr; however, release decreased quickly beyond 96 hours. Ag^+ elution profiles were much lower than model predictions until an agglomeration coefficient was included to account for suspected particle aggregation. The results reported lay a foundation for developing bactericidal PEEK composites with an integrated reservoir of antibacterial agents to maintain long-term efficacy. With process optimization, the Ag content of PEEK may be tuned to achieve sustainable, bactericidal levels of Ag^+ release in the future.

Specific Aims

Aim 1: Develop and validate methods for PEEK to measure crystallinity using FTIR and to characterize mechanical behavior using miniature specimens. PEEK is a strong and versatile polymer; nevertheless, it is also costly and often molded into small and complicated designs not feasible for standard crystallinity analysis or mechanical testing.

Aim 2: Evaluate antimicrobial activity and elution kinetics of Ag particles and develop an analytical model for the release of Ag from a PEEK matrix based on Ag^+ production kinetics.

Aim 3: Fabricate and analyze the properties of Ag-PEEK composites.

a) Fabricate composite specimens using a twin-screw extruder with subsequent injection molding.
b) Analyze the relationship between Ag filler (both material and concentration) and the crystallinity and mechanical properties of the composite material using methods developed in Aim 1.
c) Characterize the antimicrobial activity of Ag-PEEK composites against *S. Aureus* and *E. Coli*.
d) Quantify Ag^+ release from the material types that exhibit at least a ten-fold reduction in bacterial colonization and validate the analytical Ag release model.

Introduction

Periprosthetic Infection

Infection is a devastating and sometimes life-threatening complication of orthopaedic, spine, and trauma device implantation. Periprosthetic, or device-related, infections are one of the more frequent reasons for arthroplasty revision surgeries; once an infection is established, it is difficult to eliminate [1-5]. Infection arises in 1 to 2% of all primary arthroplasty procedures yet is associated with 10-33% of implants revised previously for infection [2, 3, 5-8]. Infection rates for specific procedures can be even higher. For fracture fixation devices, infections develop in an average of 5% of cases [4, 9, 10]; however, the infection rate climbs to 30% when the procedure involves external pin fixation [11, 12]. Infections are also a risk with spinal fusions and are a complication in up to 6.7% of procedures, leading to bone destruction and the eventual destabilization of the implant and spinal segment [13]. Additionally, infection increases the economic burden for both patients and hospitals. Bozic and Ries found direct medical costs for revision of infected total hip arthroplasty (THA) were 2.8 times higher than revision for aseptic loosening and 4.8 times higher than primary THA [1].

Many experts suggest that the infection rates are masked by various clinical circumstances and are in reality higher [9, 14-16]. Infections go undetected in clinical diagnosis because physicians depend on tests and microbial cultures, such as aspirates of joint regions, that have low yield [10]. If antibiotics are administered before the retrieval of diagnostic samples, there is

also an increased probability of missing the infection [10]. Finally, infection rates may be underestimated based on the limitation of clinical microbiological techniques to detect device-related indolent infections reproducibly [10, 15, 16].

The conditions for periprosthetic infection begin with implantation of the device. Bacteria from the surgical procedure or blood-borne bacteria adhere to the implant surface through surface tension, electrostatic forces, or by specific adhesions such as fibrinogen-binding adhesins on the cell membrane [9, 17]. Bacteria then become irreversibly attached by producing a network of fibrous polysaccharides and glycoproteins, specifically glycocalyx. Biofilms take few bacteria to initiate, and the resulting sister cells created through cell division are immediately embedded in the exopolysaccharide matrix [9, 18, 19]. Ultimately, the adherence of bacteria to the implantable material forms a biofilm, which organize in a three-dimensional tissue-like structure as it matures (Figure 0-1).

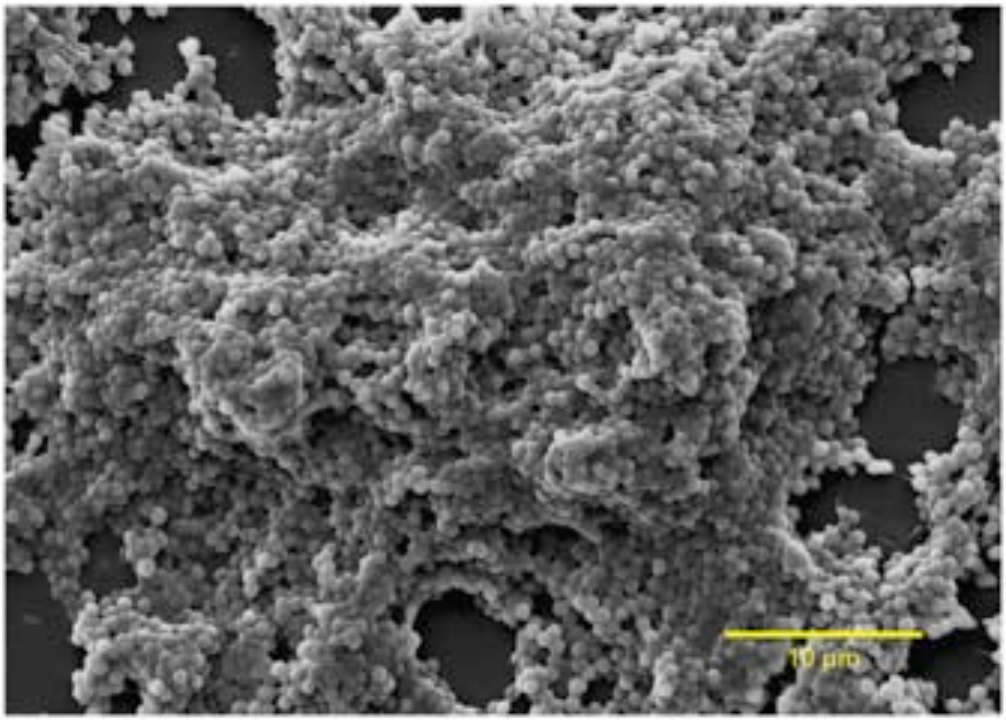

Figure 0-1: After initial attachment, bacteria begin forming biofilm in layers of microbes, as shown here with *S. epidermidis*, and obscure many of the bacteria below the surface.

After a biofilm is established, new bacteria adhere directly to the existing biofilm without initiating glycocalyx production [18]. Eventually, a mature biofilm reaches "critical mass," and the top layer of the biofilm releases planktonic microbes into the surrounding environment, which subsequently seeds new areas. The bacteria then colonize surrounding tissue, and the implant becomes a continuing source for infections [20].

Isolated from local immune system defenses, the most substantial problem with periprosthetic infection is the failure of systemic antibiotics to eradicate the biofilm. This is caused by the low diffusion rate of antibiotics across the biofilm membrane, difficulty in maintaining therapeutic levels of antibiotics

around a relatively avascular implant, and a downshift in the metabolic activity of the bacteria sequestered in the biofilm [16, 18, 21]. Due to the inability of systemic antibiotics to eliminate the infection in situ, most infected implants, such as total joint replacements, have to be explanted. Once the implant is explanted, dead or damaged tissue is removed, and a large does of local antibiotics is delivered to the infected area. For most orthopaedic implants, the infected cavity is filled with antibiotic-loaded polymethylmethacrylate (PMMA), also known as bone cement. The bone cement diffuses antibiotics directly to the infected implant site over an extended period of time, which ranges from 6 weeks to 4 months [21-24]. The treatment process to remove infection is lengthy, involves two surgeries, and after the procedure the patient has a higher probability of reinfection.

Infection Prevention Methods

To minimize the occurrence of periprosthetic infection, research efforts have focused on the development of surface modifications and materials resistant to bacterial growth. Anti-adhesive and anti-biofouling surfaces, which do not actively kill or inhibit microbial function but prevent adherence of cells and proteins on the surface, have been explored as a means to eradicate device related infections [25-30]. Polyurethane surfaces have been made hydrophilic with hydroxyethyl methacrylate or Hydromer coatings (Hydromer, Inc.), significantly reducing the adhesion of coagulase-negative *staphylococci* [28, 29]. However, preventing bacterial adherence also prevents host cells from adhering

to the implant. This reduces tissue integration and makes implant stability a concern. [26, 31].

Various antiseptics and antibiotics (Chlorhexidine, rifampicin, etc.) have been coated or absorbed onto the surface of implant materials [28-30, 32-34]. However, drug-loaded polymer based coatings are often problematic due to rapid or unpredictable drug release rate [29]. To increase predictability and control of release, direct incorporation of antimicrobials into the polymer structure of the device during manufacturing has shown effectiveness in catheters. The incorporation of the antimicrobials into the polymer structure extends their elution time by converting the structure of the polymer into slow-release reservoir [29, 34, 35]. Despite the promising properties of antibiotic and antiseptic incorporated devices, development of resistant bacteria always poses a limitation to their use. As antibiotic use has risen, the emergence of resistant bacteria strains, like methicillin-resistant *Staphylococcus aureus* (MRSA), has also grown. To combat antibiotic resistant strains of bacteria, multicomponent systems, like silver (Ag), are being used. The complex nature by which Ag eliminates bacteria reduces the probability of the development resistant bacteria.

Antimicrobial Properties of Ag

Metals such as Ag, gold, and copper have antimicrobial properties. Ag has emerged as a popular choice for medical devices because of its wide range of activity against both Gram-positive and Gram-negative bacteria, as well as fungi. Ag has also shown a relatively low cellular toxicity when compared to other

metals [36-39] because the negative effects to mammalian cells are mitigated by resident intracellular metallothioneins and rapid uptake of Ag into the mononuclear phagocyte system [40-42]. Ag particles have reached the market in such medical applications as dental resin composites [43] and burn wound treatments [44], but it is most widely used as an antimicrobial coating in catheters [45, 46].

The antimicrobial properties of Ag are thought to be due to interaction of the Ag^+ with sulfur, oxygen, and nitrogen functional groups [22, 26, 27]. Commonly, Ag^+ interacts with thiol groups (-SH) on structural proteins and key respiratory enzymes in bacteria. This inactivates the proteins and interferes with their proper function within the cell [26]. This can lead to structural damage on cell walls, reduction in cell metabolism, and loss of the ability to regulate exposure to oxidative reactions [22, 26]. Ag^+ can interact with enzymes of the respiratory chain reaction such as NADH dehydrogenase resulting in the uncoupling of respiration from ATP synthesis. Ag^+ can also bind with transport proteins leading to proton leakage and inducing collapse of the proton motive force [47, 48]. Ag^+ has also been observed to cause bacterial DNA to conglomerate centrally in the cell as a defense mechanism against its denaturing effects. This condensation results in the arrest of replication as the DNA is no longer in the required relaxed conformation [27]. Likewise, non-ionic Ag nanoparticles may directly affect bacteria by destabilizing the outer membrane of the bacteria. This collapses the plasma membrane potentials and reduces the levels of internal ATP [48]. Transmission electron microscopy has observed Ag

nanoparticles penetrating the membranes of E. Coli, producing pits across the surface, and increasing cell permeability [44, 49-51]. Because of the multiple mechanisms for interaction between Ag and bacteria, the risk of developing bacterial resistance through single point genetic mutations is reduced. Plasmids have been isolated from clinical strains of *Salmonella* in burn wards that confer resistance to the presence of Ag through proteins, which sequester Ag at the surface of the cell membrane and prevent it from interacting with the rest of the cell [52, 53]. Methods differentiating between Ag sensitive and resistant bacteria are not well established and even the existence of Ag-resistant bacteria that pose a clinical threat is currently in question [52, 53].

Concerns have been raised over the *in vivo* efficacy of silver coatings and additives in use for urinary catheters and other implanted devices [30, 46, 54-56]. This is because immediately after implantation, implant surfaces are coated in a conditioning film of serum and glycoproteins. For urinary catheters, the Ag-silicone materials additionally become encrusted due to the mineralization of Ca^{2+} and Mg^{2+} when exposed to high media concentrations of struvite and hydroxyapatite [30, 57]. These physiologic coatings have been thought to inhibit release or decrease activity of Ag^{+} with the presence of albumin, proteins, and Cl^{-} on biomaterial surfaces [46, 55, 58]. The antibacterial effect of Ag^{+} is known to be caused by its affinity to bind to O, N, and thiol groups on bacteria proteins; however, this effect is diminished by the abundance of proteins and ions in the mammalian tissue environment sequestering Ag^{+} before interaction with bacteria. Previous studies have increased the Ag MIC for *E. coli, S. aureus,* and *S.*

epidermidis by the addition of albumin and Cl^- into the incubation media [55, 59]. Further analysis by microradiography also revealed up to 3 mol of Ag bound to 1 mol of albumin [55]. Nevertheless, elution trials of Ag impregnated PMMA and silicone after the application of a blood plasma conditioning film exhibited either no reduction in Ag^+ release *in vitro* [46, 60-64] or 20-fold greater release when compared to uncoated controls [46]. In some studies, a conditioning film also correlated with increased antibacterial effects [60-62]. Increased biocidal properties could be linked to increased dissolved oxygen content within the media [65, 66]; however, the exact mechanism for this effect is unknown [62]. Initial studies suggest that protein and serum surface-coatings do not directly inhibit Ag^+ elution or impact antibacterial properties if Ag^+ concentrations remain in excess to compensate for Ag^+ bound to non-bacteria proteins [46].

Competing theories exist for the mechanisms of Ag^+ release from metallic Ag. Initial studies linked the antimicrobial activity of Ag to oxidized surfaces [48, 58, 67, 68]. Gibbard in 1937 revealed metallic Ag surfaces exhibited little antimicrobial effects when polished or cooled from melt in a hydrogen environment. Although, when cooled in an oxygen environment, Ag actively inhibited bacteria growth [67, 68]. Gibbard also discovered that colloidal silver, silver oxide, and silver nitrate continuously retained activity [67, 68]. Further support for oxidized Ag was gained in recent years by Lok et al., where increased antibacterial activity was observed when nanoparticles were suspended in solution that was bubbled with oxygen prior to incubation with bacteria [48]. These data suggest that the active agent is actually Ag oxide (Ag_2O), which

dissolves in H_2O to produce available Ag^+ for interaction with bacteria [48, 58]. However, Ag_2O has previously shown 1000-fold lower activity than pure silver coatings on catheters and is no longer available on the market due to a lack of efficacy [45, 56]. In addition, silver nanoparticles that have not been intentionally oxidized or have been coated with either citrate of PVP have exhibited sufficient levels of Ag^+ release to retard bacterial growth [44, 65, 69-73]. Ag nanoparticles have a higher enthalpy of formation than an equivalent mass of bulk Ag due to the increased surface area to mass ratio [65, 70, 72]. The increased specific surface positively influences the rate of oxidation with elevated levels of surface reactive atoms. The literature suggests that multiple factors influence the Ag^+ release from silver including surface oxide layer, surface functionalization, and surface area [65, 72, 73].

Various techniques have been utilized to harness the antimicrobial properties of Ag including co-sputter of Ag on to hydroxyapatite (HA), physical vapor deposition (PVD), and spin casting [74]. The Ag layer shows poor adhesion and lacks coating uniformity with materials such as polyurethane. [75, 76]. Recently, Ag has been added directly to molten polymers for incorporation into the bulk matrix; examples include Ag impregnation of various polyurethane and silicone catheters [29, 45, 46]. Such bulk loading removes the risks of scratching surface coatings, mechanical failure, low surface adhesion, and uncontrolled release rates of Ag^+ from the surface coating. Bulk incorporation of Ag has been successfully used in Ag/polyamide composites or in bone cement composites, where nanoAg particles were added during the monomer-mixing

phase. Both have shown promising Ag^+ release profiles and inhibition of *S. epidermidis*, *S. aureus*, *E. coil*, and *C. albicans* [62, 76]. Because of the inherent high temperature stability of Ag particulates along with its broad spectrum of antimicrobial activity, Ag additives are ideal candidates for the development of an antimicrobial composite with a high-performance thermoplastic.

PEEK- Poly(aryletheretherketone)

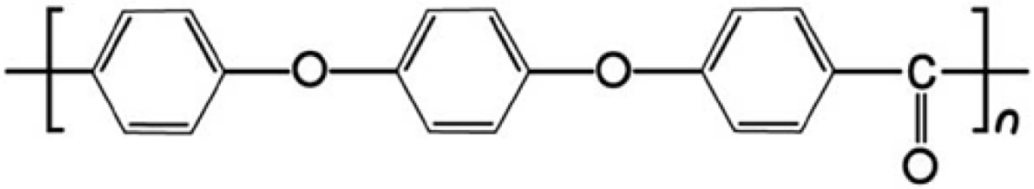

Figure 0-2: Chemical formula for Poly(aryletheretherketone). Reprinted with permission from http://www.medicalpeek.org/.

Poly(aryletheretherketone) or PEEK is a thermoplastic that is commonly used for spine and other load-bearing applications. PEEK has high temperature stability of upwards of 300°C, is resistant to chemical and radiation damage, and is biocompatible. The glass transition (T_g) and melt temperature (T_m) of PEEK are 143°C and 343°C respectively [77]. Typical injection-molded PEEK samples have a degree of crystallinity ranging from 30 to 35% (per mass), but annealing at temperatures above T_g can raise this by increasing lamellar thickness [78]. PEEK is a relatively stiff molecule, due to the planar benzene rings of its

backbone [79], but the molecule still has the ability to rotate axially about the ether and ketone-carbon bonds [80].

The stability and thermal properties of PEEK make it an excellent candidate for composite manufacturing to tailor its properties for specific applications. PEEK has been blended with hydroxyapatite (HA) and bioactive glass to promote bone on-growth *in vivo* without impacting melt processing or crystallization [81, 82]. Chopped carbon fiber reinforcement (CFR) has strengthened the elastic modulus of PEEK (3-4GPA) to levels closer to cortical bone (20GPa), and 68% continuous CFR has increased elastic modulus (135 GPa) above titanium alloy (110 GPa) [82]. PEEK transitioned from industrial use into the medical device field due to its mechanical properties analogous to bone. CFR-PEEK emerged in the 1990s as an ideal candidate for a posterior lumbar interbody fusion device (the Brantigan Cage), since titanium alloy, and other metal alternatives, had a high elastic modulus (110 GPa) compared to cortical bone (18 GPa) [80]. Disproportionate mechanical properties would encourage stress shielding and a reduction in bone quality in adjacent spinal segments. Diagnostic assessment of bone growth is also uninhibited due to the radiolucency of PEEK. Because of the success of the Brantigan Cage, in the past two decades, PEEK has permeated the spinal industry in a wide range of applications from posterior dynamic stabilization (CD Horizon Legacy, Medtronic, Inc.) to PEEK-on-PEEK implants for nucleus replacement (NUBAC, Pioneer Surgical Technology, Inc.). Currently, PEEK is being investigated outside of the spine as a material for the bearing surface in joint replacements, hip resurfacing

technology, finger joint replacements, and for composite hip stems [80, 83]. Given this active increase in the share of medical device industry, there is a growing need to design surfaces and PEEK materials that will actively prevent bacteria adhesion and infection.

With the current prevalence of periprosthetic infection, material properties of PEEK, and the anti-microbial effectiveness of Ag, I hypothesis that adding commercially available Ag to the bulk of PEEK will reduce bacterial adhesion to the surface, and thus prevent the occurrence of biofilm formation and periprosthetic infection.

1. Develop and Validate Methods for PEEK to Measure Crystallinity Using FTIR and to Characterize the Mechanical Behavior Using Miniature Specimens

Standardized testing currently lacks options for characterizing crystallinity and mechanical behavior for medical implants and research materials that are either too small for bulk mechanical testing, like the tensile test, or retain complex geometries outside of the required dimensional constraints. Nevertheless, since manufacturing conditions and mold temperatures greatly influence crystal lamellae formation and mechanical behavior of the polymer matrix, characterizing as-manufactured materials is vital. To alleviate these issues, the following studies were designed to validate tests for the characterization of limited materials and a wider range of implant designs.

Part 1 - Validation of Crystallinity Measurements of Medical Grade PEEK Using Specular Reflectance FTIR-microscopy[1]

[1] Previously published as, "Jaekel DJ, Medel FJ, Kurtz SM. Validation of Crystallinity Measurements of Medical Grade PEEK Using Specular Reflectance FTIR-microscopy. Society of Plastics Engineers Annual Technical Conference. Chicago: Society of Plastics Engineers; 2009" and as ASTM standard, "ASTMF2778-09. Standard Test Method for Measurement of Percent Crystallinity of Polyetheretherketone (PEEK) Polymers by Means of Specular Reflectance Fourier Transform Infrared Spectroscopy (R-FTIR). West Conshocken, PA American Society for Testing and Materials; 2009."

Abstract

Characterizing the crystallinity in PEEK is critical, since it dictates the mechanical behavior of the polymer. Wide angle X-ray scattering (WAXS) has been typically employed for this purpose; yet, it is impractical for the measurement of some composite materials. Differential scanning calorimetry (DSC) has also been used but with limited accuracy. Specular Reflectance Fourier transform infrared (R-FTIR) microscopy has been identified as a suitable method to measure the crystallinity of industrial grade PEEK, but the usefulness with medical grade PEEK remains unknown. By comparing R-FTIR, WAXS and DSC for a range of medical PEEK grades, we demonstrate that FTIR can detect changes in crystallinity due to annealing treatments and incorporation of carbon fibers or radiopaque compounds.

Introduction

Polyetheretherketone (PEEK) is widely used as a structural load-bearing polymer in spinal implants and is increasingly used for trauma and orthopedic medical devices [80]. Mechanical properties of PEEK, such as yield strength, elastic modulus, or toughness, are determined to a large extent by its degree of crystallinity [77]. In this sense, annealing treatments are commonly used to promote higher crystallinity and thus improved mechanical strength in injection molded PEEK parts. Therefore, characterizing the degree of crystallinity in PEEK is paramount for predicting the mechanical behavior and performance of PEEK implants [80]. Wide angle X-ray scattering (WAXS) is considered the most

accurate method for measuring crystallinity in PEEK [80]. However, it is not practical for the measurement of as-manufactured PEEK implants, which can contain fiber reinforcement or image contrast agents. Differential scanning calorimetry (DSC) has also been used to characterize PEEK crystallinity, but has limited accuracy due to recrystallization phenomena that occur during the experiment [80].

Fourier transform infrared (FTIR) microscopy is a practical method for physical and chemical characterization of polymers. In review of infrared spectroscopy techniques for PEEK, research was previously conducted into crystallinity measurement with both Multiple Internal Reflection/Attenuated Total Reflection (MIR/ATR) and FTIR in transmission mode [77, 80, 84-87]. PEEK is a highly absorbing polymer; therefore, very thin films (10 μm or less) are typically necessary to accurately quantify and measure intense absorption bands in the mid-infrared range when working in the transmission mode [85, 86]. Films of this nature are difficult to produce with either compression molding or a microtome. It was also attempted to flatten PEEK samples into thin films with diamond-anvil window compression, but this was observed to cause pressure induced crystallization [85, 86]. None of these sample preparation techniques ensure the preservation of crystallinity after modification, which makes quantification of crystallinity levels of as-manufactured samples highly inaccurate. On the other hand, ATR has also become a more standardized FTIR tool in research and manufacturing. ATR is fundamentally a single reflection technique and typically does not produce the high absorption intensity or the correct single-to-noise ratio

required for quantifying crystallinity [85]. Furthermore, reproducible sampling between the probe and hard contact surface of PEEK has been shown to be unfeasible for this type of characterization [85]. Finally, ATR requires the samples to be in contact with germanium or diamond element to get a single point measurement.

In contrast with the aforementioned FTIR techniques, specular reflectance FTIR (R-FTIR) is a non-contact, non-destructive testing technique, which requires little to no sample preparation. R-FTIR also has the potential for automated measurement of multiple points, and thus, detecting crystallinity gradients (if any) along cross-sections of manufactured parts. R-FTIR works through the collection of reflected energy off the surface of an optically thick material at a specific angle of incidence [85, 86]. The reflectivity of the specimen amplifies at the wavelengths in which the material displays strong IR absorption. The reflected radiation collection occurs at a near normal incidence (ca 30°) as opposed to diffusely scattered light, which intrinsically reflects at a much larger angular range. Therefore, R-FTIR requires a less optically flat surface area for each measurement recorded [85, 86]. R-FTIR microscopy has been reported to provide consistent characterization of crystallinity in industrial grades of PEEK [85, 86]. The generality of R-FTIR to characterize crystallinity in medical grades of PEEK, containing fiber reinforcement or radiopacifiers, remains unknown. The aim of this study was to compare the utility of R-FTIR, WAXS, and DSC techniques to evaluate the degree of crystallinity for a range of medical grades of PEEK OPTIMA®: standard; carbon fiber reinforced; and radio opaque. We

hypothesized that R-FTIR would detect changes in crystallinity due to annealing treatments and incorporation of carbon fibers or radiopaque compounds into medical grade PEEK.

Methods and Materials

Sample Preparation and Processing

Three medical grade PEEK-OPTIMA resins were obtained from the manufacturer in pellet form: virgin PEEK-OPTIMA LT1 (LT1), Radiopaque LT1 (RO), and LT1CA30 carbon fiber reinforced (CFR) (Invibio Ltd., UK). An unfilled industrial sample, 450 G (Victrex; UK), was also obtained with the same molecular weight as LT1. Resin was heated at 150°C for at least 3 hr to remove residual humidity prior to processing. Specimens were then injection molded into 0.7 mm thick tensile dogbone specimens (Figure 1-1) with a BOY 50M molder, under specific conditions recommended by the manufacturer (Invibio, Inc). The mold closing time was set to 30 seconds, and the mold temperature for LT1 and RO was approximately 190°C. For CFR, the mold temperature had to be increased to 220°C for proper molding.

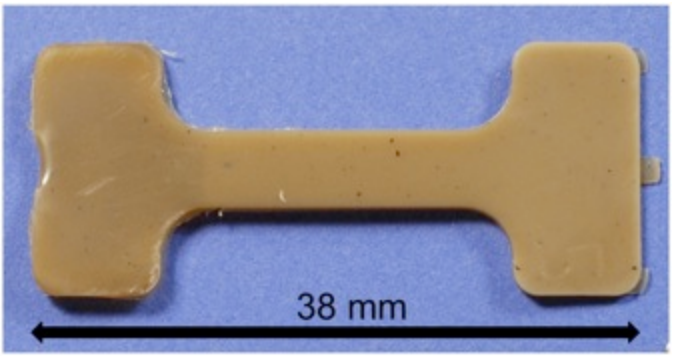

Figure 1-1: Injection molded tensile specimen of PEEK (Victrex 450G).

For each type of resin, four treatment-processing groups were created: as-molded (unannealed injection molded), 200°C annealed, 300°C annealed, and amorphous PEEK. These annealing temperatures were chosen to produce a broader range of crystallinity values for validation and comparison of various characterization techniques. In particular, 200°C was an annealing temperature recommended by PEEK manufacturers to obtain crystallinity values near 35%, and 300°C was chosen to attempt to raise the crystallinity to levels approaching 50%. When heating PEEK between glass transition and melting point, recrystallization and partial melting occur, and thus cause a higher degree of perfection in the crystalline regions and increases in lamellar thickness, and therefore in crystallinity [88, 89]. The 200°C annealed samples were dried at 150°C for 3 hr, and then ramp heated at 12°C/min to 200°C. They were held at 200°C for 4 hr and then ramp cooled at the same rate to below 140°C. Annealing was performed for the 300°C group in the same fashion with the exception that there was no controlled ramp heating or cooling. Amorphous PEEK was created

by heating to 400°C for 30 minutes, followed immediately by quenching in liquid nitrogen.

Wide-Angle X-ray Scattering

WAXS scans were performed with a Siemens D500 X-ray diffractometer. Diffraction patterns were acquired at a scanning rate of 0.03°(2θ)/min over an angular range of 5°<2θ<45°. Five samples (n=5) for each processing condition and PEEK grade were scanned, and samples were prepared by placing the gauge region of two tensile specimens in the WAXS chamber. This was due to dimensional requirements of the equipment. Once data was collected, a baseline was formed to create a zero point for the spectra. Next, curve fitting was performed to obtain the separate contribution of the amorphous and crystalline peaks to the WAXS patterns with the assistance of JADE Version 7 - XRD Pattern software (Materials Data, Inc.; USA). After defining a tentative custom set of initial peaks, the software was then allowed to iteratively adjust them to best fit the experimental WAXS pattern. To obtain optimal curve-fitting, the height and FWHH (Full-width Half-height) of the initial peak corresponding to the broad amorphous halo at 2θ = 20° had to be locked. The ratio of the total area below crystalline peaks (2θ = 19°, 21°, 23°, 33°, and 39°) to the overall area under crystalline and amorphous (2θ = 20°, and 28°) peaks yielded the percent crystallinity.

With CFR, an additional peak in the WAXS patterns appeared at 2θ = 25° (Figure 1-2), which was consistent with previous reports [90]. In this case, the CFR peak had to be included in the custom-defined set of initial peaks for proper fit of WAXS patterns, and further calculation of PEEK crystallinity. When radiopaque material (barium sulphate) was introduced into PEEK, differentiation of the peaks became even more complex (Figure 1-2). Barium sulphate WAXS patterns have been documented in the literature, so the 2θ values where barium sulphate peaks appeared were known [90, 91]. Again, initial peaks were specifically chosen for curve-fitting purposes based on their documented locations. In addition, RO PEEK WAXS patterns were curve-fitted in two ranges (2θ: 16° to 26° and 2θ: 26° to 40°) to more precisely assess area values, minimizing the influence of signal noise (Figure 1-3).

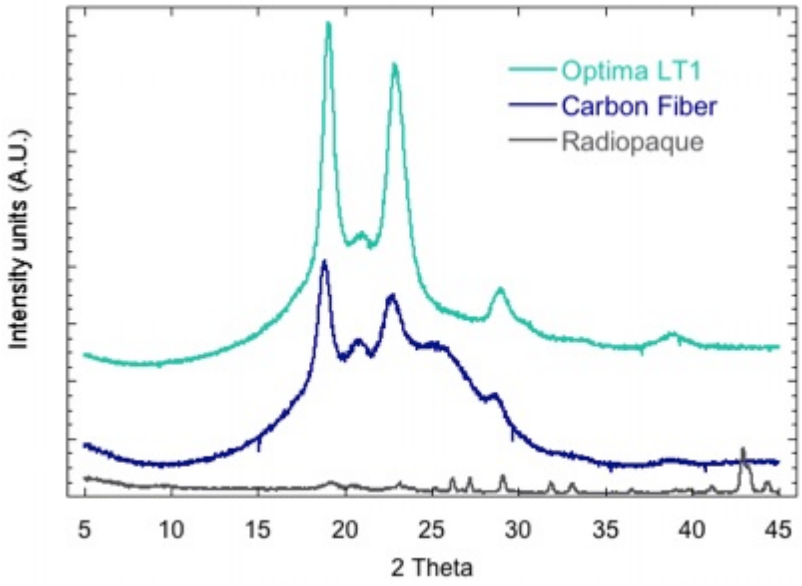

Figure 1-2: The effects of filler material on WAXS profiles.

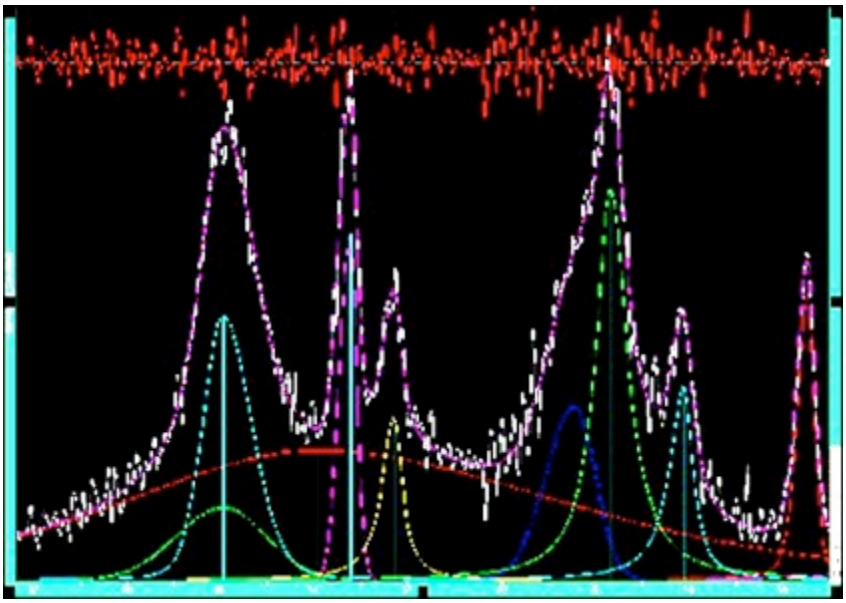

Figure 1-3: Curve-fitting of WAXS pattern for barium sulphate filled PEEK.

Specular Reflectance FTIR

Specular reflectance FTIR measurements were collected with a Nicolet Continuum (Thermo Electron Corp.) with an aperture size of 360 μm x 360 μm. FTIR spectra were acquired at a resolution of 4cm^{-1} at 100 scans per spectrum. The Kramers-Kronig transform algorithm was used to derive the absorbance spectra. Spectra were collected from the gauge region of the tensile testing specimens for 10 samples (n=10) per processing condition and PEEK grade. In the spectra range of 1400cm^{-1} to 900cm^{-1}, an automatic baseline correction was applied. As the absorption bands at 1305cm^{-1} and 1280cm^{-1} are known to be sensitive to crystallinity [85], the height ratio of these peaks was recorded for each material group (Figures 1-4 & 1-5). The height ratio of these peaks defines a crystallinity index (CI) based on R-FTIR measurements, which is given by the following equation:

$$CI = \frac{H_{1305}}{H_{1280}} \qquad \text{(Eq. 1)}$$

where H_{1305} and H_{1280} are the heights of the infrared bands centered at 1305cm^{-1} and 1280 cm^{-1}, respectively.

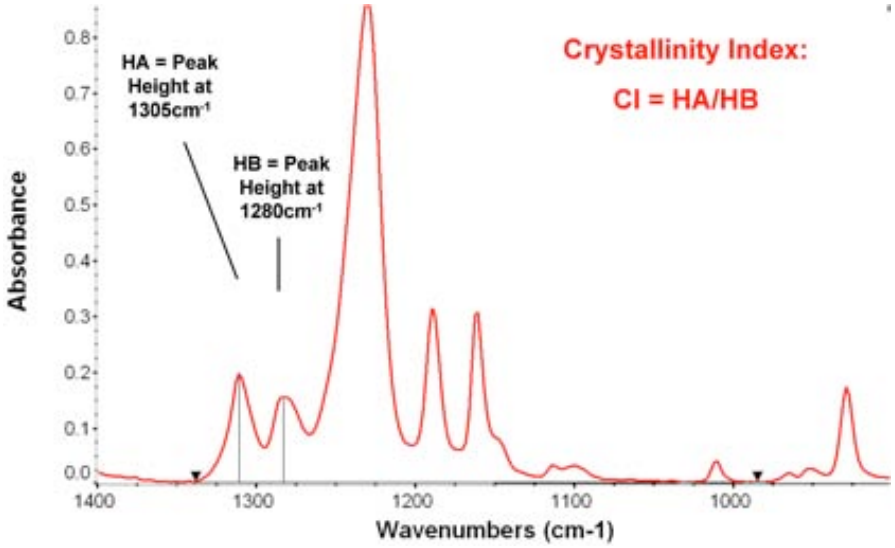

Figure 1-4: Typical specular reflectance spectrum with defined peaks.

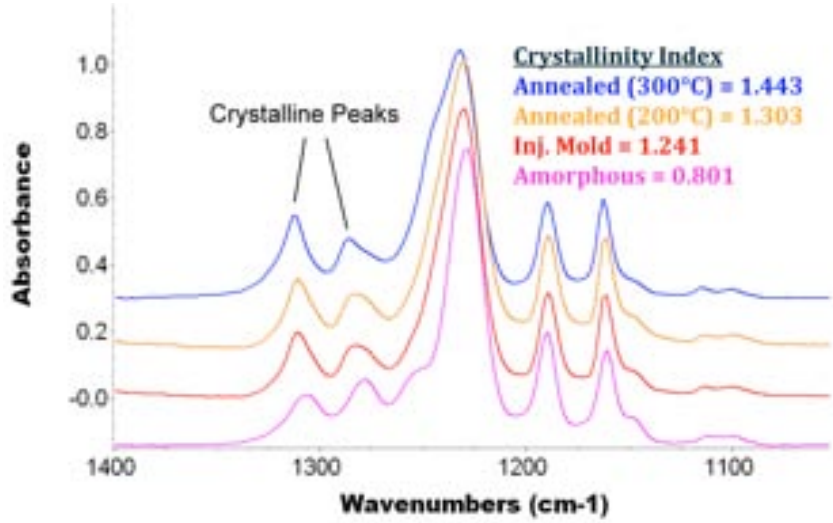

Figure 1-5: Specular reflectance FTIR spectra for various heat treated PEEK samples.

Differential Scanning Calorimetry

For DSC, approximately 7 mg samples were evaluated in a Q2000 DSC apparatus (TA Instruments). The same specimens employed for both R-FTIR and WAXS were sectioned and tested. All samples were equilibrated at 23°C and then heated at 20°C/min from 23°C to 400°C [92, 93]. Crystallinity was calculated by linear integration of the heat flow curve from 300°C to 360°C and assuming the heat of fusion of perfectly crystalline PEEK is 130 J/g [93]. Mass values were corrected for RO and CFR PEEK specimens, since they consisted of only 80% and 70% polymer, respectively. For example, 80% of the measured mass for a CFR specimen was used for defining the DSC thermogram.

Results

As-molded PEEK materials displayed similar R-FTIR crystallinity indices (~ 1.20), regardless of the addition of fillers. All annealed PEEK materials exhibited increased crystallinity indices compared to as-molded samples, with the highest increase after annealing at 300°C (CI: 1.38-1.54). In addition, all the amorphous PEEK materials consistently displayed the lowest CI values (~ 0.78) (Figure 1-6).

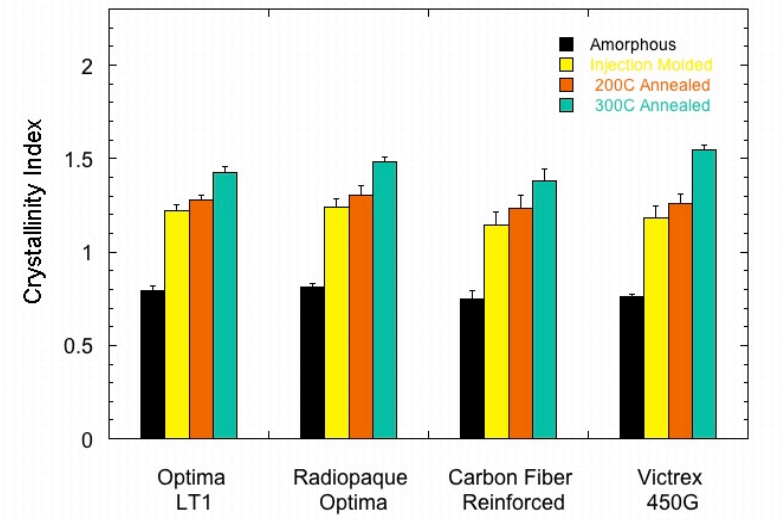

Figure 1-6: Summary of crystallinity index values for all samples (mean ± SD).

Percent crystallinity results calculated from WAXS measurements confirmed the trends found in the R-FTIR study. With the CFR grade, WAXS crystallinity increased from 25.4% to 41.4% after annealing of the as-molded CFR specimens at 300°C (Figure 1-7). All the amorphous samples for CFR and RO had no distinguishable PEEK signals in the WAXS patterns beyond the amorphous halo at $2\theta = 20°$, so the reported values were essentially zero when using this method.

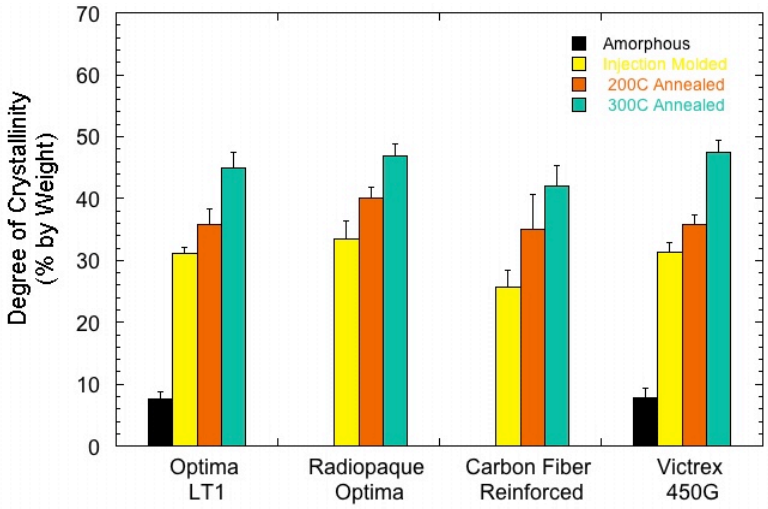

Figure 1-7: WAXS crystallinity measurements for all PEEK samples.

After comparing and plotting R-FTIR results against WAXS data, a highly linear correlation was observed between CI and percent crystallinity (Figure 1-8). The correlation was achieved by averaging the CI values for the two specimens combined for each WAXS measurement. For OPTIMA-LT1 alone, the linear fit resulted in an R^2 of 0.98 and when combined with data from the unfilled industrial grade, the linear trend line had an R^2 of 0.97. Once all PEEK grades were considered (Figure 1-8), a corresponding linear fit was produced, with a slightly lower R^2 value of 0.94.

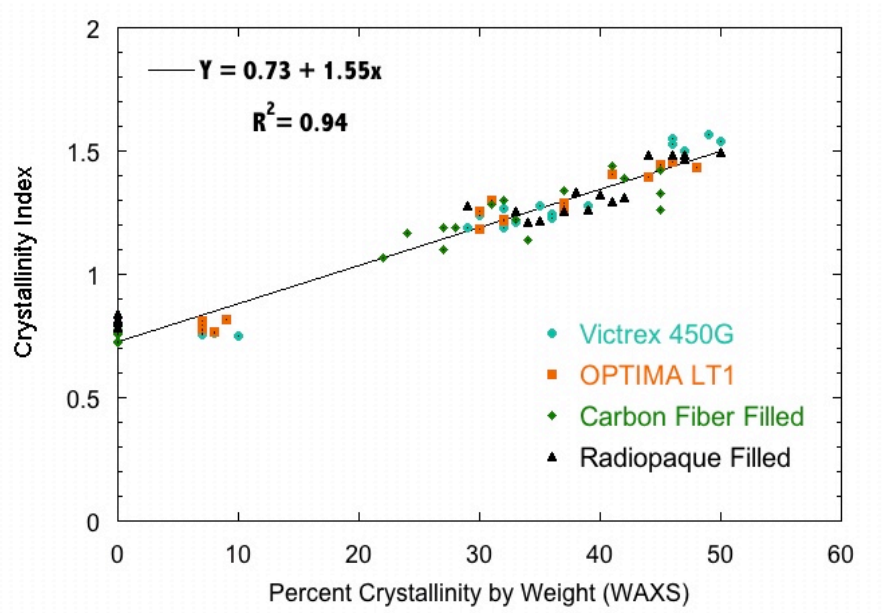

Figure 1-8: Correlation between R-FTIR and WAXS measurements for all PEEK samples.

In contrast with FTIR, DSC measurements were less sensitive to changes in crystallinity. For 450G, DSC provided indistinguishable crystallinity values (27.5±0.6%) regardless of post-processing treatments with the only exception being samples annealed at 300°C (37.2±2.4%) (Figure 1-9). For LT1, the DSC crystallinity values for samples annealed at 300°C were lower (23.8±2.5%) than those of as-molded and 200°C annealed specimens (29.3±1.0% and 30.0±10.6%, respectively). In general, the DSC measurements for degree of crystallinity in all PEEK materials were approximately 30% and also were unaffected by the addition of filler materials.

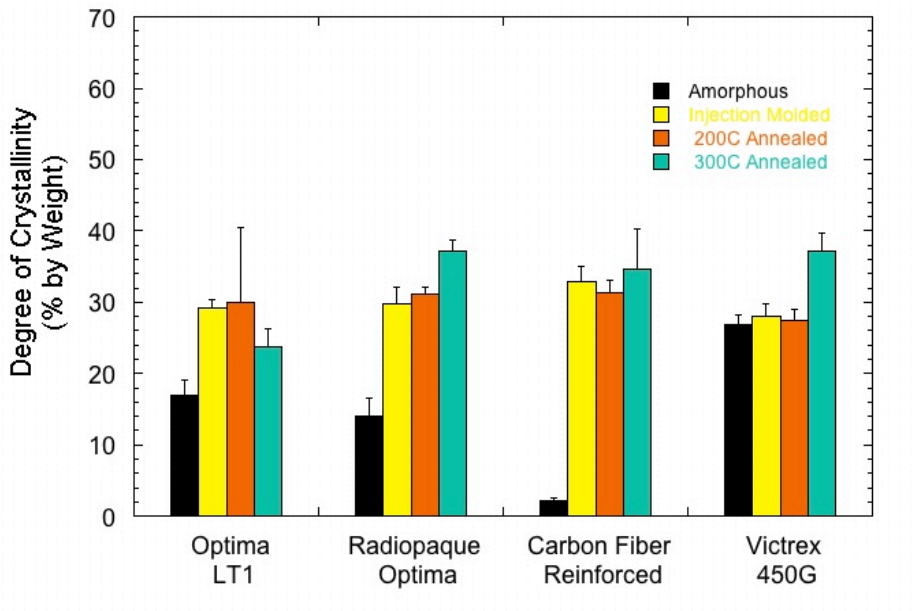

Figure 1-9: DSC Crystallinity measurements for all PEEK samples.

Discussion

In contrast with DSC, R-FTIR provided consistent trends in CI values in spite of the incorporation of fillers or the use of post-processing thermal treatments. Moreover, since the crystallinity index of R-FTIR was unaffected by the filler materials added to PEEK, new methods did not have to be developed to calculate the CI when either barium sulphate or carbon fibers were introduced with the base material. Also, because R-FTIR is a surface characterization technique, it might allow characterization of potential crystallinity gradients throughout cross-sections of manufactured PEEK parts. It also does not require much sample preparation for injection molded parts or have dimensional limitations for the tested samples. In comparison, WAXS provides an average bulk crystallinity measurement of the tested sample.

WAXS proved to be suitable for characterizing unfilled PEEK grades, but diffraction patterns of PEEK composites were altered due to X-Ray scattering of carbon fibers and barium sulphate. In these cases, more complicated methods involving curve-fitting were necessary to quantify the level of crystallinity. For example, WAXS patterns for the radiopaque composite had substantially different patterns than other PEEK materials because of the obscuring of crystalline peaks by barium sulphate signal contributions. That fact made the curve-fitting procedure of WAXS patterns much more time intensive than the R-FTIR method. For the amorphous composite materials, WAXS also presented the issue of displaying 0% for their crystallinity. On visual examination of a cross section of any amorphous sample, an increasingly lighter brown color from surface to center was observed, suggesting a slightly increasing crystallinity within the specimen. Therefore, this residual, non-zero, crystallinity may be the reason why WAXS patterns for amorphous LT1 and 450G showed little but noticeable crystalline signals, and as a result yielded low (7.7±1.0%) but non-zero crystallinity values. In contrast, WAXS seemed to be unable to quantify the low crystallinity in composite grades of amorphous PEEK, since crystalline PEEK signals were completely missing and 0% crystallinity was calculated for these materials.

With utilization of complex curve-fitting techniques, WAXS methods were able to produce repeatable percent crystallinity values. Due to the non-destructive nature of reflectance measurements, WAXS and R-FITR were performed on every specimen included in this study. Plotting WAXS and CI data against each

other, allowed for the creation of a master calibration curve for the Crystallinity Index (Figure 1-8). Thus, it was possible to formulate an equation from the linear regression of the master curve to obtain percent crystallinity from CI values:

$$\%Crystallinity = \frac{CI - 0.728}{1.549} \times 100 \quad \text{(Eq. 2)}$$

As opposed to R-FTIR and WAXS, the crystallinity measurements gathered from DSC were insensitive to changes in crystallinity due to the addition of fillers or post-processing procedures. This could be caused by crystals developed during the heating process of this method, which are not uncovered by crystallization exotherms in the DSC results [87]. Thus, the amount of recrystallization is unknown. In addition, DSC is a destructive test and requires sectioning which may not be feasible for evaluating as-manufactured specimens. Consequently, for representation of crystallinity level and for evaluation of as-manufactured parts, DSC appears to be an inaccurate and unreliable method.

Conclusions

The results of this study establish specular reflectance FTIR as a suitable technique for characterizing crystallinity of PEEK biomaterials. R-FTIR provides ease of use, quick testing time, and reproducible calculation method for crystallinity. Testing is non-destructive and can be universally applied for many PEEK grades. WAXS, though able to measure crystallinity in virgin PEEK forms, is much more time intensive for testing, and involves complex curve-fitting procedures to obtain crystallinity measurements for filled materials. DSC has also been shown to be unreliable for measuring percent crystallinity within this study.

It was unable to resolve differences between annealing processes and displayed varying trends between PEEK grades. The findings shown here will provide a useful basis for developing a standard method that can be used for characterizing crystallinity in medical grade PEEK and other composites using specular reflectance FTIR.

Part 2 - Characterization of PEEK Biomaterials Using the Small Punch Test[2]

Abstract:

The small punch test is widely used to characterize the ductility and fracture resistance in metals and ceramics when only a small volume of material is available. This study was conducted to investigate the suitability of the small punch test for characterizing polyetheretherketone (PEEK) polymeric biomaterials for changes in material grade, crystallinity, and molding process. The small punch test reproducibly characterized the mechanical behavior of PEEK and was able to distinguish differences induced by molding process alterations and annealing. Peak load was most sensitive to changes in crystallinity, grade, molding process, and increased with increasing crystallinity but lowered with addition of image contrast material. Ultimate displacement was

[2] Previously published as, "Jaekel DJ, Macdonald DW, Kurtz SM. Characterization of PEEK biomaterials using the small punch test. Journal of the mechanical behavior of biomedical materials. 2011;4:1275-82.

negatively correlated with crystallinity. Molding process conditions had the greatest influence on metrics of the small punch test, when compared with the effects of annealing and addition of radiopacifier. The results of this study validate the small punch test as a repeatable method for measuring mechanical behavior of PEEK biomaterials.

Introduction

For over two decades, the small punch test (also referred to as the "miniature disc bend test") has been used to characterize ductility and fracture resistance in metals and ceramics when only a small volume of material can be obtained [94-96]. Conventional mechanical testing requires relatively large specimen sizes, and therefore these bulk specimen methods are unsuitable to directly measure the properties of as-manufactured medical devices, to evaluate retrieved implanted components, or to determine localized differences inferred from specialized manufacturing processes. In more recent years, this miniature specimen technique was adapted for orthopedic polymers like ultra-high molecular weight polyethylene (UHMWPE) and various bone cements [94, 95]. Specifically, the small punch test has been useful for evaluating changes that occur in UHMWPE after long-term aging; wear testing; and in vivo use in accordance with ASTM F2183. Although the small punch test has been used to characterize polymer biomaterials such as UHMWPE and various bone cements, little is known about the application of the small punch test in regard to medical

grade polyetheretherketone (PEEK) or its radiopaque composite biomaterials [94, 95].

PEEK has high temperature stability of upwards of 300°C, resistance to chemical and radiation damage, and favorable biocompatibility [80, 82, 97]. The average tensile strength and flexural modulus of PEEK are 93 MPa and 4 GPa respectively; however, with PEEK composites reinforced by hydroxyapatite or carbon fibers, these properties can be tailored to the desired biomedical application [80, 82, 98]. Due to favorable properties of PEEK, it was adapted for the medical device world starting in the 1990's with the Brantigan Cage, which was designed to stabilize the anterior column of the spine. Since then, PEEK has been increasingly used by the orthopedic, spine, and trauma device industries as a structural load-bearing polymer [80, 98]. With PEEK and its composites more widely being adapted to numerous implant designs, it has been challenging to evaluate potential in vivo changes of mechanical behavior using conventional bulk tests, such as tensile testing, due to the unique size restrictions of implanted devices. There is a current void in the literature on miniature specimen testing of load-bearing polymer such as PEEK; thus, validation small punch testing is necessary for future characterization of the mechanical behavior of PEEK implants, before and after removal from the body.

PEEK is a two-phase semi-crystalline polymer that typically ranges from 30 to 35% crystallinity, depending upon thermal processing conditions and annealing [77, 80, 87, 99]. Mechanical properties can be influenced by the degree of crystallinity, and it has previously been reported that increasing

crystallinity can increase elastic modulus and yield strength, while conferring lower toughness [77, 80, 89, 99]. In the past, crystallinity related differences in mechanical properties have been characterized by bulk samples in tensile testing, but have not been investigated for PEEK on a miniature sample scale.

The primary goal of this study is to investigate the suitability of the small punch test for characterizing the mechanical behavior of PEEK biomaterials. This experimental procedure was used to record the stiffness, peak load, and fracture behavior for two commercially available grades of implantable grade PEEK (Optima LT1 and Image Contrast or Radiopaque grade, LT120BA). We hypothesized that, due to the addition of radiopacifier, the image contrast material would exhibit lower yield and ultimate small punch test behavior. We were also interested in whether the small punch test could not only differentiate behavior between grade and filler material, but also changes in the degree of crystallinity and molding conditions. We hypothesized that materials with higher crystallinity would exhibit greater stiffness and peak load with lower toughness and ductility.

Materials and Methods:

Materials

Two medical grade PEEK OPTIMA biomaterials (Invibio Ltd, Lancashire, United Kingdom) were obtained in pellet form: (1) an unfilled grade of PEEK (OPTIMA LT1), and (2) a 20% $BaSO_4$ filled image contrast grade (LT120BA). Average particle size for BaS04 was 1-2 μm as stated by manufacturer and

confirmed by SEM. The image contract grade of PEEK was designed for optimal visualization under x-ray, MRI, and CT imaging techniques. Prior to molding, both of the resins were heated at 150°C for at least 3 hours to remove residual moisture. Testing samples were manufactured for each resin type using two injection molding processes. The first set of samples were molded using standard industrial recommended settings of a maximum barrel temperature of 375°C and injection pressure near 14 MPa (Invibio, Ltd) to produce 38 mm diameter and 10 mm thick pucks. From these, 7-mm cylinders were bored and subsequently machined into 0.5mm-thick and 6.4mm-diameter disc-shaped specimens. A second set of samples was injection molded using a different processing method. These samples were manufactured using a mold for thin walled (0.7mm) parts. The equipment molded at a slightly lower pressure 13 MPa and higher temperature (>410°C) to fill the mold. The high temperature process specimens were molded into 7.5 mm cylinders from the sprue region of the final molded part using a BOY 50M molder. The cylindrical samples were then machined to the specified sample size mentioned previously.

Annealing and level of crystallinity

To investigate the effects of crystallinity on mechanical properties, three unique annealing conditions were used on all of the material groups to provide a broad range of crystallinity within each group: (1) as-molded (unannealed), (2) 200°C annealed, and (3) 300°C annealed. The 200°C annealed samples were dried at 150°C for 3 hr, and then ramp heated at 12°C/min to 200°C. They were

held at 200°C for 4 hr and then ramp cooled at the same rate to below 140°C. Annealing was performed for the 300°C group in the same fashion with the exception that there was no controlled ramp heating or cooling. These annealing conditions are expected to produce samples that range in crystallinity from 15% (unannealed) to 50% (300°C annealed). The thickness and height of the annealed samples were monitored before and after heat treatments to ensure annealing did not induce dimensional changes.

Crystallinity was calculated for each punch specimen using specular reflectance FTIR spectroscopy measurements at the center of the sample as detailed previously and in accordance with ASTM F2778 [99, 100]. This method measures the peak height ratio of the absorption bands in specular reflectance FTIR spectra at 1305cm^{-1} and 1280cm^{-1}. These peaks are known to be sensitive to crystallinity, and have been previously correlated to wide-angle X-ray scattering measurements to produce a direct measurement of crystallinity as a percentage from the FTIR spectra as described in ASTM F2778 [85, 99, 100].

Small punch testing

Specimens were confined in a die and guide fixture and then subjected to bending by indentation with a custom-built, hemispherical headed punch as described previously (Figure 1-10) [94-96]. Testing was conducted similarly to ASTM F2183[101], which describes the procedure for small punch testing of UHMWPE. Load and displacement were recorded as a constant displacement rate of 0.5 mm/min was applied. Load displacement curves were characterized by the peak load, ultimate load, ultimate displacement, and work to failure. After

failure of the specimens, fracture surfaces were analyzed using light microscopy as well as scanning electron microscopy (SEM) where appropriate.

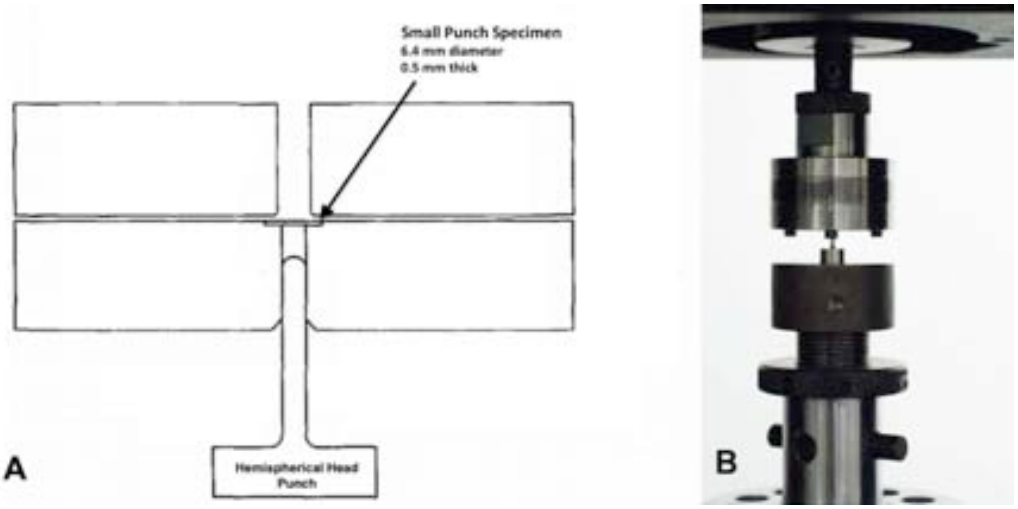

Figure 1-10: (A) Diagram of the small punch test fixture, disc confinement, and hemispherical head punch. (B) Photograph of fixture and testing configuration used.

Cyclic loading

Initial examination of PEEK small punch discs showed the linear elastic region of the load-displacement curve was located at loads lower than 15 N and at displacements lower than 0.6mm. Subsequently, to confirm the stabilization of the slope of linear-elastic region in the Load-Displacement curves, 5 standard process specimens of both unfilled and image contrast grades of PEEK were subjected to cyclic loading in the small punch apparatus. The displacement rate was consistent with previous tests (0.5 mm/min). An extensometer was attached to the testing fixture for direct recording of displacement to accurately measure the initial linear region. Samples were cyclically loaded 10 times in load range of 0.5 to 15 N, and following the tenth cycle, samples were tested to failure at the

same displacement rate. Stiffness was determined for each cycle based on the slope of the linear regression line that was fit to the data. A linear correlation between small punch stiffness and elastic modulus was previously determined by Edidin and Kurtz for various medical polymers (UHMWPE, polyacetal, etc.)[102]:

$$E=k*A \quad \text{(Eq. 3)}$$

where *E* is the elastic modulus, *k* is the stiffness, and *A* is a constant coefficient. Edidin and Kurtz determined the main influence to *A* was the Poisson's ratio of the biomaterial. Therefore, since the Poisson's ratio of PEEK (0.36) and polyacetal (0.35) are similar, the constant coefficient value for polyacetal (14.6) was used for calculating the elastic modulus of PEEK[80, 102].

Statistics

For each molding process, material grade, and annealing condition, a minimum of 10 samples was tested per group, resulting in a total of 120 specimens. The distributions of mechanical properties and crystallinity were inspected for normality using the Shapiro-Wilk test. For comparisons with normal data sets, T-Tests or ANOVA with a post-hoc Tukey was used. For comparisons with non-normal data sets, the Mann-Whitney U test or Kruskal-Wallis 1-way ANOVA was utilized, where appropriate. For all statistical tests, PASW Statistics (Version 18.0.0; IBM, Chicago, IL) was used.

Results

Small punch test results

The load-displacement curve recorded for PEEK materials displayed an elastic deformation phase and peak load followed by a shorter or equal length plastic membrane-stretching phase (Figure 1-11: representative PEEK load displacement plot). The average value for all metrics analyzed is summarized in Table 1-1. For each annealing condition, no differences were observed in the crystallinity values between unfilled and image contrast grade materials in the standard ($p > 0.2$; T-Test) or high temperature process ($p \geq 0.05$; Mann-Whitney U Test) processes (Table 1-1).

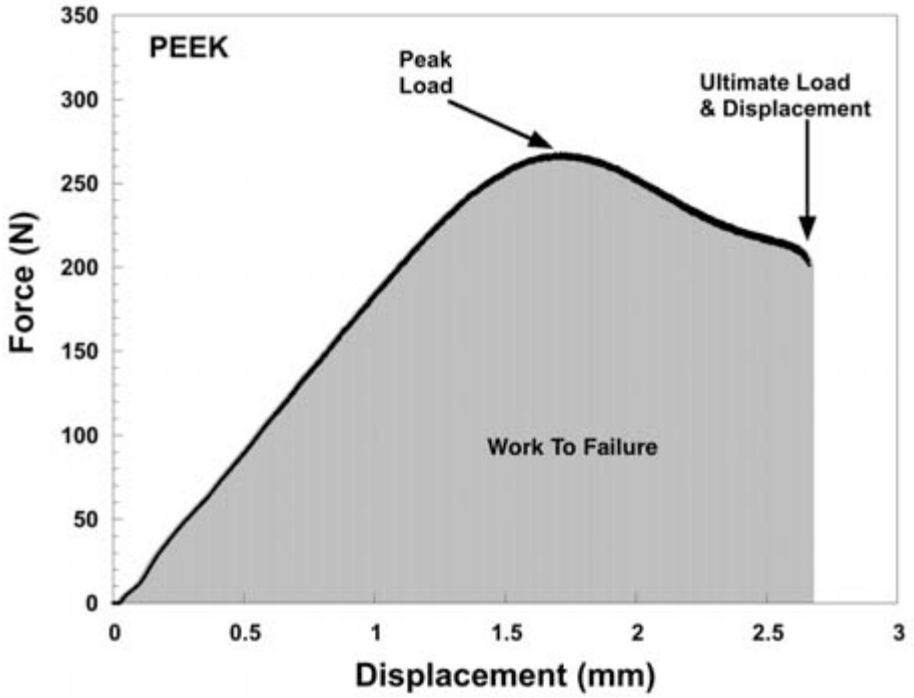

Figure 1-11: A typical load-displacement curve for a small punch test to failure for PEEK biomaterials.

Table 1-1: Average parameter values measured for each PEEK material.

Molding Process	Material Grade	Test	Crystallinity (%)	Peak Load (N)	Ultimate Load (N)	Ultimate Displacement (mm)	Energy (mJ)
Standard	Unfilled	Unannealed	16 ± 5	256 ± 7	222 ± 12	2.80 ± 0.09	505 ± 27
		200ºC	38 ± 4	264 ± 4	212 ± 7	2.67 ± 0.11	494 ± 24
		300ºC	46 ± 2	275 ± 8	188 ± 25	2.44 ± 0.12	458 ± 30
	Image Contrast	Unannealed	15 ± 2	229 ± 3	198 ± 10	2.71 ± 0.09	435 ± 19
		200ºC	40 ± 5	242 ± 6	210 ± 17	2.73 ± 0.19	472 ± 48
		300ºC	47 ± 4	253 ± 5	193 ± 5	2.31 ± 0.18	398 ± 39
High Temp	Unfilled	Unannealed	13 ± 1	242 ± 4	222 ± 14	2.93 ± 0.24	524 ± 56
		200ºC	34 ± 2	248 ± 6	216 ± 21	2.86 ± 0.26	521 ± 69
		300ºC	40 ± 2	258 ± 7	197 ± 61	2.93 ±0.26	525 ± 57
	Image Contrast	Unannealed	14 ± 1	175 ± 34	143 ± 49	1.75 ± 0.72	206 ± 126
		200ºC	34 ± 1	173 ± 36	161 ± 26	1.56 ± 0.57	190 ± 124
		300ºC	42 ± 4	180 ± 44	167 ± 33	1.85 ± 101	185 ± 101

Processing (standard vs. high temp) did not have an effect on crystallinity in unannealed specimens ($p < 0.191$ and 0.199 for unfilled and image contrast PEEK groups, respectively). However, the standard process group was consistently higher than its high-temperature process counterparts when annealed at 200ºC (mean difference = 4%, $p = 0.004$ and 0.002 for unfilled and image contrast grade groups, respectively) and 300ºC (mean difference = 5%, $p < 0.001$ and 0.009 for unfilled and image contrast grade groups, respectively; Figure 1-12; Table 1-1).

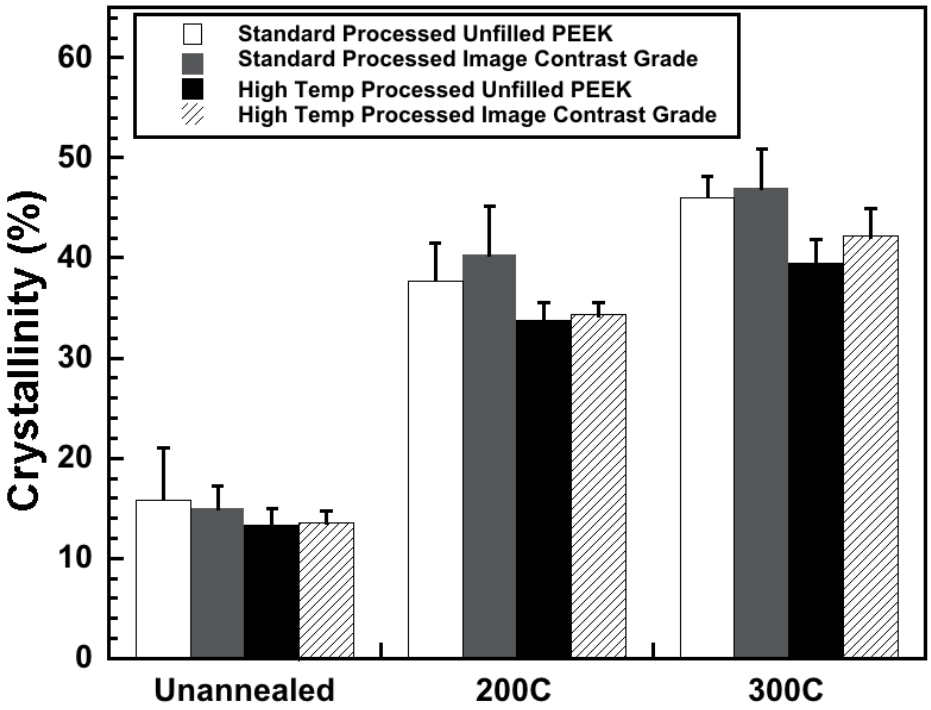

Figure 1-12: The degree of crystallinity in the different PEEK materials and molding processes at each annealing condition.

For standard process on unfilled PEEK, peak load significantly increased from unannealed to 200ºC to 300ºC ($p < 0.02$; ANOVA with post-hoc Tukey; Figure 1-13), while the ultimate displacement significantly lowered across all conditions ($p < 0.03$; ANOVA with post-hoc Tukey, Table 1-1). We observed a significant positive correlation between crystallinity and stiffness in the standard process group (Speaman's Rho = 0.41; $p = 0.001$; Table 1-1). The ultimate load and work to failure decreased across all conditions, but only significantly from the 200ºC condition to the 300ºC ($p = 0.01$ and $p = 0.02$; respectively). The peak load for the standard process image contrast grade PEEK also significantly increased with increased crystallinity ($p < 0.001$; ANOVA with Post-Hoc Tukey

Test), but was lower in all cases when compared to the standard process unfilled grade ($p < 0.001$, T-Test). Ultimate displacement also reduced with increasing crystallinity, but only significantly from 200ºC annealed group to the 300ºC (mean difference: 0.45 mm; $p < 0.001$). In addition to peak load, the ultimate load, ultimate displacement, and work to failure were significantly lower for standard process image contrast PEEK samples in the unannealed state in comparison to unfilled PEEK samples (Table 1-1). For the standard process group, all of the fracture surfaces appeared ductile in nature (Figure 1-14A&B), but as annealing temperature raised for both grades, the fractures had increased crack propagation, more brittle appearance, and less plastic deformation, especially in regards to the image contrast grades (Figure 1-14C&D).

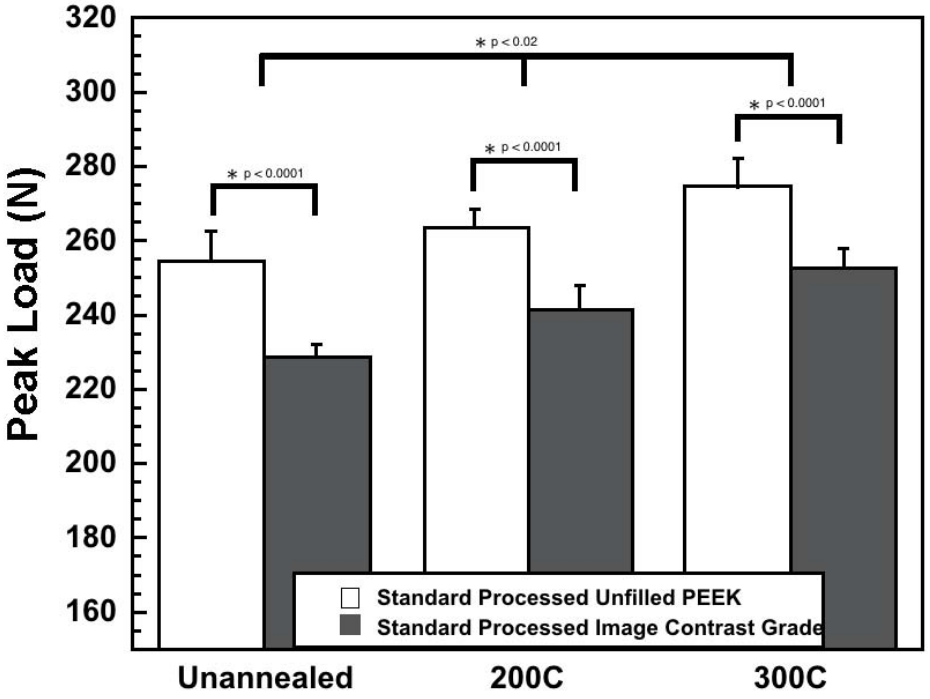

Figure 1-13: The average peak load in the standard process PEEK grades at each annealing condition.

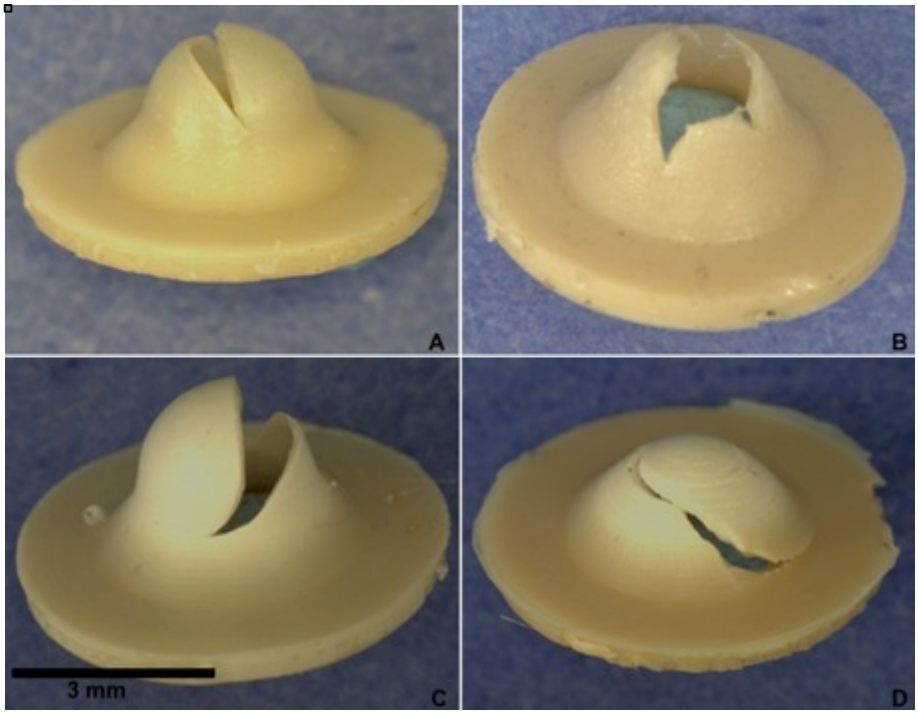

Figure 1-14: The fracture pattern for the standard process group when unannealed was a bubble deformation failure for both unfilled PEEK Optima (A) and image contrast grade (C), but the facture surface appeared more brittle in nature after being annealed at 300ºC in both unfilled PEEK Optima (B) and image contrast grade (D).

Among the high-temperature molded samples, substantially greater variability in the mechanical properties were observed, and was more apparent in the image contrast grade of PEEK. For high-temperature process unfilled samples, peak load was significantly different and increased with crystallinity ($p \leq 0.05$; ANOVA with post-hoc Tukey test). No significant difference was detected for peak load with the image contrast material ($p = 0.81$; Kruskal-Wallis Test). Similarly, no significant difference was observed for ultimate displacement, ultimate load, or work to failure with either material ($p > 0.247$ Kruskal-Wallis Test). However, all these metrics were significantly lower for the image contrast grade as compared to unfilled PEEK ($p \leq 0.004$, T-test). The high-temperature

process groups also display two distinct fracture morphologies for each material grade and correlated to two distinct load-displacement patterns (Figure 1-15). For unfilled PEEK, an open top fracture pattern (Figure 1-15A) was associated with a shortened plastic deformation phase and failure soon after peak load was achieved. The second facture pattern was bubble deformation with a crack and failure along the top edge (Figure 1-15B), which had a similar load displacement pattern to the standard process samples. Despite the distinct fracture surfaces, there was no observed difference in the metrics of the small punch test between the two patterns.

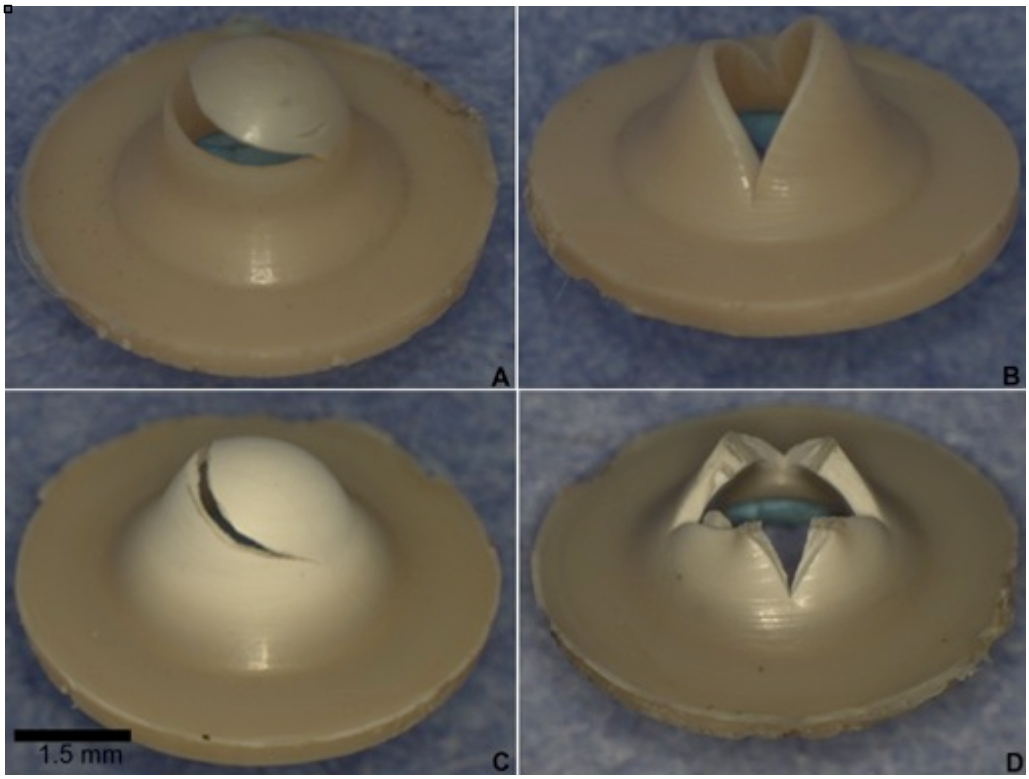

Figure 1-15: The higher temperature molding process yielded two fracture patterns for each material grade. Unfilled PEEK had a bubble deformation with crack fracture (A) and an open top fracture (B), while the image contrast grade had a similar bubble deformation with crack (C) and a brittle star fracture (D).

The high temperature process image contrast grade samples similarly exhibited two predominant fracture patterns, including bubble like specimen geometry prior to fracture (Figure 1-15C). A second more brittle, star-like facture (Figure 1-15D) was observed in the image contrast samples and was associated with a lower peak load ($p = 0.009$) with little to no plastic stretching of the material. The image contrast grade fracture patterns showed a difference between all annealing groups in regards to peak load, work to failure, and ultimate displacement (Figure 1-16A&B).

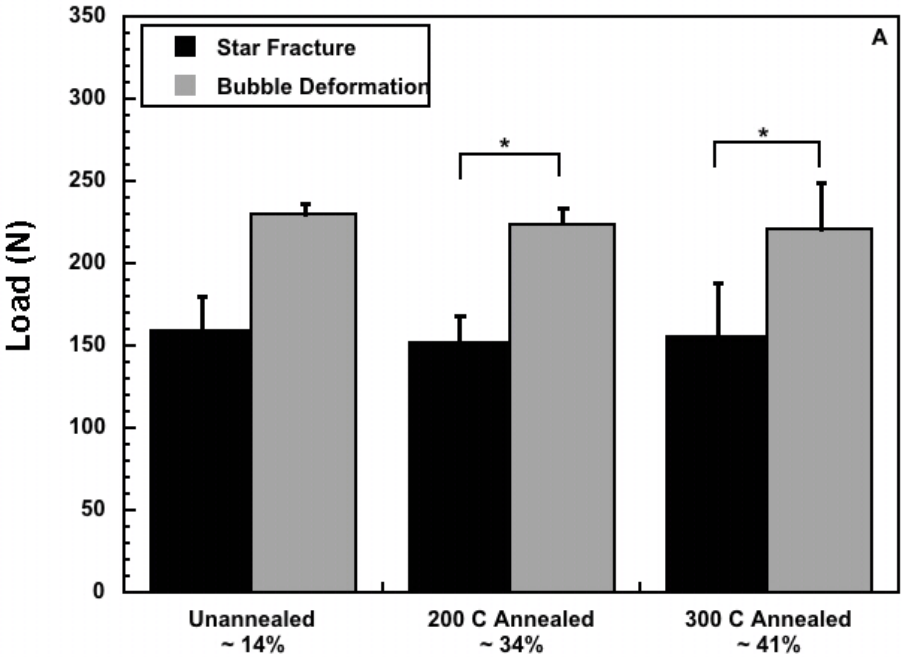

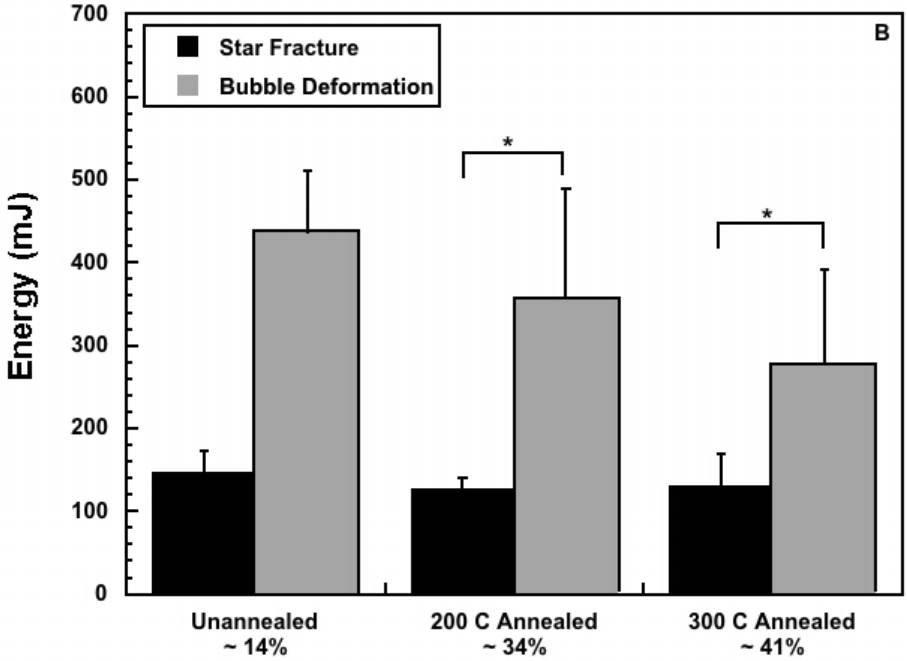

Figure 1-16: The two fracture surfaces of the standard process image contrast grade of PEEK produced distinctly different results in mechanical behavior in regards to peak load (A) and work to failure (B). Percentages shown are the average crystallinity.

When the standard process was applied during molding, it generally enhanced the observed mechanical properties when compared to the high temperature molded grades (Table 1-1, Figure 1-13). The standard process image contrast material yielded significantly higher values for all measured metrics than the high-temperature counterpart ($p \leq 0.023$). The main distinguishing feature between the unfilled PEEK groups is the standard process materials had a significantly greater peak load. No voids or defects were observed on samples after visual inspection with light microscopy or SEM.

Cyclic Testing Results

Previous to cyclic testing, small punch samples were loaded to an incrementally increased load. Before each load increase, the samples were inspected for any signs of deformation. It was noted that at a load >30N, a small indentation of the material would occur. Thus, for subsequent cyclic loading, a load range of 0.5 to 15N was set to ensure all testing was within a linear elastic region of the material. The load-displacement behavior remained relatively similar during cyclic loading with approximately 0.005 mm of creep (Figure 1-17). A high linear correlation for stiffness values was noted on all cycles (R^2 = 0.998 ± 0.002); however, a lower stiffness, and thus a lower elastic modulus, was observed in both the first cycle and in the test to failure as compared to the last nine cycles with a mean difference of 7.2% and 8.0% respectively (Table 1-2). The average modulus value for the last 9 cycles was approximately 4.2 ± 0.3 GPa (Table 1-2). Cyclic loading did not significantly affect peak load as compared to the unannealed samples (p = 0.1).

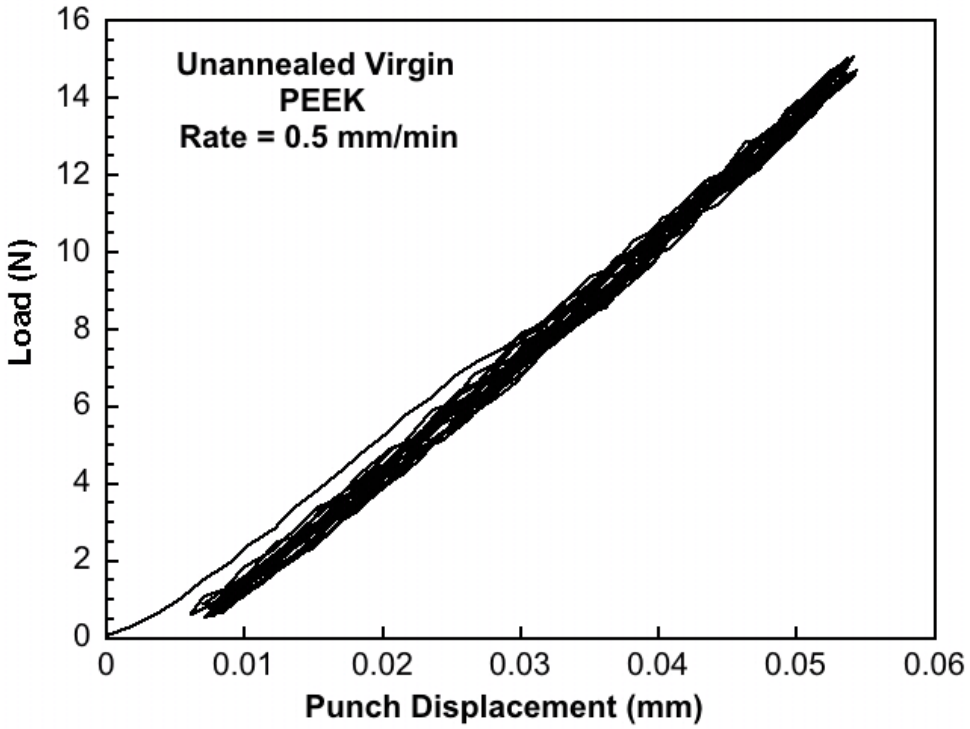

Figure 1-17: Load and displacement patterns for PEEK small punch test samples after being cyclically loaded to 15N for 10 cycles.

Table 1-2: Elastic modulus results calculated from small punch samples after cyclic loading and full small punch test.

Sample Grade	Elastic Modulus (GPa)			
	1st Cycle	Full Small Punch Test	Average of Last 9 Cycles	Difference from 1st Cycle (%)
Unfilled PEEK	3.96	3.79	4.21 ± 0.09	5.89%
	4.52	4.54	4.85 ± 0.04	6.82%
	4.40	4.09	4.70 ± 0.05	6.44%
	4.13	4.14	4.44 ± 0.03	7.04%
	3.98	4.23	4.42 ± 0.04	9.85%

Discussion

The results of small punch testing supported our original hypotheses as the image contrast agent significantly lowered the yield and ultimate strength of the PEEK. Additionally, an increase in crystallinity generally resulted in lower ultimate displacement and work to failure in both the standard process and high-temperature PEEK. Molding process, filler material, and crystallinity significantly impacted the mechanical behavior of PEEK and was effectively characterized by the small punch test. The small punch test metric most affected by changes in the material thermal treatment was peak load and to a lesser extent ultimate displacement. Higher peak loads imply a larger resistance to the start of plastic deformation (i.e., yielding), whereas ultimate displacement categorized the ductility and the extent of deformation before failure.

Previous studies of PEEK have shown an increase in elastic modulus and tensile strength with increasing crystallinity. However, this also confers a reduced toughness [77, 103]. Higher toughness is linked to lower levels of crystallinity since crack propagation occurs more readily in crystalline regions [77]. This could explain the more brittle appearance and crack formation on the 300ºC-annealed samples of the materials. At reduced crystallinity, PEEK materials could exhibit yielding at lower loads, but at a high level of crystallinity, the material reduces the potential for plastic deformation and has an increased likelihood of brittle fracture during the small punch test.

The small punch test was also sufficiently sensitive to distinguish variations between the two PEEK manufacturing processes tested in this study.

The higher temperature molding process was utilized to measure the robustness of the small punch test, but also to highlight the impact of improper molding on the final product. Molding outside of the optimal temperature range of PEEK could cause thermal degradation or irregularities [80]. The higher temperature molding process yielded lower peak loads for the materials and greater ductility for unfilled PEEK. It is noteworthy that crystallinity in the high temperature process materials is significantly lower in the 200ºC and 300ºC groups, which could influence the differences seen in peak load between the processing conditions. While taking this into consideration, it still seems unlikely to be an influential factor since the differences were still apparent when samples were unannealed. In addition, the crystallinity differences were only 3-4% within each material type, while the peak load in the high-temperature process group at 300ºC was similar to unannealed standard process material and significantly lower than the corresponding 300ºC values by 17 N.

PEEK performed similarly to previous studies on small punch testing with UHMWPE, but the load-displacement curves for PEEK often lack the ultimate load forming a second peak load and have less overall deformation. This deformation can decrease even more if crystallinity is increased towards 46%. In previous studies by Stober et al. (1984) and Chivers and Moore (1994), they reported an increase in elastic modulus with increasing crystallinity in tensile testing, and a drastic increase modulus with dynamic mechanical testing in tension [77, 104]. Elastic modulus is proportional to stiffness characterized by the small punch test [102], and similar to other mechanical testing results, the

small punch test results had a positive significant correlation between crystallinity and stiffness in the standard process group on both materials. We also observed lower values for the metrics of the image contrast grade as compared to unfilled PEEK. A similar trend is observed in the reported tensile properties by Invibio, ltd [105], but peer-reviewed studies on 20% $BaSO_4$ filled PEEK composite are not yet available. However, Bakar et al. (2003) have studied the mechanical influence of rigid spherical additives (hydroxyapatite) in a PEEK matrix with a similar reduction in tensile strength and strain with increasing filler content [106, 107]. Often this effect is explained by poor interfacial bonding, so as the particles debond from the matrix during testing, a lower percentage of the material carries the load and can experience stresses at failure levels with less load than the unfilled material [107]. In addition, the hydrophobic nature of thermoplastic polymers like PEEK can prevent proper interfacial bonding with hydrophilic fillers [108].. Methods have been developed to increase bonding of the PEEK matrix to additives such as sizing the filler for bonding. In alternative attempts, the strength of hydroxyapatite composites were increased by changing the morphology of the particle from spherical in nature to a whisker [82].

Cyclic pre-condition of PEEK confirmed a region of linear elastic behavior below 0.6 mm of displacement. Linear load-displacement curves were repeatedly observed in all cycles, but lower modulus values were consistent in the first cycle of cyclic loading and when compared to the stiffness from full small punch tests. Elastic modulus and stiffness may be calculated from the small punch test but only after cyclic conditioning can an accurate value for modulus be

determined. The initial variability in the test when encountering low loads and minimal displacements can influence calculation of modulus. In addition, the full small punch test does not have the benefit of accuracy of the extensometer that could influence the modulus calculated when testing to failure.

We acknowledge several limitations to the current study. The focus of the study design was to examine the feasibility of small punch test for the evaluation of PEEK biomaterials. Therefore, all the present testing was performed on stock materials that have not been exposed to various sterilization techniques nor have they been molded or machined directly into an implantable design. Due to the small dimensional requirements, we infer the applicability of the small punch test on as-manufactured implants, so, in moving forward in this research, testing will be repeated on retrieved and off the shelf implant designs. In addition, the work presented was performed on only 2 of the implantable grades of PEEK. Carbon fiber reinforced grades are also commercial available, and new PEEK composites, like hydroxyapatite or calcium silicate modified PEEK, are continuously being developed [82, 109]. Each filler materials could impose unique molding and machining restrictions on PEEK and impact the applicability of the materials in regards to the small punch test. Thus, the additional research is necessary to confirm the applicability of the small punch test to a broader range of PEEK biomaterials.

Conclusion

Internationally, the small punch test has been incorporated in to standards of testing for UHMWPE biomaterials (e.g., ASTM F2183), and the results of this study suggest that small punch testing may also be a promising testing technique for standardized testing of PEEK biomaterials. Though not directly correlated to larger scale mechanical testing, such as uniaxial tensile testing, because of its multi-directional nature, the small punch test is able to detect alterations in the mechanical behavior with only a small amount of material required for analysis. This testing technique will enable future studies of fillers, processing changes, and degradation without the creation of bulk test samples. The small punch test provides a repeatable and reproducible method for measuring changes and variability in PEEK implant designs.

2. Evaluate Antimicrobial Activity and Elution Kinetics of Ag Particles and Develop an Analytical Model for the Release of Ag from a PEEK Matrix

Abstract

To study the antibacterial properties of Ag particles and determine the influence of particle diameter, 7 silver particles were examined through minimum inhibitory concentration (MIC) testing on Ag-dispersed agar gels. Inhibitory testing revealed a size-dependent effect on the reduction of bacterial growth. Ag particles >8μm in diameter exhibited little to no effect on bacterial growth, while the smallest particles (100 nm, nanoAg) displayed complete inhibition at lower concentrations. The increased bactericidal effects were due to larger surface area to mass ratio exposing more surface atoms for the oxidation of Ag^0 to Ag^+. This concept was confirmed after additionally observing significant bacterial inhibition with a larger diameter particle (8 μm) that was designed with a porous structure to have a similar surface area to mass ratio as 100 nm particles (5 m^2/g). Using the properties of the nanoAg or μAg particles, a model for Ag incorporation into PEEK was developed by combining known models for the oxidation of Ag^0 to Ag^+, Fickian case I diffusion of H_2O into PEEK, and the Higuchi method of drug release from a solid polymer. The idealized model predicted Ag^+ release at levels above MIC for *E. coli* and *S. aureus* when PEEK matrices were incorporated with ≥1% of Ag particles.

Introduction

Ag particulates are increasingly incorporated into biomaterials, such as polyurethane urinary catheters, or applied as surface coatings to reduce the incidence of periprosthetic infection [43, 45, 46]. Specifically, nano-diameter (10-100nm in diameter) pure Ag particles are of interest due to increased antimicrobial activity compared to larger diameter counterparts [37, 44, 51, 71, 110-112]. Small diameter particles have an increased surface area to mass ratio (m^2/g), which, in theory, leads to an elevated volume of surface atoms accessible for oxidation of Ag^0 to Ag^+ [48, 49, 65, 69, 113]. Nanoparticles also have lower redox potentials and are more vulnerable to oxidation [69]. The primary species thought to be responsible for antimicrobial activity of Ag is Ag^+; hence, the elevated reactivity of nanoparticles increases Ag^+ release into the surrounding environment. The size-dependent effect has been primarily documented for particles suspended in solution, and how diameter effects persist within a polymer matrix is unknown.

Zhang et al. proposed that the production of Ag^+ occurs through an oxidation reaction dependent on dissolved oxygen concentration ($[O_2]$) and pH ($[H^+]$) (Eq. 4) [65]:

$$Ag_s + \frac{1}{2} O_{2(aq)} + 2H^+_{(aq)} \leftrightarrow 2Ag^+_{(aq)} + H_2O_l \quad \text{(Eq. 4)}$$

The reaction, based on hard sphere collision theory, models the molecules in the reaction as rigid spheres colliding. This concept has been previously used to explain the dissolution kinetics of various nanoparticles [51, 65, 69, 70, 114]. The reaction equation was derived from earlier studies in which the pH or O_2 were varied to observe Ag^+ release. As pH was incrementally decreased from 9 to 4, Ag^+ release significantly rose due to the elevated levels of H^+ [70]. Reduced pH has previously been linked to positively influencing oxidation with other nanoparticles such as ZnO [114]. Enhanced inhibition of E. coli growth was also observed when Ag nanoparticles were incubated in a solution that was O_2 enriched [48]. The oxidation process, however, is most likely not a direct electron transfer in which O_2 is reduced to H_2O, but through more common reactions producing peroxide (H_20_2) intermediates. The reaction between Ag and H_20_2 is so rapid, though, that the initial oxidation between Ag particles and O_2 is the rate-limiting step, and therefore, is the focus of the reaction [70]. Finally, NaCl concentration in solution should not be a limiting factor for the oxidation reaction of Ag to Ag^+. Salt concentration increases particle aggregation in the media but does not directly affect reaction kinetics [70]. Aggregation decreases surface area and depresses the number of exposed atoms at the grain boundaries, thus lowering Ag^+ production [48, 49, 65, 113].

Using theoretical reaction kinetics for Ag, Zhang et al. developed an equation for Ag^+ release rate by assuming small Ag particles act as soluble reactants. The overall reaction was described with Arrhenius law for temperature dependence ($k=Ae^{-Ea/RT}$) and first order reaction kinetics [65].

$$\gamma_{Ag^+} = kC_{AgNPs}[O_2]^{0.5}[H^+]^2 \quad \text{(Eq. 5)}$$

where γ_{Ag^+} is the Ag^+ release rate (mol/l*hr), and k is the reaction rate constant. By inclusion of constants and integration of the equation, Zhang et al. produced a model to predict concentration of Ag^+ released by Ag particles:

$$[Ag^+]_{released} = [Ag]_{initial}\left[1 - \exp(-a * t)\right] \quad \text{(Eq. 6)}$$

and $$a = \frac{3}{4}\left(\frac{8k_BT}{m_B}\right)^{1/2} \rho^{-1} \exp\left(\frac{-E_a}{k_BT}\right) r^{-1}\left[O_2\right]^{0.5}\left[H^+\right]^2$$

where $[Ag]_{initial}$ is the initial concentration of Ag particles in solution, k_B is the Boltzmann constant, m_B is molecular weight of dissolved oxygen, ρ is the density of Ag, E_a is the activation energy, r is the radius of the particle, $[O_2]$ is the dissolved oxygen concentration, and $[H^+]$ is the hydrogen ion concentration. To optimize the model, Zhang et al. fitted elution data from nanoparticles ranging from 20-80 nm in diameter at concentrations from 300 – 600 µg/l for the unknown factor, E_a. The model generated framework for the development of a predictive model for Ag^+ release in any environment.

The purpose of the following study was to determine which commercially available Ag particulates are most effective against common bacteria causing periprosthetic infection. Futhermore, we asked if there is a size dependence of the antimicrobial properties. For the most effective particles, the study also characterized elution profiles to develop an idealized model for Ag^+ elution from PEEK and predict effective Ag loadings.

Methods and Materials

Antimicrobial Activity of Ag Particles

To determine antimicrobial activity of Ag particles and the optimum additive for Ag-PEEK composites, commercially available Ag products were compared. After evaluating multiple sources for thermal stability, viable options were narrowed to 7 formulations:

- Nanoparticle Ag
    - 80-100nm diameter (99.9%trace metal basis,)
    - <150nm diameter (99.5 % trace metal basis)
- Micro-particle Ag
    - 5-8μm diameter (99.9 % trace metal basis)
    - <45μm diameter (99.99% trace metal basis)
    - <250μm diameter (99.99% trace metal basis)
- Marketed antimicrobial Ag
    - Biogate – HyMedic 4000 (Smart Silver)

- 3.5 –18 μm diameter (99.9% elemental Ag)
  - Micro-diameter particle, but porously designed to have specific surface area similar to 100nm particle ($5m^2/g$).
- Industrially designed Ag particle for use in medical polymers, but never used with PEEK.

- Miliken SelectSilver® Zr2k
  - 1.3 μm diameter
  - Ag sodium hydrogen zirconium phosphate (10% Ag)
  - Industrially designed Ag composite for use in medical polymers, but also never used in a polymer like PEEK

The antimicrobial properties of each of the Ag particulates alone were measured using an experiment adapted from the Clinical Laboratory Standards Institute (CLSI) M11-A7 document on quantifying the minimum inhibitory concentration (MIC) of antibiotic compounds. The seven Ag particulates were cured in Agarose gel (Agar) with Tryptic Soy Broth (TSB) in 35mm petri-dishes in two concentrations: 2 mg/ml and 200 μg/ml. Each plate was challenged with 100 μl (10^5 cfu/ml) of *S. aureus* ATCC 25923 or *E. coli* ATCC 25925, and incubated for 20hr. Ag-Agar plates were compared to full growth on standard agar. Four agar samples were tested in each trial, which were repeated 4x to verify results.

Ion Release from Ag Particles

To study Ag^+ release from antimicrobial Ag particles, the most effective Ag particles from the Agar tests were incubated in 500ml of phosphate buffered saline (PBS) at a concentration of 1 mg/l at 37°C. Every 24 hr, 4 ml of fluid was removed, and Ag^+ was separated from Ag particles using Amicon Ultra-4 centrifugal filter units (Amicon Ultracel 3K, Milipore, USA, mean pore size of 1-2 nm). On day 1, samples were also collected at 0, 4, and 12hr time points. After centrifugation for 70 min at 3500 x g, fluid was stored at 4ºC for analysis. Ag^+ concentrations were calculated by atomic absorption spectrometry (model AA240-FS, Varian Techtron Pty Ltd., AU). Concentrations were interpreted from absorbance values through a linear interpolation of a standard dilution curve derived from solutions of known $[Ag^+]$ ranging from 0.05 ppm to 10 ppm. Dissolved oxygen (DO) and pH were monitored every 72 hr with a pH multimeter (Orion 5 Star Plus, Thermo Scientific) and/or DO probe (Orion 091010MD, Thermo Scientific) to monitor any changes in $[H^+]$ or $[O_2]$ in the media.

Results and Discussion

Antimicrobial Activity of Ag Particles

The larger particles, 45 μm and 250 μm, exhibited no effect on the bacteria at either concentration (Figure 2-1). The 5-8 μm particles (Figure 2-1A) inhibited *S. aureus* colonization at 2 mg/ml, but full growth was observed at the lower concentration. The 150nm, HyMedic, Zr2k, and <100 nm either expressed

no growth or very trace amounts of bacteria at 2 mg/ml (Figure 2-1E-H). The 150 nm (Figure 2-1E) particles showed no reduction of bacterial growth at 200 µg/ml; however, the 100nm, the HyMedic 4000, and the Zr2k, had the most reduction of growth at the lower concentration. Overall, the 100 nm particles had the least bacterial growth of all the particles at the 200 µg/ml. These results were mirrored when repeated with *E. coli*. Extensive images of bacterial reduction on agar gels are shown in Appendix B for both S. *aureus* and *E. coli*.

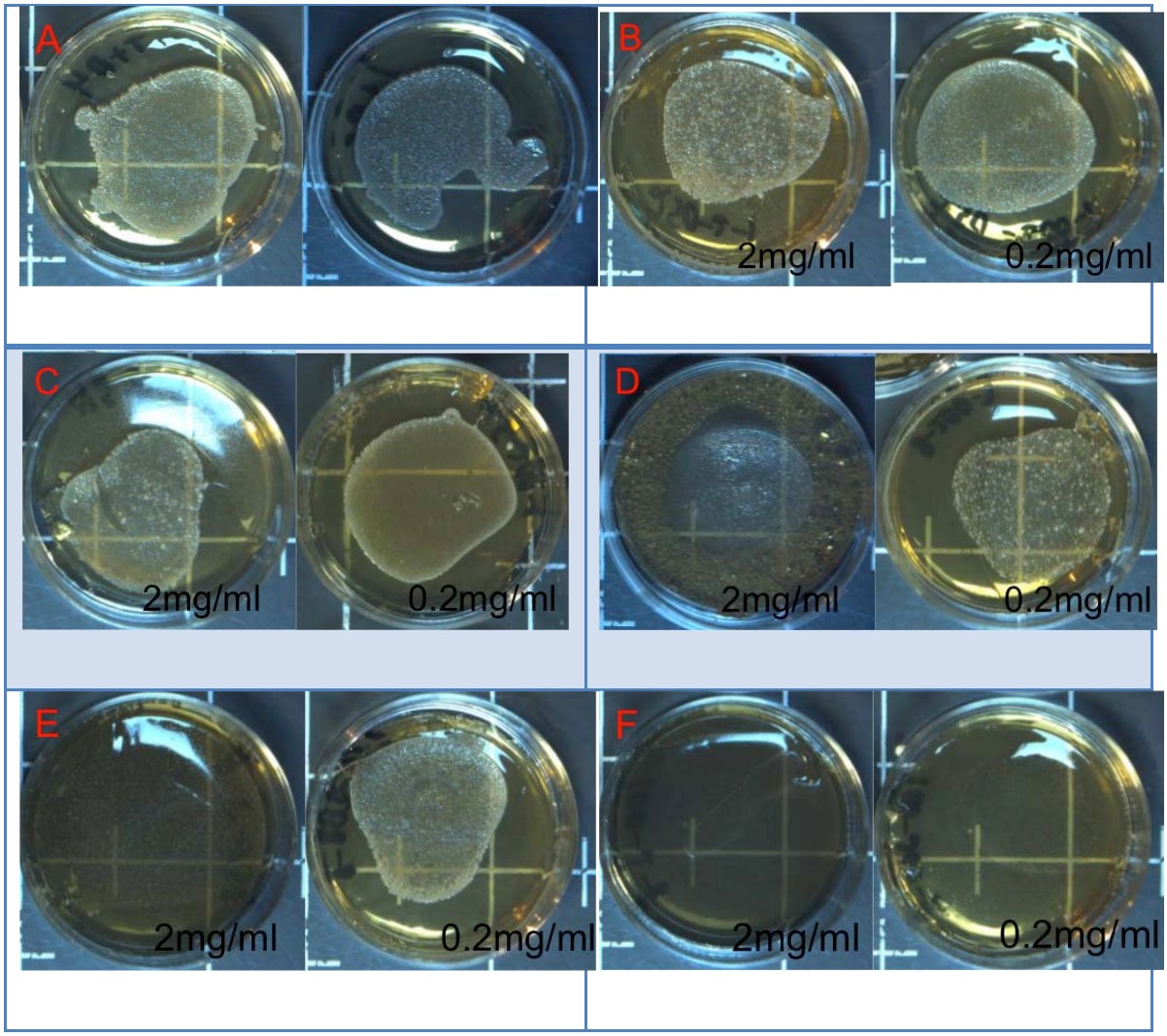

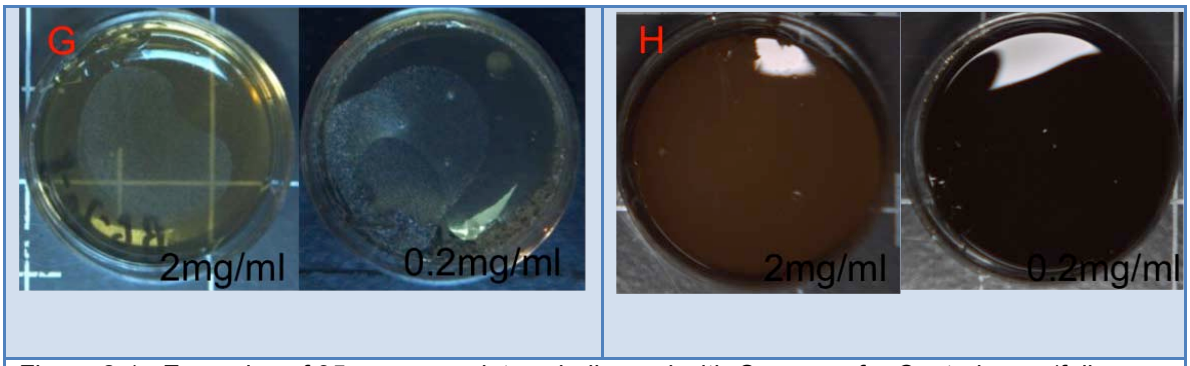

Figure 2-1: Examples of 35 mm agar plates challenged with *S. aureus* for Control agar (full growth) (A), 250 µm diameter (B), 45 µm diameter (C), 5-8 µm diameter (D), 150 nm diameter (E), 100 nm diameter (F), BioGate HyMedic 4000 porous micron diameter (G), and Zr2k particles (H). Entire sets of agar plate images are listed in Appendix B.

Elemental Ag can come in various formations and particle sizes. For antibacterial purposes, it has been often assumed that nano-sized Ag particles will be more effective against microbes than larger counterparts. Antimicrobial testing was modeled after standard minimum inhibitory concentrations (MIC), which, in many models, were performed in aqueous solution with growth media. For Ag particulates, standard testing is difficult because with time, the larger and thus heavier particles can subside from the media and give a misrepresentation of the inhibitory activity due to the Ag^{+} not being uniformly distributed through the media. This effect has even been seen when incubating overnight with shaking or agitation. Future objectives are to uniformly integrate the Ag with a polymer matrix, therefore; Ag in solution was far from the intended environment. Standard MIC studies conducted on solidified Agar gels were modified so the selected Ag particulates were set in the agar at specific concentrations. Despite the different base material, this was a better facsimile of the Ag-polymer environment and still conformed to MIC tests used on antibiotics. Furthermore,

the 2mg/ml concentration corresponded to a low weight ratio of Ag in PEEK (0.00154 or 0.15%) and illustrated the antibacterial properties of Ag particles at lower concentrations than Ag filler ratios in current applications [29, 45, 46, 76, 115].

The <100nm particle (nanoAg), porous micro-sized Ag (μAg), and phosphate-Ag composite (Zr2K) displayed the highest inhibition of bacterial growth. For pure Ag particles, inhibition increased as particle diameter reduced as shown by the smallest particle (nanoAg) exhibiting the highest inhibition. Bacterial reduction on μAg agar suggested that antimicrobial properties were linked to increased available surface area because μAg and nanoAg have the same mass to surface area ratio (5 m^2/g) but different diameters. Smaller particles have larger surface area ratios, and hence, more surface atoms accessible for oxidation of Ag^0 to Ag^+. The results show nanoAg, μAg, and Zr2k would be the best candidates for incorporation into a PEEK matrix.

Model Development with Water Diffusion

For PEEK that has been blended with Ag, release of Ag^+ from the substrate follows a 3-phase process (Figure 2-2). First, there is an influx of water into the matrix, followed by the oxidation reaction of Ag to Ag^+ within the polymer, and finally, incongruence with the other processes, diffusion of Ag^+ from the matrix.

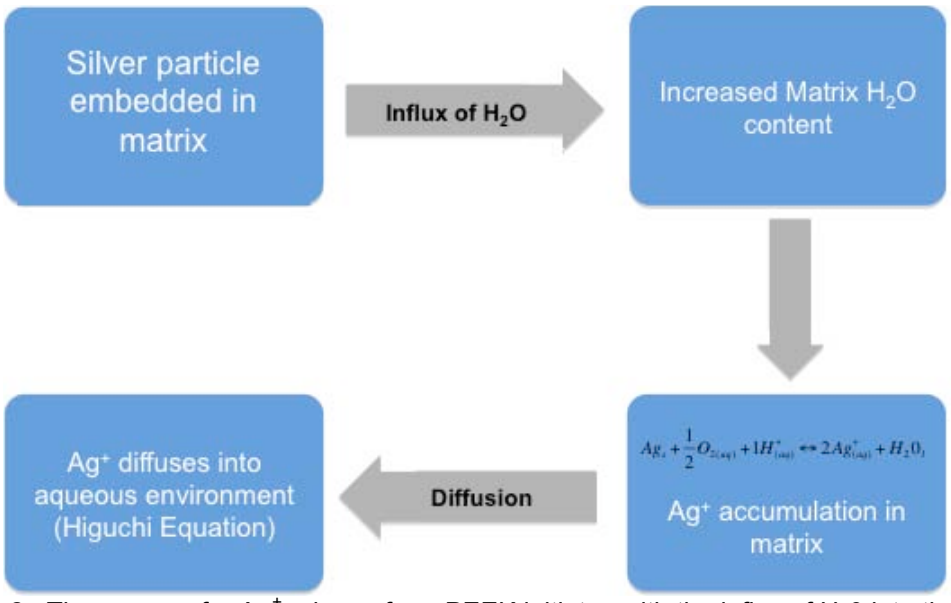

Figure 2-2: The process for Ag^+ release from PEEK initiates with the influx of H_20 into the polymer matrix. When exposed to O_2 and H^+ from H_20, the Ag particles begin an oxidation reaction to form Ag^+, which is subsequently released from the matrix, and modeled by the Higuchi equation.

The Ag oxidation reaction has been modeled, as shown in the previous section in Eq. 6 by Zhang et al., and was dependent on the concentration of O_2 and H^+ in the aqueous environment [65]. Water diffusion into PEEK has been studied extensively in the literature and is defined by Fickian Case I diffusion,

$$\frac{M_t}{M_\infty} = x1 = 1 - \sum_{n=0}^{\infty} \frac{8}{(2n+1)^2 \pi^2} \exp\left(\frac{-D(2n+1)^2 \pi^2 t}{\ell^2}\right) \quad \text{(Eq. 7)}$$

where, D is the diffusion coefficient, l is the thickness of the material, t is time, and M_t/M_∞ is the ratio of mass of water absorbed at time "t" equilibrium mass of absorbed water [103, 116]. Final portion of Ag^+ release is defined by diffusional release of a drug from a polymer matrix. The Higuchi Theory is able to define diffusional release from a solid polymer matrix in a spherical, a cylindrical, or, in

the purposes of this study, a slab configuration [117, 118]. The Higuchi model is based on the solid drug (in this case, Ag) first dissolving and diffusing from the surface layer of the polymer, and once this layer is exhausted, diffusion from the next layer continues. To use this model, four assumptions must be made:

- A pseudo steady-state exists
- The drug particles (Ag^+) are small compared to average distance of diffusion
- The diffusion coefficient of drug in polymeric matrix (D_p) is constant
- External medium is immiscible with the matrix and constitutes an infinite sink

The general model is defined by:

$$Q_t = \frac{M_t}{A} = \left[D_p t C_p \left(2C - C_p \right) \right]^{1/2} \quad \text{(Eq. 8)}$$

where C is total concentration of drug, which comprises solid and dissolved drug (i.e., a 10w/w% in PEEK would be 0.142 g/ml), D is the diffusion coefficient of Ag^+ out of PEEK, A is the total surface area of the slab, and C_p is the solubility of drug in polymer or the amount of drug dissolved and available for release [117, 118]. In the case of Ag-PEEK matrix, C_p would be related to the amount of Ag^+ available in the matrix. Depending on the oxidation potential of the Ag and surface concentration, there could also be a “burst” effect within the first few hours of incubation in water. However, rapid oxidation of surface would have to be substantially greater than potential release of Ag^+ from immediately below the surface and center of the material to have an observable effect.

To explore this process further, a model was generated in MATLAB (MATLAB R2011a, MathWorks, Inc.) to mimic the model created from Zhang et al. on the basis of Eq. 6 [65]. Using parameters from Zhang et al., an estimate of E_a, the activation energy, was calculated to be -5.5×10^{-20} J. A value of k_B of 1.38×10^{-23} $m^{2}*kg*s^{-2}*K^{-1}$, Ag density of 10.5 g/cm^3, and molecular weight of O_2 (m_B) as $2*15.999*1.66 \times 10^{-24}$ g was used for all calculations. The Matlab script is detailed in Appendix C1. For comparison, the activation energy for AgBr is approximately -4.6–5.31×10^{-20} J [119]. $Ag_{intital}$ was found to be 45 µg/l by Zhang et al., when the actual initial concentration was 600 µg/l. Our new model was able to generate the same results using data from the Zhang et al. paper (Figure 2-3).

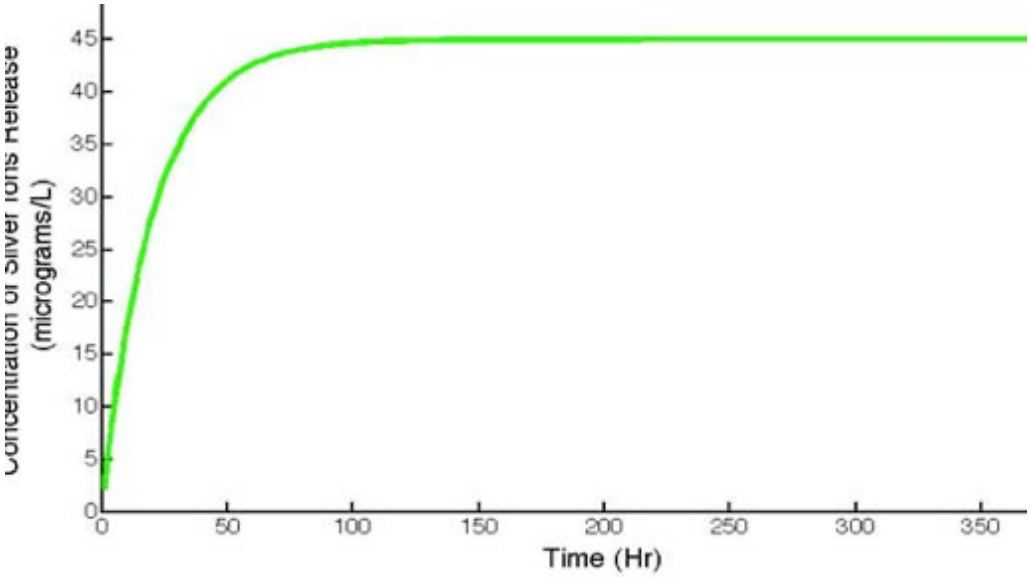

Figure 2-3: Initial model of Ag to Ag^+ oxidation reaction reproduced the analytical predictions from Zhang et al.

$Ag_{initial}$ defined the upper limit of the elution. If changed to 600 µg/l, the curve would slowly approach 600. Fluctuating 0_2 values within relevant values (5 to 10

mg/l) did not affect the release profile. However, changes in pH influenced the rate of production as pH of 7 was approached (Figure 2-4).

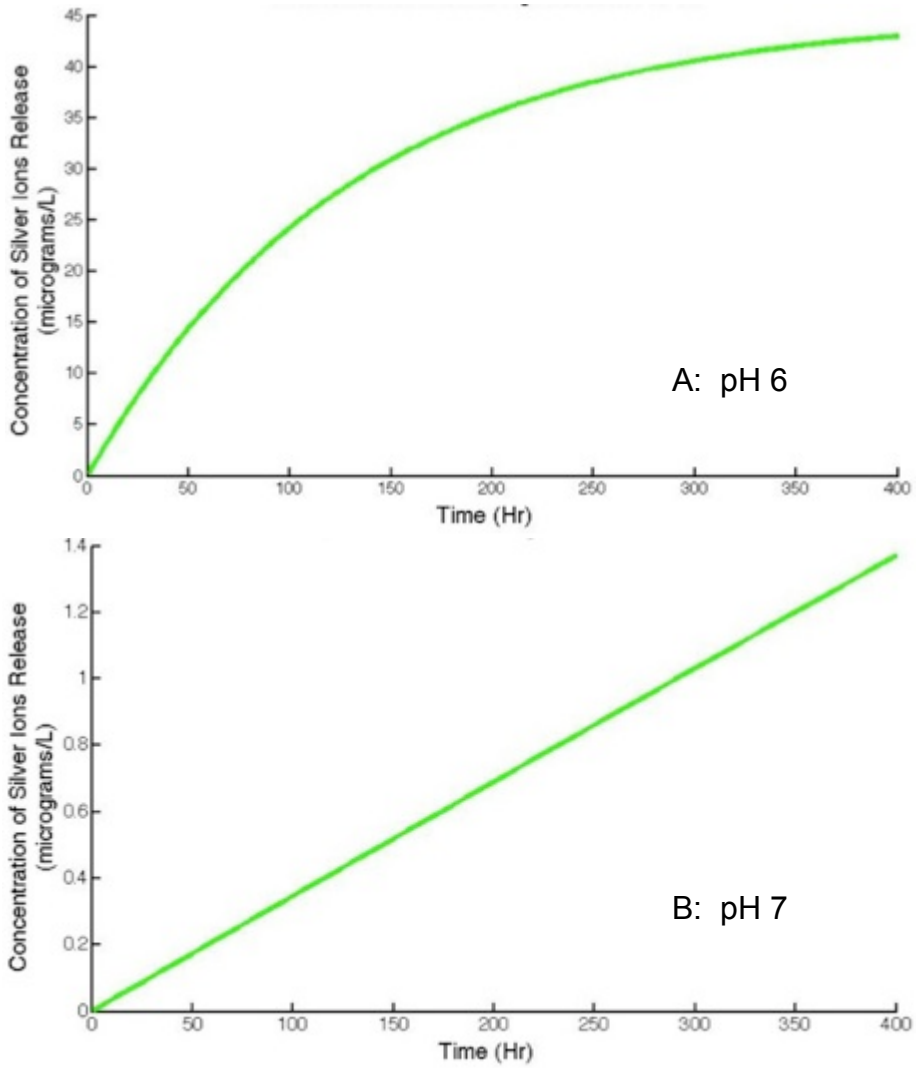

Figure 2-4: Modeling of Ag to Ag^+ oxidation reaction based on the model from Zhang et al. for pH 6 (A) and pH 7 (B).

On the same time scale, Ag^+ production was more linear but at a lower magnitude at increased pH; however, if the time scale was expanded to 20,000hr, the model followed a similar profile as the lower pH.

Based on the Higuchi Theory (Eq. 8), the model characterized elution using an initial Ag concentration in the matrix, C, of 0.142 g/ml (equivalent to 10 w/w% Ag-PEEK composite, a diffusion coefficient, D, representing the diffusion of water out of PEEK (D=0.000044 cm^2/h), a total surface area (A) of 4.32 cm^2, and the solubility, C_p, of 0.00646 g/ml (0.4% of C) (Figure 2-5).

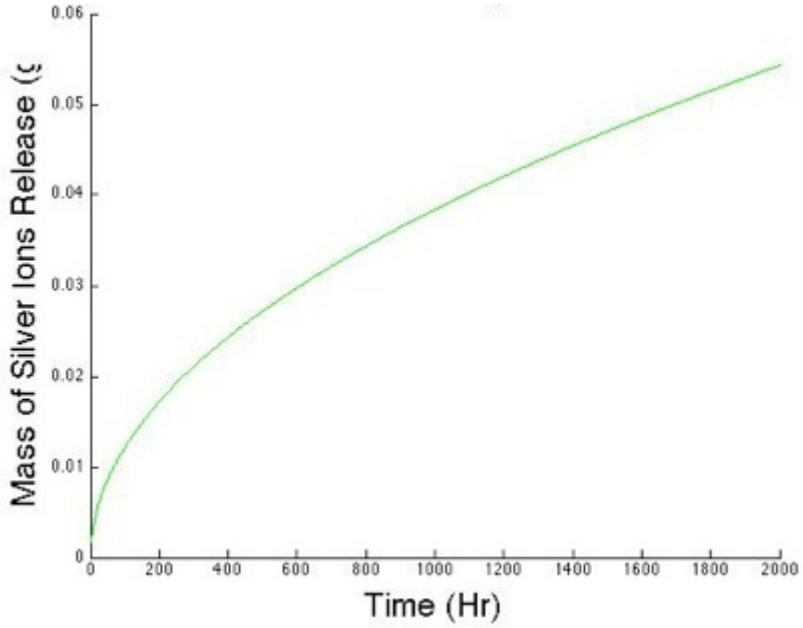

Figure 2-5: Elution pattern for Ag^+ from PEEK based on a constant value for drug solubility, C_p.

If the Zhang et al. equation is incorporated into the model as solubility of the drug, C_p, when pH is increased closer to physiologically relevant levels (7.3), and O_2 level is halved from physiologic standards to 0.0034 g/l, the model release of Ag^+ becomes more linear than the previous iteration (Figure 2-6) [65, 117]. This model was also based on nanoparticles in diameter range of 80-100nm because this size range exhibited the most antibacterial potential previously.

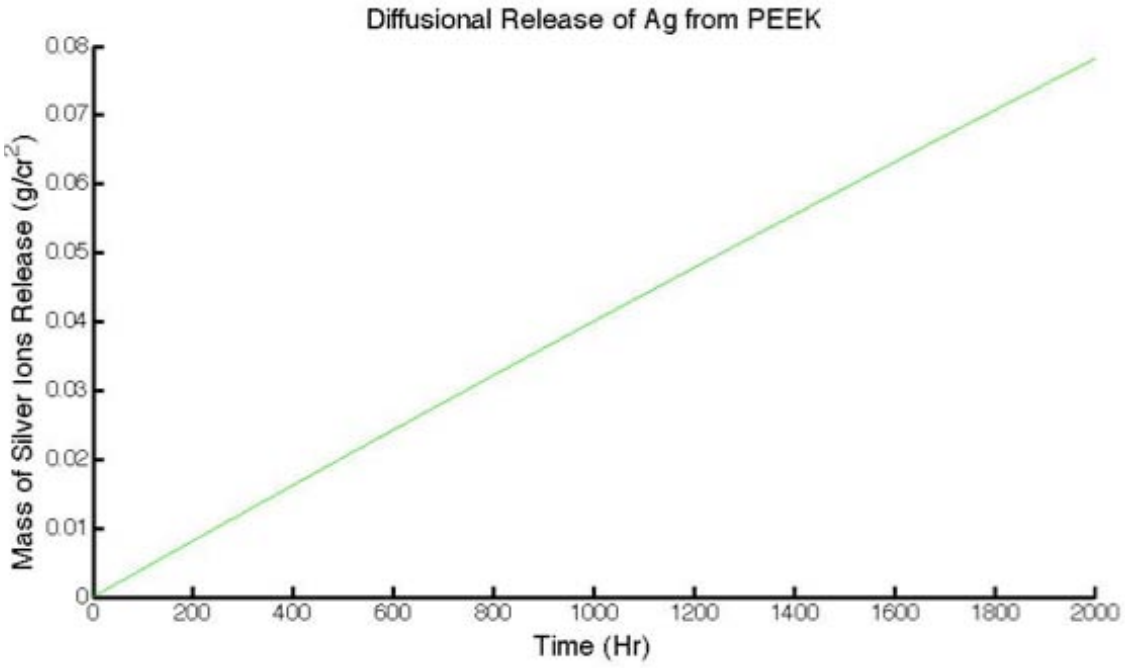

Figure 2-6: Predicted Ag^+ release from PEEK composite by combined Higuchi method with Ag^+ reaction model from Zhang et al. [65, 117].

For PEEK, maximum water uptake has been documented between 0.34-0.44w/w% at 37C [116, 120]. Therefore, the aqueous content was 0.4% of particles suspended in media. To create an idealized model combining the Higuchi method and the Zhang et al. model, the ratios for both O_2 and H^+ were set to be 0.4 of content in solution, which vastly lowered the magnitude of Ag^+ release from the surface of a theoretical composite (Figure 2-7).

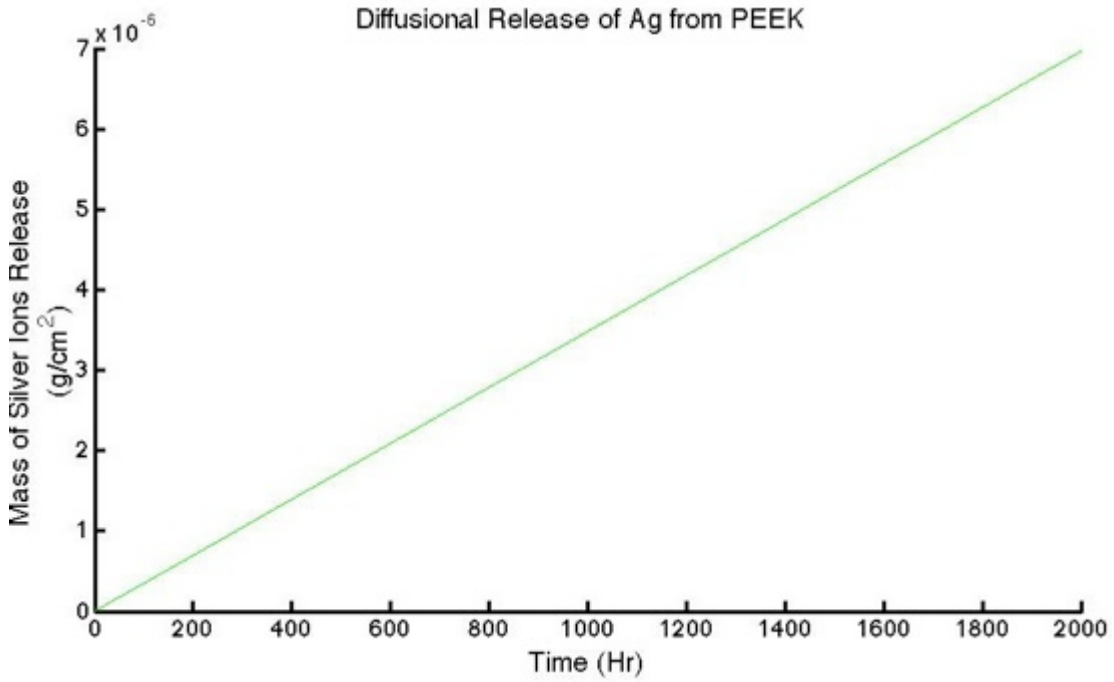

Figure 2-7: Modeled Ag^+ release from PEEK composite by combined Higuchi method with Ag^+ reaction model from Zhang et al. and lowering O_2 and H^+ to 0.4% of values in solution [65, 117].

The next step in developing an idealized model was the inclusion of water diffusion to influence the Ag oxidation reaction. Water uptake by PEEK at time, t, was defined by the M_t/M_∞ ratio (Eq. 7) and was redefined as a factor, x_1. The mass ratio (x_1) was incorporated into the Ag^+ generation portion of the model by directly affecting the levels of O_2 and H^+ (Eq. 9).

$$[Ag^+]_{released} = [Ag]_{initial}\left[1-\exp(-a*t)\right] \quad \text{(Eq. 9)}$$

$$a = \frac{3}{4}\left(\frac{8k_BT}{m_B}\right)^{1/2}\rho^{-1}\exp\left(\frac{-E_a}{k_BT}\right)r^{-1}\left[x_1*O_2\right]^{0.5}\left[x_1*H^+\right]^2$$

At full hydration, the highest concentration of O_2 and H^+ will be present in the matrix, but the maximum water absorption in PEEK is only approximately 0.4%. Thereby, the maximum levels for O_2 and H^+ were reduced to 0.4% of the concentration in PBS (Figure 2-8).

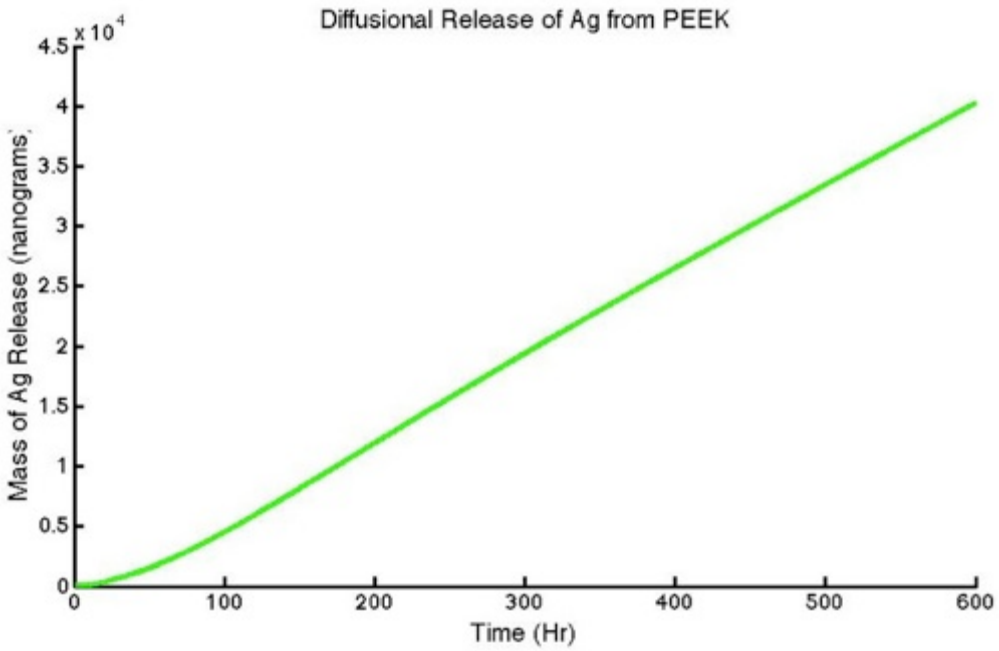

Figure 2-8: Idealized model for release of Ag^+ from PEEK with incorporation of water diffusion.

Again, the magnitude of release declined with the incorporation of water diffusion. Although a linear release was observed over 600 hr, water diffusion created a non-linear region within the first 48 hr of the model, which could correlate to decreased levels of release at the start of incubation.

As elution trials concluded for Ag particles in PBS, the average pH and O_2 were 7.3±0.1 from 9±1 mg/l respectively over the life of the elution trial. Therefore, pH and $[O_2]$ were held constant at 7.2 and 9 mg/l to model idealized release of Ag^+ from a PEEK matrix (Figure 2-9). In summation, the final system

of equations for the Ag-PEEK model was comprised of Ag^+ generation governed by the Zhang et al. model, $[H^+]$ and $[O_2]$ concentrations directly influenced by Fikian Case I water diffusion into PEEK, and, finally, Ag^+ release modeled by the Higuchi method (Eq. 10). The full MATLAB script is detailed in Appendix C2.

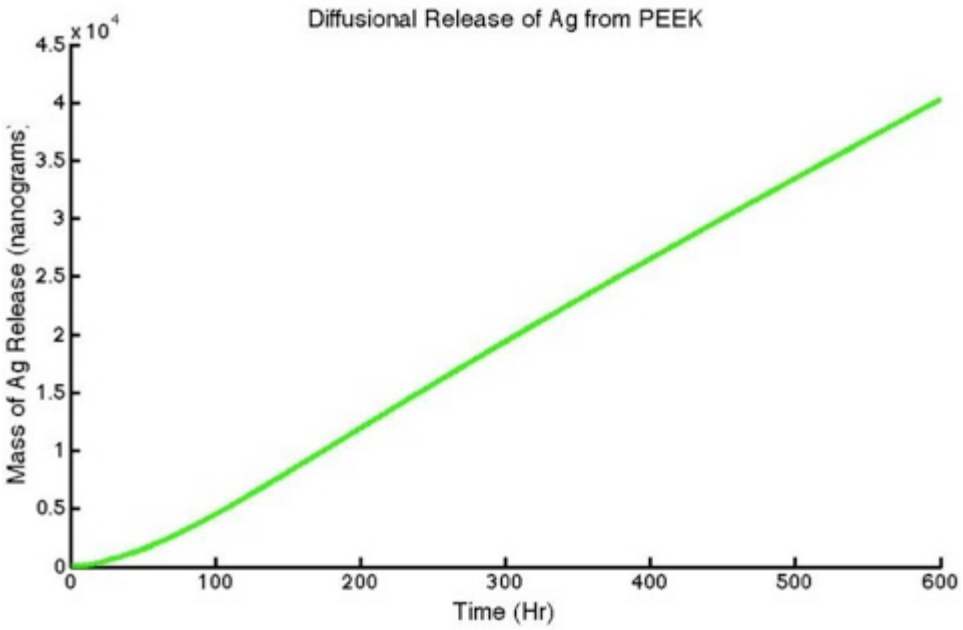

Figure 2-9: Idealized model of Ag^+ release based on O_2 and H^+ levels from PBS.

$$Q_t = \frac{M_t}{A} = \left[D_p t C_p \left(2C - C_p\right)\right]^{1/2} \qquad \text{(Eq. 10)}$$

$$C_P = \left[Ag^+\right]_{release} = C\left[1 - \exp\left(-a * t\right)\right]$$

$$a = \frac{3}{4}\left(\frac{8k_BT}{m_B}\right)^{1/2} \rho^{-1} \exp\left(\frac{-E_a}{k_BT}\right) r^{-1}\left[x_1 * O_2\right]^{0.5}\left[x_1 * H^+\right]^2$$

$$x_1 = \frac{M_t}{M_\infty} = 1 - \sum_{n=0}^{\infty} \frac{8}{\left(2n+1\right)^2 \pi^2} \exp\left(\frac{-D\left(2n+1\right)^2 \pi^2 t}{\ell^2}\right)$$

Thus far, the diffusion coefficient used was for diffusion of water out of PEEK ($4.4x10^{-5}$ cm^2/hr) because the diffusion coefficient of Ag^+ in PEEK in an aqueous environment is unknown. However, diffusion for other molecules in PEEK was measured in previous studies (Table 2-1) [103, 121-123].

Table 2-1: Diffusion coefficient values for various molecules in PEEK.

Substance in PEEK	Diffusion coefficient				Source
	m^2/s	mm^2/hr	cm^2/s	cm^2/hr	
CO2			0.000000002	7.20E-06	De Candia et al. [121]
Water in Brine (desorption)		0.0044		4.40E-05	Boinard et al. [103]
Water in Brine (adsorption)		0.0033		3.30E-05	
Benzene	8.2E-13			2.95E-05	Wolf et al. [122]
Tolune	3.5E-13			1.26E-05	
Chloroform	9.85E-12			3.55E-04	
Carbon Disulfide	3.7E-12			1.33E-04	
Antibiotic Diffusion out of PMMA			8.1E-11	2.92E-07	Law et al. [123]
			1.69E-10	6.08E-07	
			1.7E-11	6.12E-08	

The majority of diffusion coefficients were either associated with strong organic solvents or gas diffusion in air environments, but nonetheless, a relevant range of magnitudes for PEEK material were defined. When the Diffusion coefficient values were incrementally increased from $2x10^{-6}$ to $2x10^{-4}$ cm^2/hr (Figure 2-10), the predicted Ag^+ release increased with diffusion coefficient, but the magnitude of change decreased as coefficient values elevated toward the upper limits of relevant values (Table 2-1). Due to the influence of the diffusion coefficient on the model, a diffusion coefficient of $4.4x10^{-5}$ cm^2/hr, coinciding with water desorption from PEEK, was used as a conservative estimation of Ag^+ release for further idealized model predictions.

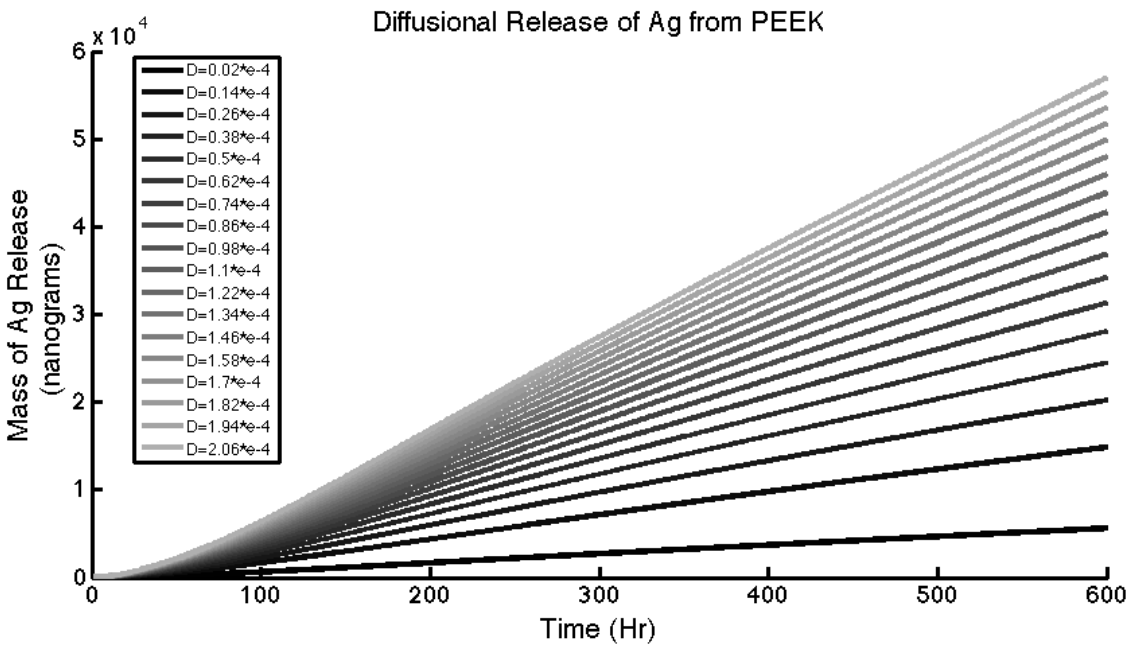

Figure 2-10: Predicted Ag^+ release when diffusion coefficient is varied from 0.000002 to 0.000206 cm^2/hr at 0.000012 cm^2/hr increments.

Ion Release Trials and Model Fitting

Based on the results from the previous section, both the nano (nanoAg) and micro-sized porous (μAg) Ag particles displayed antibacterial properties. To characterize the Ag^+ generation kinetics, both particles types were incubated in PBS for 15 days. The Ag^+ release kinetics were similar to profiles measured for nano-diameter Ag particles by Zhang et al. and Liu and Hurt (Figure 2-11) [65, 70]. Concentration of Ag^+ rose almost linearly within the first 48hr before release began to decline and plateau between 100-200 μg/l by 250 hr. Both Ag particle types followed similar release patterns; however, the nanoAg showed higher

levels of Ag^+ production.

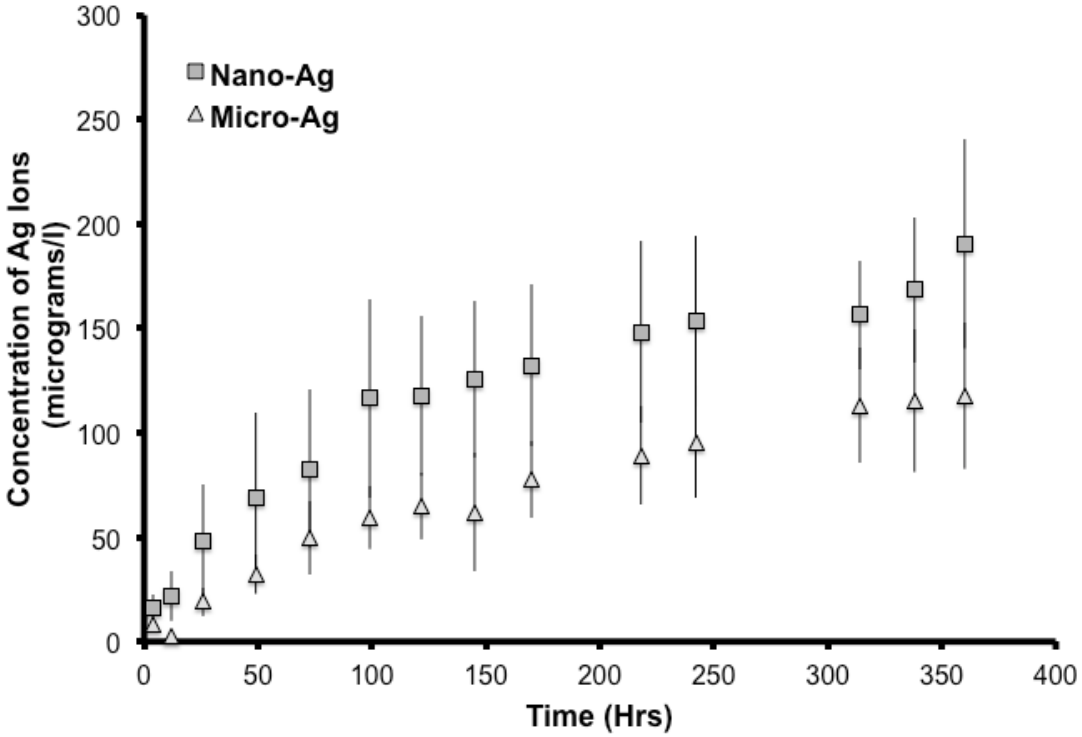

Figure 2-11: The Ag^+ release profiles for both nanoAg and micro-sized porous Ag particles (μAg).

In the model proposed in Eq. 6, one variable, E_a, was unknown. Previously, the model was using the calculated value of E_a from the Zhang et al. study; however, E_a could be substantially different for the nanoAg and μAg studied. Therefore, Eq. 6 was fitted to the particle elution data for each particle type to determine an optimized value for E_a. All fitting was performed with the Curve Fitting Tool in MATLAB (MATLAB R2011a, MathWorks, Inc.). When the initial concentration, $[Ag]_{initial}$ was held constant along with pH (7.3) and O_2 concentration (9 mg/l), a more linear fit was generated for both nanoAg and μAg particles with adjusted R^2 values of 0.64 and 0.89 respectively (Figure 2-12). E_a (E_{a1}) values for nanoAg and μAg were $-6.5x10^{-20}$J and $-6.3x10^{-20}$J respectively.

This value is lower than the original value in Zhang et al. studies [65].

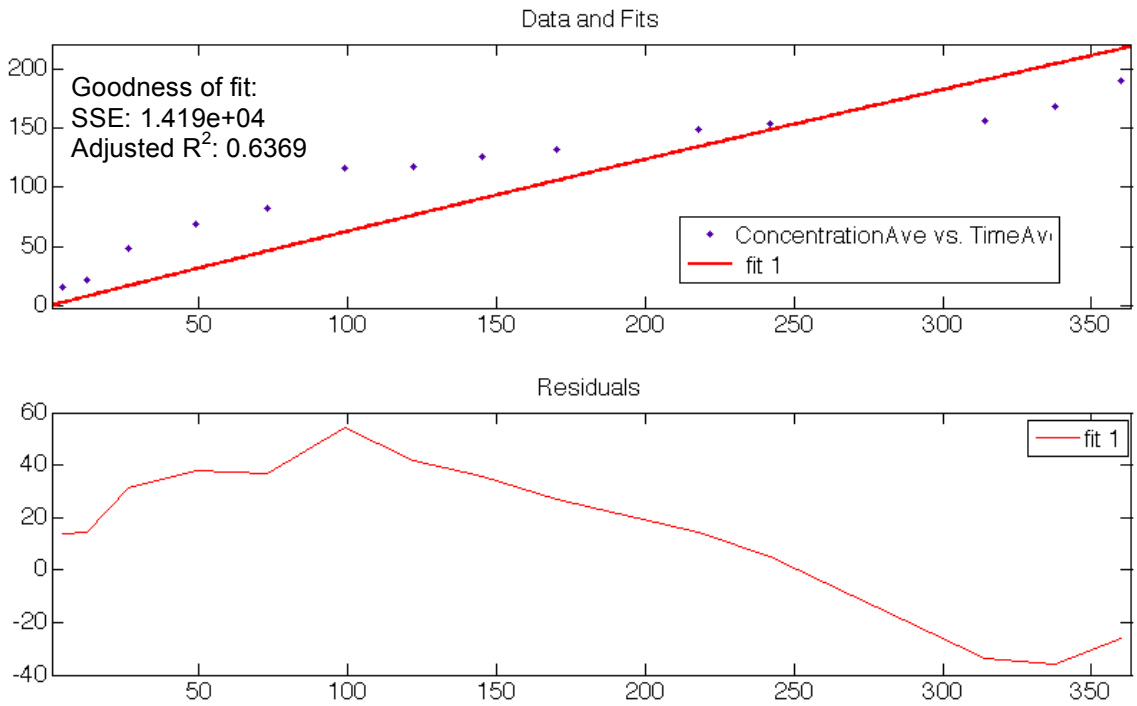

Figure 2-12: Model fit for nanoAg ion release when $[Ag]_{initial}$ is held constant.

The model was then fit for both $[Ag]_{initial}$ and E_a values. Adjusting the model for $[Ag]_{initial}$ enhanced the model fit, which was also observed by Zhang et al. The initial concentration can be reduced due to particles aggregating in solution which can be intensified by NaCl [65, 70]. Additionally, $[Ag]_{initial}$ may be inaccurate to the model because small Ag particles do not completely dissolve in solution from oxidation within the time period of the study [65, 70]. After fitting for both $[Ag]_{initial}$ and E_a, the values for E_a (E_{a2}) decreased to -7.9 x10-^{20}J for nanoAg and -7.6 x10-^{20}J for µAg with adjusted R^2 values of 0.97 and 0.99 respectively (Figure 2-13 & 2-14). The estimated values for $[Ag]_{initial}$ were lower than the initial concentration at 176.1 µg/l for nanoAg and 140.4 µg/l for µAg. Adding one

extra parameter, $[Ag]_{initial}$, improved the capacity of the model to fit the experimental data. Expanded information on all fits for the particle elution trials was included in Appendix D.

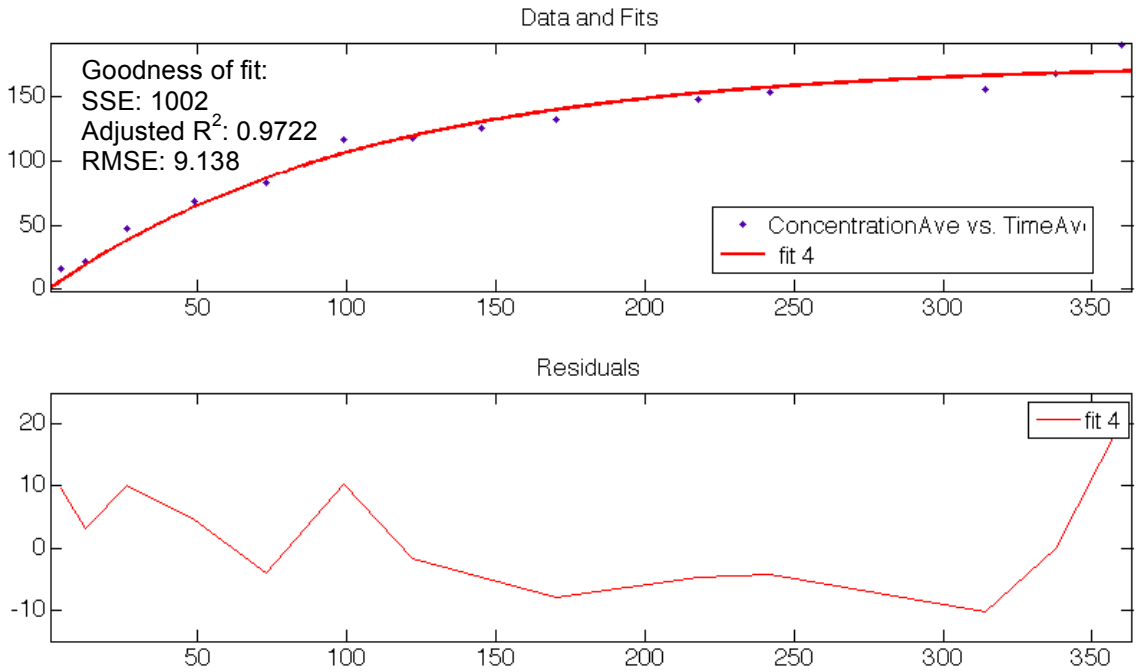

Figure 2-13: Model fit and residuals for nanoAg when both E_a and $[Ag]_{initial}$ were predicted.

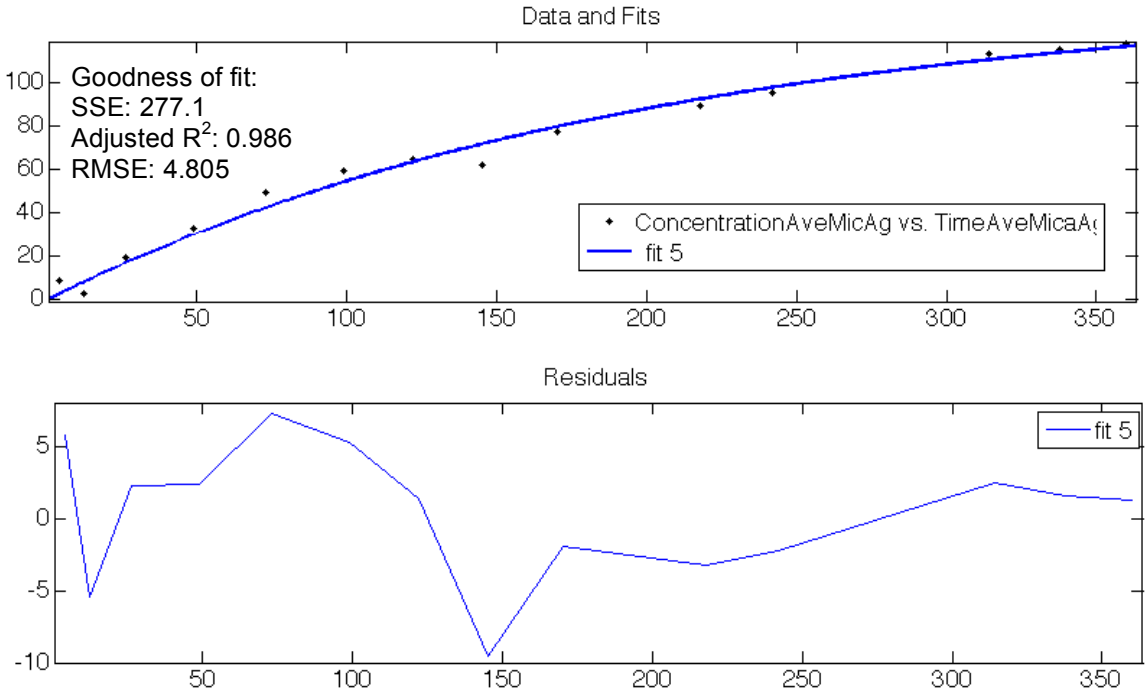

Figure 2-14: Model fit and residuals for μAg when both E_a and $[Ag]_{initial}$ were predicted.

When fitted values for E_a were incorporated into the entire model for Ag^+ elution from Ag-PEEK composites, overall predicted Ag^+ release increased from the E_a calculated from Zhang et al. ($-5.5x10^{-20}$J) to E_{a2} ($-7.9x10^{-20}$J) (Figure 2-15). Due to the positive influence on Ag^+ release and the better fit to experimental data (R^2>0.97), further development of the model to predict potential Ag^+ release from Ag-PEEK composites was focused on the estimated values for E_{a2}.

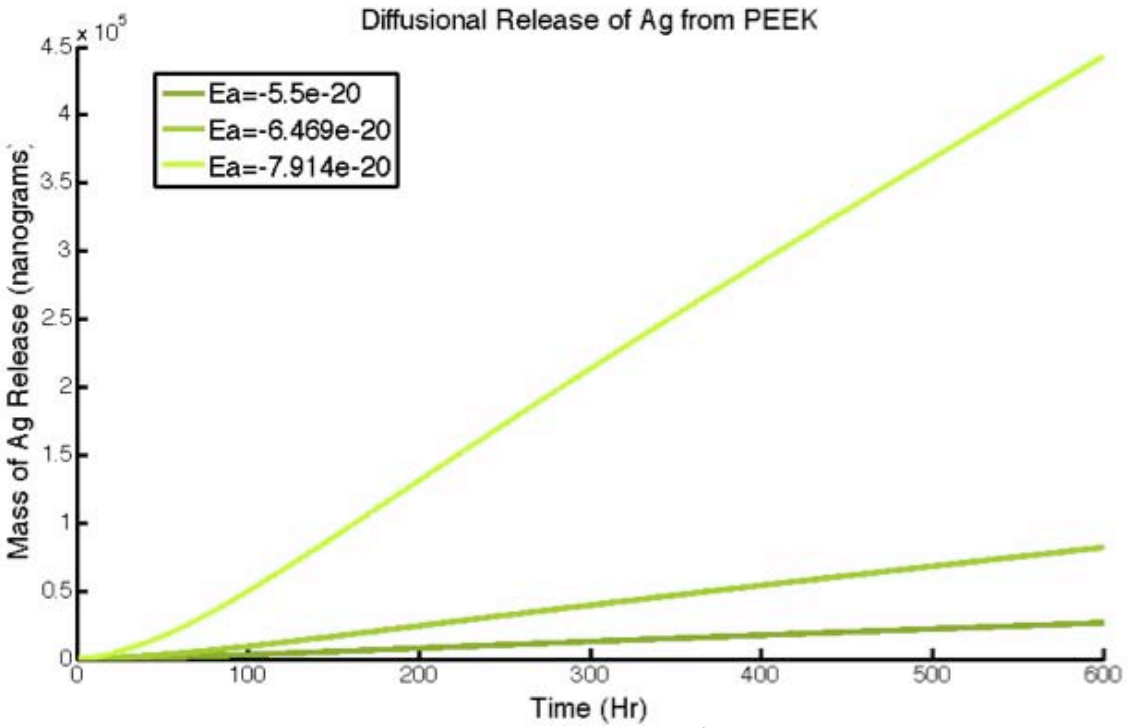

Figure 2-15: Model predictions on the influence of E_a on Ag^+ elution from Ag-PEEK. As E_a was decreased from the Zhang et al. (-5.5e-20J) value to the predicted value in this study (-7.9e-20J), Ag^+ release increased [65].

Theoretical Release from Ag-PEEK Composite

There were a few limitations to this model in the current form. First, a significant parameter for the Zhang et al. model (Eq. 9) was the radius of the particle (r) because the model was developed to predict Ag oxidation in Ag nanoparticles of varying diameters, ranging from 20 to 80nm [65]. The same radius value was used for both nanoAg and μAg for all iterations of this model since the diameter of the μAg particle does not exactly characterize the antimicrobial potential of the porous structure. The increased antimicrobial properties of smaller Ag particles stem from the increased surface area to mass

ratio, which was supported by the antibacterial testing conducted with agar gels. Since the specific surface area was equivalent for nanoAg and μAg, using the same value for the radius was justified. Furthermore, the diffusion coefficient for Ag^+ out of PEEK is unknown, so the value for water diffusion from PEEK was chosen for later iterations of the idealized model. The water diffusion coefficient was a conservative estimate within relevant values for PEEK [103, 121-123].

The fundamental purpose of this model was to predict Ag^+ release in aqueous media from a rigid polymer molded with Ag particulate. The model was idealized for Ag^+ generation from two Ag particulates. The next influential factor to Ag^+ elution was composite loading; so, to study this effect, initial concentration of Ag in the matrix was increased from 1 to 10 w/w% for both Ag particulates. Within 48hr, the nanoAg model predicted approximately 1600 and $1.6x10^4$ ng of Ag^+ released for 1 and 10w/w% respectively and a sustained release beyond 600 hr (Figure 2-16A). μAg model predicted slightly lower ranges of release (1200 to $1.2x10^4$ ng) for ranges of 1 to 10 w/w% loadings (Figure 2-17A). The release pattern at shorter time periods up to 48 hr was non-linear due to the slow water uptake portion of the model; however, when expanded beyond 600 hr, the model exhibited first order release. Release profiles with other E_a values were included in Appendix E

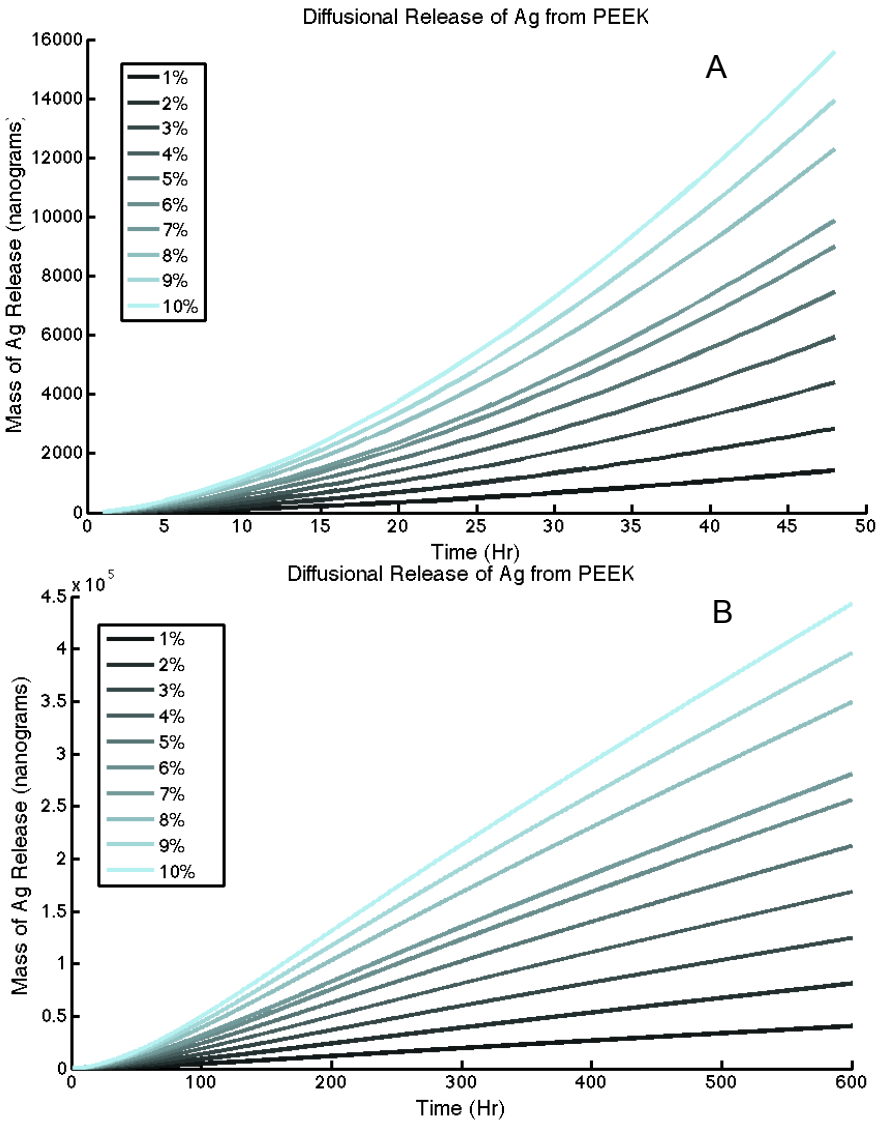

Figure 2-16: Diffusional release profiles for nanoAg composite material at 50hr (A) and 600hr (B).

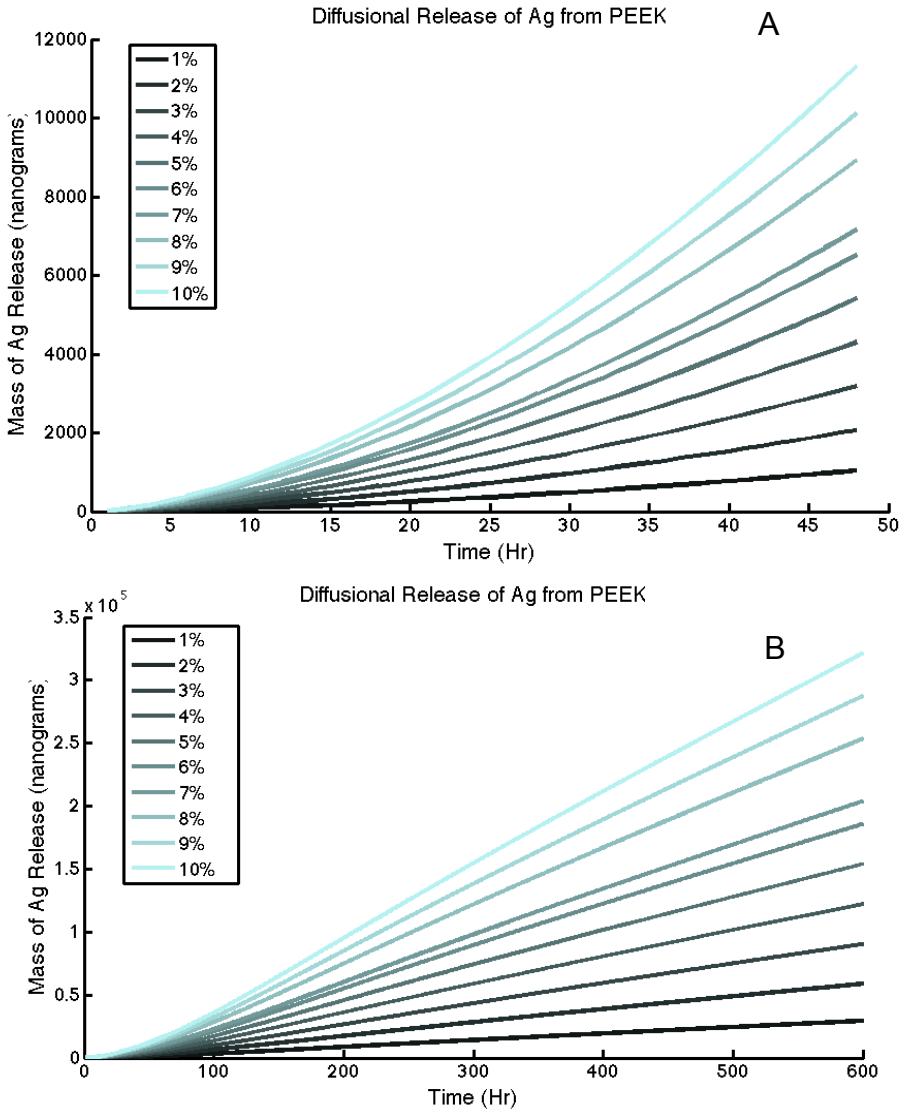

Figure 2-17: Diffusional release profiles for μAg composite material at 50hr (A) and 600hr (B).

The model was designed to be equivalent to future elution trials performed in approximately 3 ml of aqueous media with Ag-PEEK composites and also comparative to future bacterial attachment experiments performed in TSB. Multiple studies have reported inhibitory concentrations for Ag and Ag^+ against bacteria. Jung et al. measured, in depth, the minimum inhibitory concentration (MIC) of Ag^+ and utilized procedures similar to existing protocol designs in our

labs for bacterial adhesion. The reported MIC for both *E. coli ATCC 25922* and *S. aureus ATCC 25923* at bacterial concentrations of 10^{5-6} cfu/ml was approximately 50 ppb (50 µg/l) [44]. The equivalent release in our test configurations was 150 ng of Ag within the first 48 hr of incubation. With all values of E_a predicted by the model, at minimum, 150 ng of Ag^+ was eluted within 48 hr, and, in most cases, release was an order magnitude higher. The MIC is the value needed to inhibit all bacteria in the media. Most of the proposed studies for Ag-PEEK composites are for bacterial adhesion on surfaces and may have colony numbers even lower than planktonic bacteria concentrations.

The developed model predicted loading ratios from 2-10 w/w% Ag in a PEEK matrix produce sufficient levels of Ag^+ to inhibit surface bacterial growth. The model predictions matched results of previous tests using different designs for antimicrobial composites previously used in medical applications. Previous work with our implant retrieval program revealed that antibiotic bone cement spacer loads were as high as 8.7 to 12% to combat infection [24]. In addition, in previously published studies, polyamide was loaded with 2, 4, and 8 w/w% of Ag to successful reduce *S. aureus* and *E. coli* growth [36, 124-126]. Since PEEK is denser and less porous than other biomaterial polymers used with Ag previously, higher amounts of Ag in the bulk might be required to achieve the desired antimicrobial effects [76, 126]. For future studies into antimicrobial PEEK composites, loading ratios of 2%, 5%, and 10 w/w% are suggested.

Conclusion

Antibacterial testing in Agar gels revealed a size dependent effect as the smallest particle size (100 nm) exhibited the most reduction in bacterial growth. Bacterial inhibition with a porous micro-sized particle (μAg) of a similar surface area to mass ratio as the 100 nm particles (5 m^2/g) suggested that antimicrobial properties were linked to smaller particles having increased surface area available for oxidation of Ag^0 to Ag^+. Using the properties and Ag^+ release kinetics of the 100 nm or μAg, a model for Ag incorporation into a PEEK was developed to estimate the magnitude of Ag^+ release. The idealized model predicted Ag^+ release at levels above MIC for *E. coli* and *S. aureus* when PEEK matrices were incorporated with ≥1% of Ag particles.

3. Fabrication and Analysis of Ag-PEEK Biomaterials

Abstract

Periprosthetic infection is an infrequent yet devastating and sometimes life-threatening complication of medical device implantation and is associated with increased cost, length of hospitalization, and multiple surgical interventions. All biomaterials are prone to device-associated infection. Since the early 1990s, devices comprised of polyetheretherketone (PEEK) have increasingly been used in the spine and orthopaedic device industries, and thus their protection from infection becomes a high priority. Because Ag particulates have well-established antimicrobial properties and thermal stability, we examined the feasibility of creating Ag-PEEK composites with nanoAg, μAg, and Ag phosphate (Zr2K) particulates for infection control. The PEEK matrix was loaded with three filler ratios (targets of 2, 5 and 10 w/w%) of Ag particulate; however particle aggregation occurred and lower than expected weight ratios were obtained. In Ag elution trials, nanoAg and μAg-PEEK composites sustained linear and long-term release of Ag at inhibitory concentrations for *S. aureus* and *E. coli*. In contrast, Zr2k composites released Ag rapidly within the first 48 hr, however, release decreased quickly to levels inadequate for inhibition of bacterial growth beyond 96 hours. Incubation of 0.6% and 3.6% Ag-loaded matrices (target ranges of 2 and 5%) with *S. aureus* or with *E. coli* showed no reduction in surface adherent bacteria as measured by direct counting. When filler ratios were increased,

significant reductions in bacterial counts occurred in approximately 5 out of 12 trials for each filler type. Our data suggest that with process optimization, the Ag content of PEEK can be tuned to achieve long-term, bactericidal levels of Ag^+ release.

Introduction

The implantation of orthopaedic devices is a very successful surgical procedure and has allowed continued mobility and function for millions of patients [1, 80]. A devastating and sometimes life-threatening complication of these surgeries is infection, which can establish on the implant surface. Infection is relatively infrequent, e.g., 1 to 2% of all primary arthroplasty procedures, up to 5% of fracture fixation devices [4, 9, 10], up to 30% of external fixators [11, 12], and up to 6.7% of spinal fusions have been reported to become infected [2, 3, 5]. These infections are associated with an increased medical cost 4.8 times higher than primary surgery [1], and in the case of spinal fusions, can lead to bone destruction and eventual destabilization of the implant and the entire spinal segment [13]. These implant-associated infections are difficult to eradicate due to immune surveillance of the implant, difficulty in maintaining therapeutic levels of antibiotics around the relatively avascular implant, and most importantly, due to the metabolic changes associated with bacterial colonization of surfaces that render the adherent bacteria recalcitrant to antimicrobial treatment [1-5].

To minimize the occurrence and devastating consequences of periprosthetic infection, many research efforts have focused on the development of materials that resist bacterial colonization. Controlled release systems as well as systems that permanently display antimicrobials have been applied to implantable medical devices in attempts to reduce local infection [14, 26, 28, 34, 127, 128]. Ag has emerged as a popular choice because of low cellular toxicity [36] and a wide range of activity against Gram-negative and Gram-positive bacteria, as well as fungi. Antimicrobial properties of Ag are thought to be due to interaction of the Ag^+ with sulfur, oxygen, and nitrogen functional groups within the bacterium [36, 129, 130]. Frequently, Ag^+ interacts with thiol groups (-SH) on structural proteins and key respiratory enzymes in bacteria, and, in turn, inactivate them [129]. This inactivation leads to structural damage in cell walls, reduction in cell metabolism, loss of the ability to regulate exposure to oxidative reactions, and ultimately loss of bacterial viability [36, 129]. Ag^+ also causes bacterial DNA to condense and inhibit DNA replication [130]. Because of these multiple mechanisms, the risk of developing bacterial resistance to Ag through single point mutations is reduced [36, 62, 130].

Ag particles have recently been incorporated into dental implants and burn wound dressings [44], but its most widespread use to date has been as an antimicrobial coating in catheters [45, 46]. Ag has been added directly to molten polymers for incorporation into various polyurethane and silicone catheters [29, 45, 46]. Such bulk loading removes the risks of scratching or more catastrophic mechanically-based losses, the risk of low surface adhesion, or the equally

important risk of uncontrolled release of Ag^+ from the surface coating. Impregnated polymers also have the potential for long-term release by diffusion from the bulk.

Poly(aryletheretherketone) or PEEK is one such moldable polymer that is commonly used for orthopaedic and other load-bearing applications. PEEK is a two-phase semi-crystalline polymer whose average tensile strength and flexural modulus are 93 MPa and 4 GPa respectively. A PEEK composite of up to 30% (w/w) carbon fiber reinforcement (CFR) has increased the average tensile strength and flexural modulus to 170 MPa and 20 GPa respectively [82]. PEEK has also been reinforced or enhanced with compounds like glass and hydroxyapatite (HA) to increase bone on-growth potential *in vivo* [81, 82]. Because of the strength, versatility, and appropriate mechanical properties of PEEK, more traditional metal devices are increasingly being replaced by PEEK in applications ranging from spinal cages to intramedullary nails and finger joints [80]. With this active increase in the share of the medical device industry, comes a growing need for PEEK surfaces and materials that will actively prevent bacteria adhesion and infection. In this report, we have (1) asked if different-sized Ag particulates could be uniformly incorporated into a PEEK matrix, (2) if these particles would influence the material properties of molded PEEK, (3) if Ag^+ will actively elute from the composite surface, and (4) if the effects of the surface and the eluents will reduce bacterial adhesion and growth.

Materials and Methods

Materials

Due to their high temperature resistance (>700°C) and bactericidal properties against both *S. aureus* and *E. coli* in agar gels at concentrations less than 0.2 µg/ml (Chapter 2), three Ag particulates were chosen: a Ag nanoparticle (<100 nm diameter, 99.5% trace metals basis, specific surface area: 5 m^2/g, Sigma Aldrich), a porous micro-sized Ag particle (~7.5 µm diameter, specific surface area: 5 m^2/g, Biogate HyMedic 4000, DE), and a 10% Ag-composite particle (1.3 µm diameter, Ag sodium hydrogen zirconium phosphate, Zr2k, Miliken, USA) (Table 3-1). Ag-PEEK composites (nanoAg, µAg, or Zr2K) were fabricated by mixing a pellet grade of unfilled PEEK (LT1, Invibio, UK) with powder forms of each Ag particulate at weight ratios of 2, 5, and 10%, respectively. Unfilled PEEK (control) or the PEEK/Ag particulate mixtures were then composited in an industrial grade twin-screw extruder, pelletized and subsequently injection molded into bars under industrially recommended settings as described previously [99, 131]. For each concentration of Ag filler, both injection molded surfaces and machined surfaces (where the exposed surface is, at minimum, 500 µm below an injection molded or extruded surface) were tested. Due to equipment limitations, composites at filler ratios of 2 and 5% were fabricated in a separate mold than the 10% composites. Therefore, samples were compared to unfilled injection molded PEEK from the respective molds.

Table 3-1: Description of Ag particulates used as additives in PEEK.

Material	Ag Type	Particle Size	Radius (m)	Density (g/cm^3)	Surface Area (m^2/g)
NanoAg	Pure Ag	80-100 nm	0.00000005	10.49	5
BioGate HyMedic 4000 (μAg)	Porous Ag particle	7.5 μm	0.00000375	10.49	3-5.0
Milliken Zr2k	10% w/w Ag Loaded sodium hydrogen zirconium phosphate Particle	1.3 μm	0.0000013	0.25	7.69

Material Characterization

After manufacturing, crystallinity was evaluated for any differences in melt processing that influence crystal formation. Crystallinity was calculated for each composite using specular reflectance FTIR spectroscopy measurements at 3 points across each sample (n=5) described previously (Chapter 1) and in accordance with ASTM F2778 [99, 100]. Ag dispersion was observed through light microscopy imaging (Leica DFC490) and scanning electron microscopy (SEM, FEI, model XL30) at magnifications from 50 to 2000x; particles were confirmed as Ag through elemental analysis with Energy Dispersive X-ray Spectroscopy (EDS, FEI, XL30).

Ag dispersion was also characterized with MicroCT (Scanco μCT 80, Switzerland), with scanning at a 10-μm uniform voxel resolution. Images were analyzed for large conglomerates of Ag particles or areas void of Ag. Material density was assessed by gravimetric analysis and volume measurements from a gas pycnometer (Accupyc II 1340). Results were compared to theoretical density calculations for the composite materials using the linear rules of mixtures (Eq11 [132, 133]).

$$\rho_c = \frac{\rho_f \rho_p}{\rho_p m_f + \rho_f (1 - m_f)} \quad \text{Eq11}$$

Where ρ_c is the density of the composite material, ρ_f is the density of the filler material, ρ_p is the density of the polymer, and m_f is the mass fraction of the filler. Solving for the mass faction yields (Eq12).

$$m_f = \frac{\rho_f \rho_p - \rho_c \rho_f}{\rho_c \rho_p - \rho_c \rho_f} \quad \text{Eq12}$$

Mechanical Behavior

In order to understand the impact of Ag additives to mechanical behavior of PEEK, composites were subject to small punch testing. Specimens of each composite type and filler ratio (n=5) were confined in a die and guide fixture and then subjected to bending by indentation with a custom-built, hemispherical headed punch as described previously in Chapter 1 [94-96]. To prepare specimens for small punch testing, 2mm thick rectangular specimens (10 x 12 mm) were sectioned to 1 mm thick slices by a diamond saw (Buehler IsoMet 100). Subsequently, slices were lathed with a precision diamond tool to 0.5 mm thick and then cut to a disc 6.5 mm in diameter with a metal hole-punch. Load and displacement were recorded at a constant displacement rate of 0.5 mm/min. Load displacement curves were characterized by the peak load, ultimate load, ultimate displacement, and work to failure. After failure of the specimens, fracture

surfaces were analyzed using light microscopy as well as scanning electron microscopy (SEM) where appropriate.

Surface Colonization of Bacteria

To evaluate effects of the composite material on bacterial colonization, 6 samples of each composite and 6 samples of unfilled PEEK were sectioned (10 x 12 x2 mm) and cleaned by immersion in a 1% Alconox® solution overnight, followed by extensive washing in distilled, deionized (DI) H_2O. Prior to testing, samples were sterilized by submersion in 70% EtOH for 15 min. *S. aureus* (ATCC® 25923™) were cultured in BBL™ Trypticase™ Soy Broth (TSB, BD Biosciences); 250 rpm, 37ºC, 16-18 hr. This culture was diluted to 10^4 colony forming units per milliliter (cfu/ml) using a 0.5X McFarland (a turbidity standard equivalent to 10^7–10^8 cfu of *S. aureus* (PML Microbiologicals, Wilsonville, OR). 10^4 cfu (1ml) were incubated with samples for 3, 6, 24 or 48 hr at 37ºC without agitation. The 48hr time period had the media changed at 24 hr. At each time interval, 6 samples were removed and washed; 4 samples were used to determine bacterial colonization, and 2 fixed for imaging. Each test was repeated a minimum of 3 times (experiments were continued until repeatable results were observed as compared to controls).

To determine number of adherent bacteria, samples were washed 3x in PBS to remove non-adherent cells. Adherent bacteria were then suspended by sonication (Bransonic 1510, Emerson Electric Co., US, 40kHz) in 1 ml 0.3% Tween-80 in PBS for 5 min, followed by vortexing as described by Barth et al.

[134]. Viable bacteria were serially diluted, plated on 3M PetriFilms, incubated, 24 hr, 37ºC, colonies counted (countable range = 25 – 1200 cfu/film), and numbers expressed as relative to the average cfu recovered from the controls.

To visually observe bacteria surface colonization, two samples from each time point were assessed using SEM. After washing 5x in PBS, samples were fixed with 4% paraformaldehyde for 10 min, dehydrated in an ethanol series, and carbon sputter-coated to reduce charging during SEM imaging.

After testing in TSB, 24hr trials were repeated in brain heart infusion media (BHI), a NaCl rich (~1%), media, to test that differences in bacterial growth were not due to media selection. Bacterial challenges were also repeated with the Gram-negative *E. Coli* (ATCC® 25922™) for 6hr and 24hr challenges. A final set of challenges for 24 hr were performed on composite samples after being hydrated at 60ºC for 3 days to observe if hydration impacts the Ag antimicrobial properties.

Biocidal Activity

To evaluate the biocidal activity of the composite materials, a method was modified from the Japanese industrial Standard, JIS Z 2801, and the International standard for measuring antimicrobial activity on plastic surfaces (ISO 22196) [115, 135]. *S. Aureus* (ATCC® 25923™) was cultivated for 18 hr in a slant culture of Nutrient Broth No. 3 agar (NB, 70149 Fluka, CH), selected colonies were suspended in a 1/50 dilution of NB and by direct counting using a hemocytometer, brought to a concentration of $5x10^5$ cfu/ml. Surfaces (10 x10

mm) of both control and composite materials were then spotted with a 50µl aliquot (=2.5 x 10^4 cfu), followed by placement of a sterilized PEEK film (thickness ~0.076mm) over the aliquot (Figure 3-1). Samples were then incubated in a humid environment for 24 hr at 37ºC. The diluted inoculant maintains bacterial viability without proliferation and increased colony growth [115, 126, 135]. After 24 hr, bacteria were recovered and quantified in a similar procedure to bacterial adhesion testing.

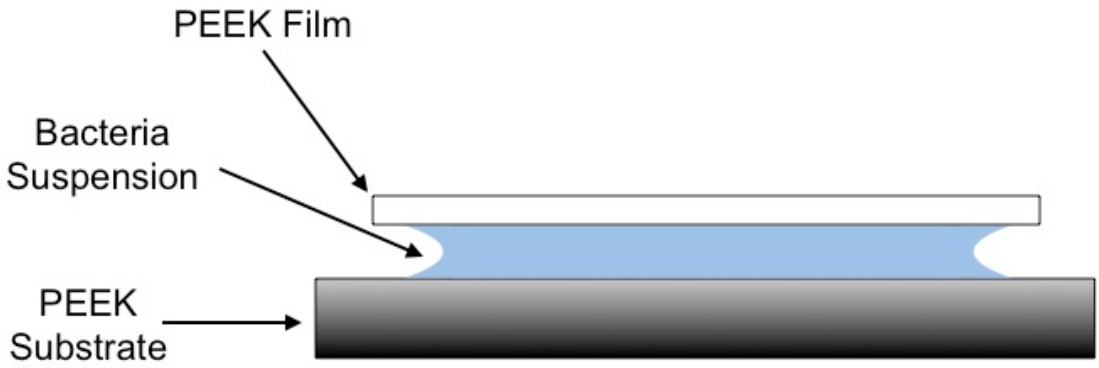

Figure 3-1: The biocidal activity experiment (ISO 22196) consisted of the tested PEEK substrate, a 50 µl bacterial cell suspension, and a thin PEEK film (~0.076mm) cover slip.

Ag Elution

To study Ag^+ release from Ag-PEEK composites, bars (30 x 10 x 2mm, n=4) of unfilled PEEK and the different 10% Ag-PEEK composites were incubated in 3ml PBS or DI H_2O for 26 days. Approximately every 48 hr, fluid was exchanged and stored at 4ºC for analysis. Ag^+ concentrations were calculated by atomic absorption spectrometry (model AA240-FS, Varian Techtron Pty Ltd., AU). Concentrations were determined from absorbance values by

comparison to a standard dilution curve created from known Ag^+ concentrations (0.05 ppm to 10 ppm).

Theoretical Model Comparison and Fitting

To compare and develop a robust model to predict Ag^+ elution from an Ag-PEEK composite, the model developed in Chapter 2 was compared to elution data collected from Ag-PEEK composites in the previous section. Diffusion coefficient, D, was fitted to experimental data using the Matlab "Curve Fitting Tool" (MATLAB R2011a, MathWorks, Inc.). Using the custom equation option, a non-linear least squares regression was performed with a trust-region algorithm. The fit was evaluated by the sum of squares due to error (SSE) and adjusted R^2 statistics.

Statistics

Distributions were inspected for normality using the Shapiro-Wilk test. For comparisons with normal data sets, T-Tests or ANOVA with a post-hoc Tukey was used. For comparisons with non-normal data sets, the Mann-Whitney U test or Kruskal-Wallis 1-way ANOVA was utilized, where appropriate. A p-value of less than 0.05 was used to determine significance for all tests. For all statistical tests, PASW Statistics (Version 19.0.0; IBM, Chicago, IL) was used.

Results

Material Characterization

PEEK composite density increased with filler ratios, however; densities were not at the levels dictated by theoretical calculations (Table 3-2). Following the linear rule of mixtures (Eq11), in all cases, the composite density did not reach the targeted theoretical density, and in certain cases, as with the 10% nanoAg the actual mass ratio was 50% lower than targeted. The targeted amounts will be used throughout, however, to refer to the different composites

Table 3-2: Measured and theoretical density for Ag-PEEK materials.

Additive	Target Filler Mass Ratio	Actual Mass Ratio	Measured Density (g/cm^3)	Theoretical Density (g/cm^3)
NanoAg	2%	0.3 ± 0.2%	1.30	1.32
	5%	2.9 ± 0.4%	1.33	1.36
	10%	4.7 ± 0.4%	1.34	1.42
Micro Porous Ag (µAg)	2%	0.6 ± 0.4%	1.31	1.32
	5%	3.6 ± 0.5%	1.34	1.36
	10%	8.3 ± 0.7%	1.39	1.42
SelectSilver® Zr2k	2%	0.2 ± 0.1%	1.30	1.21
	5%	-0.2 ± 0.1%	1.33	1.08
	10%	-0.5 ± 0.0%	1.36	0.93

Independent of filler ratio, crystallinity of nanoAg or µAg composites was not significantly different from unfilled controls ($p \geq 0.07$) (Table 3-3). Due to different molding conditions, the 2-5%.nanoAg and µAg were at slightly lower crystallinity levels (22-25%) than their 10% counterparts (30-33%); all fall within standard ranges for crystallinity for injection molded PEEK [77, 99]. In contrast, crystallinity of Zr2k composites was significantly different from controls at 2-5% loadings (31-32%, $p \leq 0.02$) and when filler was increased to 10% (47%, $p < 0.00$).

Table 3-3: Crystallinity of unfilled PEEK and Ag-PEEK materials.

Material	Crystallinity (%) (mean ± SD)
Unfilled PEEK (2-5% Mold)	*24.9 ± 2.3*
2% nanoAg	*22.4 ± 5.5*
5% nanoAg	*21.8 ± 1.8*
2% µAg	*23.3 ± 3.4*
5% µAg	*25.0 ± 1.3*
2% Zr2k	*32.1 ± 2.2*
5% Zr2k	*31.4 ± 1.3*
LT1 (10% Mold)	*28.1 ± 1.0*
10% nanoAg	*33.3 ± 3.3*
10% µAg	*30.3 ± 3.4*
10% Zr2k	*46.5 ± 3.7*

As composites approached 10% filler loading, Ag deposits could be observed visually (Figure 3-2a). Using SEM, agglomerations of Ag particles that were > 50µm on injection-molded surfaces and > 100µm on machined surfaces were apparent (Figure 3-2b). Based on evaluation by EDS, these large metallic deposits were identified as elemental Ag. Using MicroCT analysis, metallic agglomeration was also apparent throughout the bulk of the polymer composites through high contrast areas and beam hardening zones (Figure 3-2c). These effects were noted to a lesser extent in the Zr2k material where the filler particles were themselves 10% Ag (w/w).

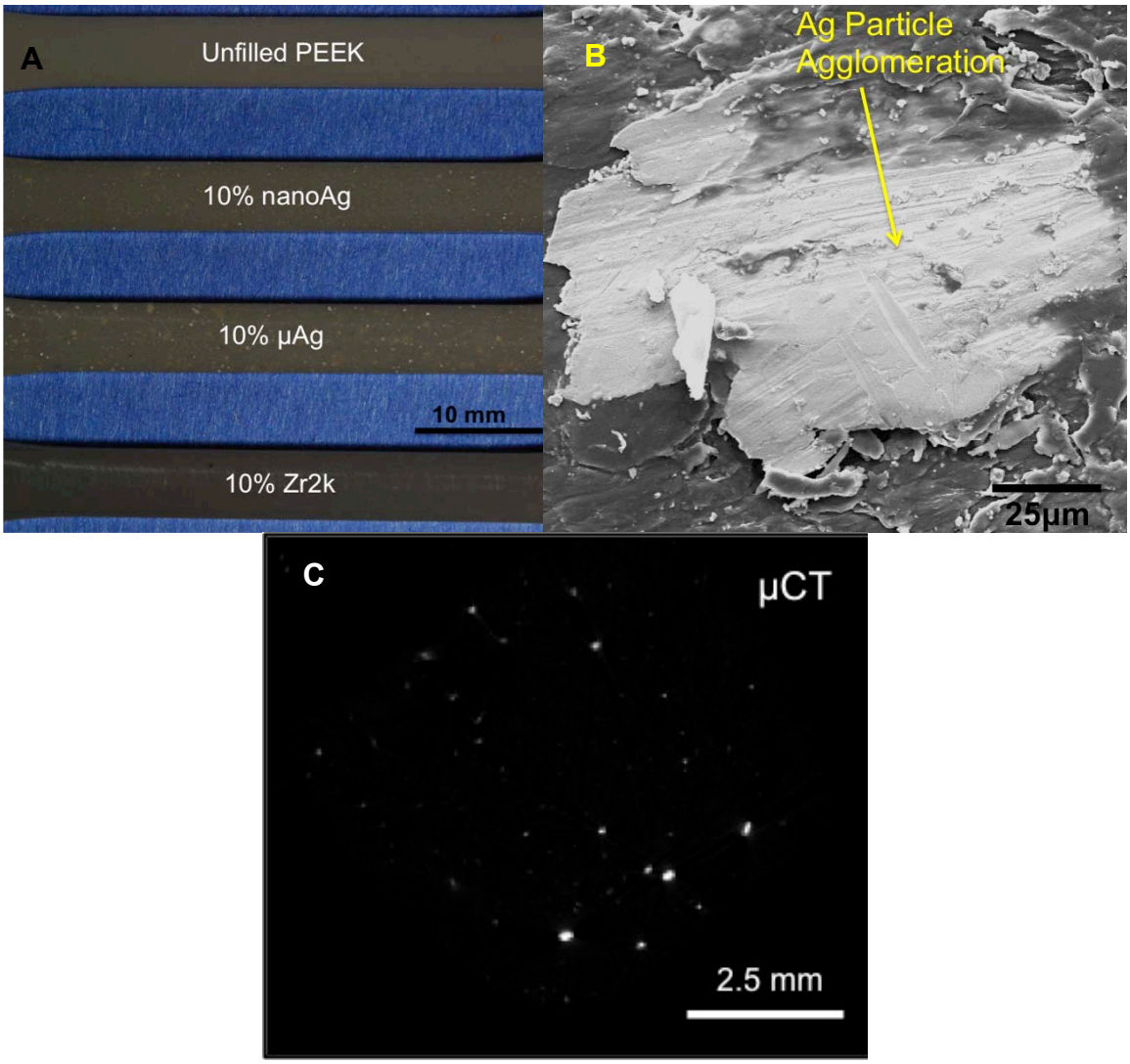

Figure 3-2: 10% composite surfaces are displayed in 1.25x magnification where Ag agglomeration is observed (A). SEM image displays a Ag deposit greater than 50 µm on the injection molded surface of a 10% nanoAg composite (B), which is also apparent after imaging the bulk of the polymer with µCT (C).

Mechanical Behavior

For all 2-5% loaded composites, no significant difference ($p \geq 0.1$) could be detected in peak load or stiffness (Table 3-4, Figure 3-3), except for the 5% Zr2k material, which exhibited a slightly lower peak load ($p \geq 0.03$). Similarly, there were no significant differences between peak load or stiffness between the

unfilled control and the 10% composites ($p \geq 0.12$, Figure 3-4). Ultimate displacement and energy to failure (Figure 3-5 & 3-6), was significantly greater ($p \leq 0.02$) for the unfilled control group for all composites with 2-10% loadings. The only exception was the 2 and 5% Zr2k ($p \geq 0.24$). Fracture surfaces were similar across all samples, nevertheless, more plastic deformation was observed on the control samples (Figure 3-7)

Table-3-4: Results from small punch testing (mean ± SD).

Material	Filler Amount (%)	Stiffness (N/m)	Peak Load (N)	Ultimate Load (N)	Ultimate Displacement (mm)	Energy (mJ)
LT1 – 2-5%comp	0	0.20 ±0.05	227 ± 9	202 ± 11	2.62 ± 0.12	412 ± 15
NanoAg	2	0.22 ± 0.03	222 ± 4	191 ±4	2.36 ± 0.18	361 ± 31
	5	0.21 ± 0.01	220 ± 6	183 ± 14	2.19 ±0.18	323 ± 41
µAg	2	0.22 ± 0.03	221 ± 8	172 ± 45	2.25 ± 0.15	334 ± 42
	5	0.27 ± 0.02	222 ± 6	163 ± 43	2.19 ± 0.16	326 ± 42
Zr2k	2	0.27 ± 0.03	225 ± 3	188 ± 3	2.71 ± 0.07	434 ± 13
	5	0.24 ± 0.05	216 ± 4	170 ± 3	2.52 ± 0.11	379 ± 28
LT1 - 10%comp	0	0.19 ± 0.04	225 ± 6	205 ± 12	2.61 ± 0.10	413 ± 25
NanoAg	10	0.24 ± 0.05	227 ± 7	206 ± 11	2.24 ± 0.17	343 ± 41
µAg	10	0.26 ± 0.07	217 ± 6	185 ± 9	2.25 ± 0.23	335 ± 43
Zr2k	10	0.26 ± 0.05	225 ± 7	185 ± 16	2.15 ± 0.17	332 ± 36

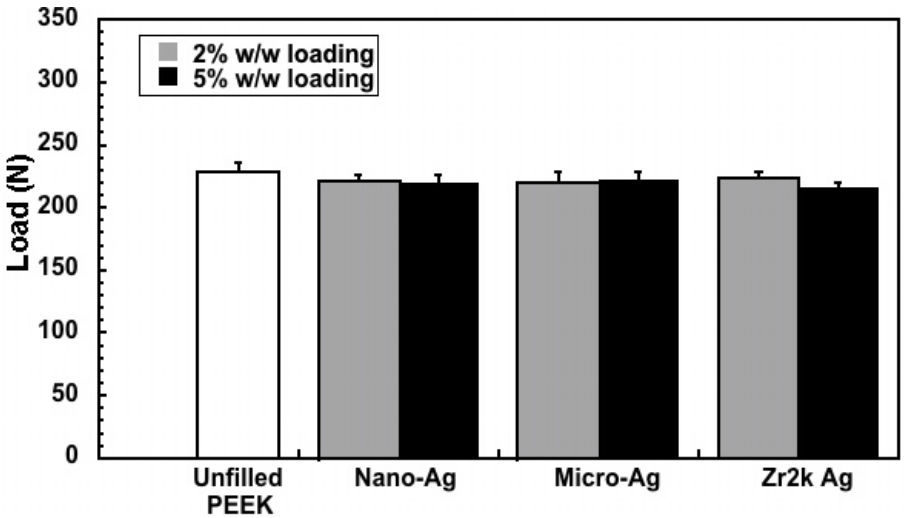

Figure 3-3: Average peak load (±SD) for 2-5% composites.

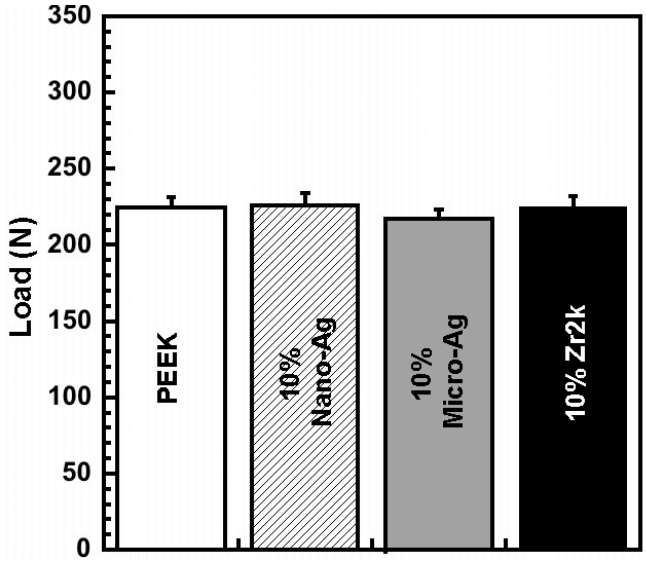

Figure 3-4: Average peak load (±SD) for 10% composites.

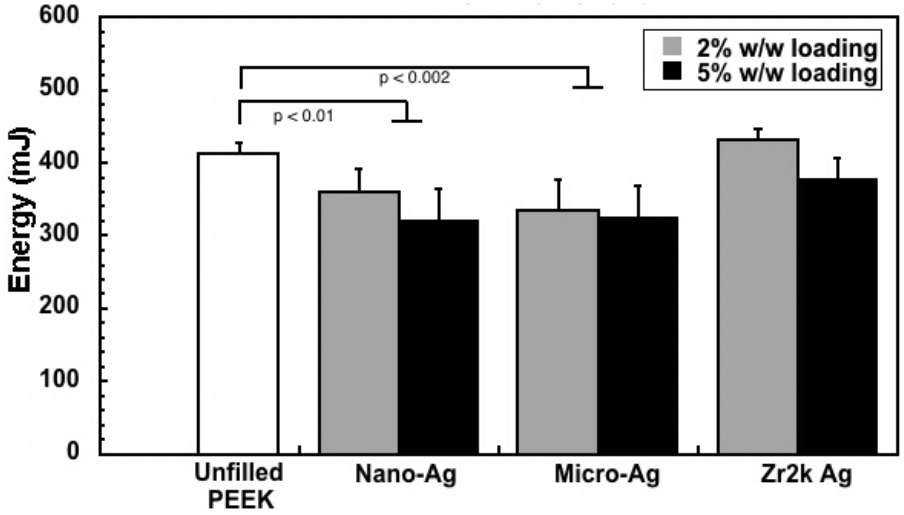

Figure 3-5: The average Energy (±SD) to failure for 2-5% composites.

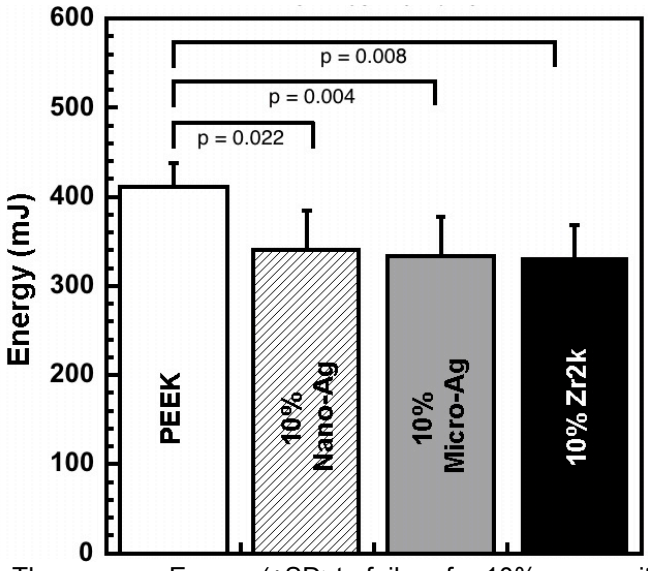

Figure 3-6: The average Energy (±SD) to failure for 10% composites.

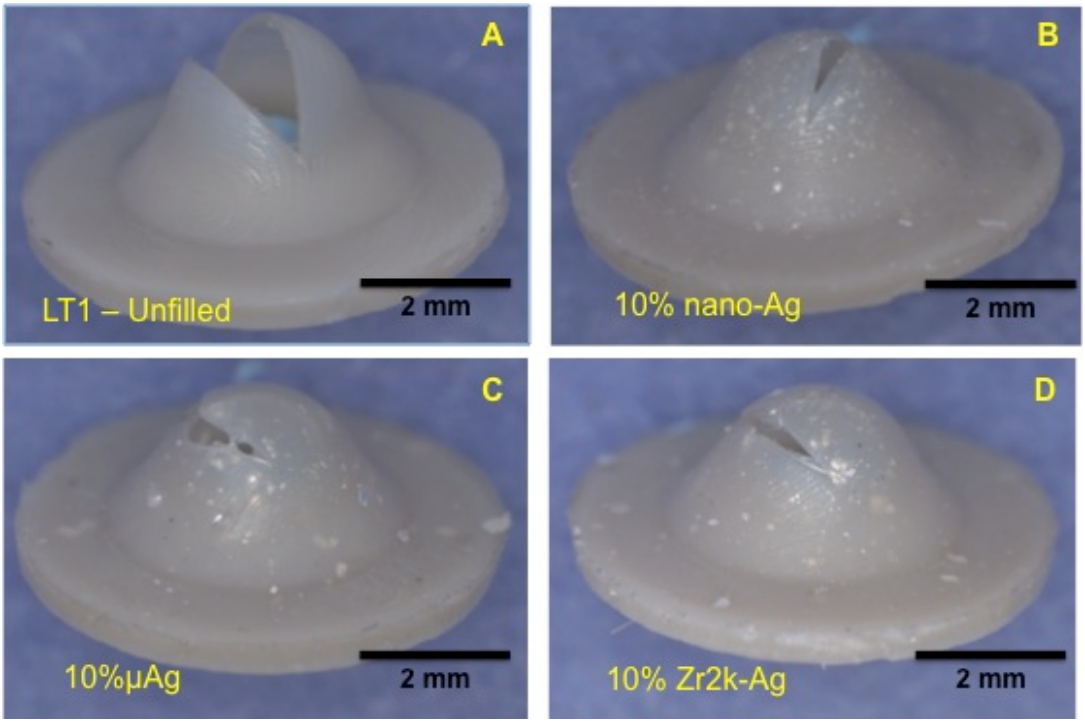

Figure 3-7: Fracture surfaces for unfilled control (A), 10%nanoAg (B), 10%µAg (C), and 10%Zr2k. Fracture surface were similar between groups, but the control sample displayed increased plastic deformation.

Surface Colonization of Bacteria

We next determined if the composite surfaces inhibit bacterial colonization over a 48 hour time period. With up to 5% incorporation of Ag particulate, no significant reduction in surface-adherent bacteria could be observed on injection molded (Figure 3-8, $p \geq 0.07$) and machined ($p \geq 0.64$) surfaces at time points up to 48 hr. Similar patterns were initially observed when the surfaces were challenged with *S. aureus* in alternative sodium enriched media (BHI, $p \geq 0.33$), and also when incubated with another periprosthetic infection related pathogen, *E. coli (*$p \geq 0.25$). Repetition of experiments and SEM imaging confirmed results.

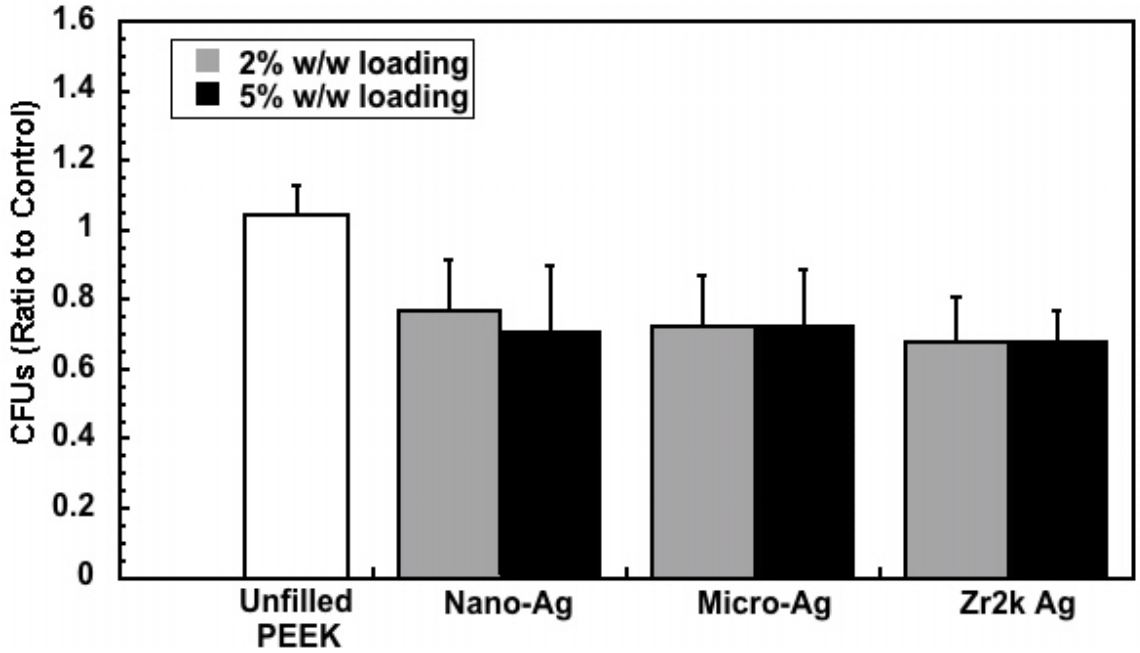

Figure 3-8: Incubation of injection-molded surfaces with *S. aureus* for 48 hr exhibited no significant reduction in adherence with 2% and 5% composites. Results are the mean ± standard deviation for control (white), 2% (grey), and 5% (black) composites. Results were normalized to controls after cfu were harvested from surfaces and counted.

When Ag additive loading was increased to 10%, a trend towards reduced colonization of the surfaces could be seen, although it was variable depending on the surface. When composites and controls were incubated with *S. aureus* for 48 hr, one trial showed no significant reduction in bacterial adhesion (Figure 3-9a, $p \geq 0.25$), whereas, another trial had over an 80% reduction in attached bacteria (Figure 3-9b, $p \leq 0.002$). NanoAg, μAg, and Zr2k injection molded surfaces exhibited significant reduction (>50%) in surface colonization in 4/12, 6/12, and 5/12 trials, respectively. This variability in the reduction in bacterial adhesion was observed on both injection molded and machined surfaces when incubated with *S. aureus* in TSB. The trend towards lower colonization was confirmed with SEM imaging, and validated the reported trends. Similar variable results were observed in BHI media; furthermore, there was no significant reduction observed when samples were challenged with *E. coli* for up to 24 hr ($p \geq 0.08$).

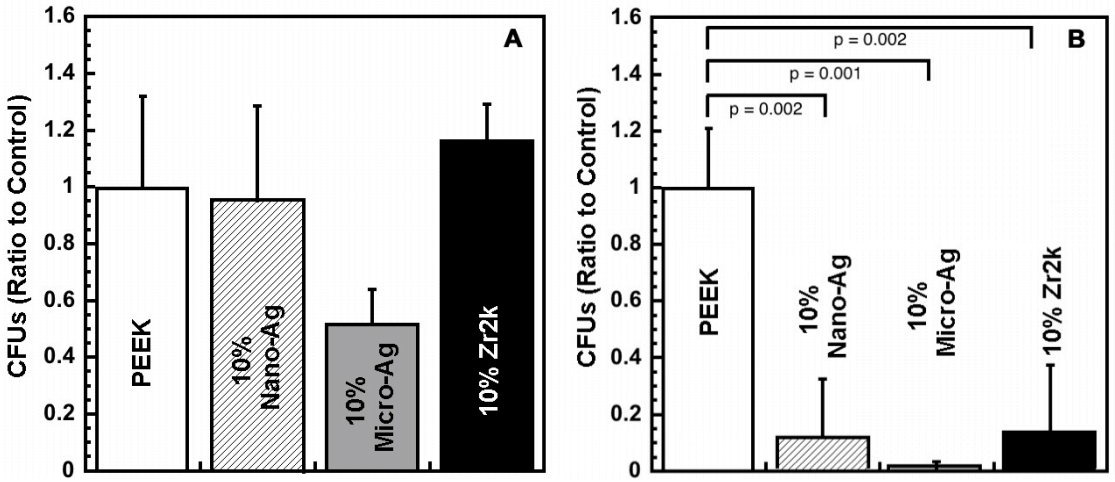

Figure 3-9: 10% Ag-PEEK composites were incubation with *S. aureus* for 48 hr. No significant reduction in surface adherence was measured when compared to unfilled controls in some trials (A), while significant reduction was found in repeated trials (B). Results were normalized to controls after cfu were harvested from surfaces and counted.

Ag^+ release is driven by oxidation of $Ag^0 \rightarrow Ag^+$ in aqueous media, however, based on FIckian case I diffusion kinetics, H_2O uptake into the PEEK matrix is initially slow [103, 116]. A 1mm sample could take over 96 hr to reach full hydration [103, 116]. To induce increased water content prior to incubation and initiate Ag oxidation earlier, samples were incubated at 60ºC in DI H_2O for 72 hr prior to testing. Following 12 hr of exposure to *S. aureus* in TSB, these pre-incubated composite materials showed no significant decrease in bacterial adhesion when compared to unfilled PEEK controls ($p \geq 0.37$) (Figure 3-10).

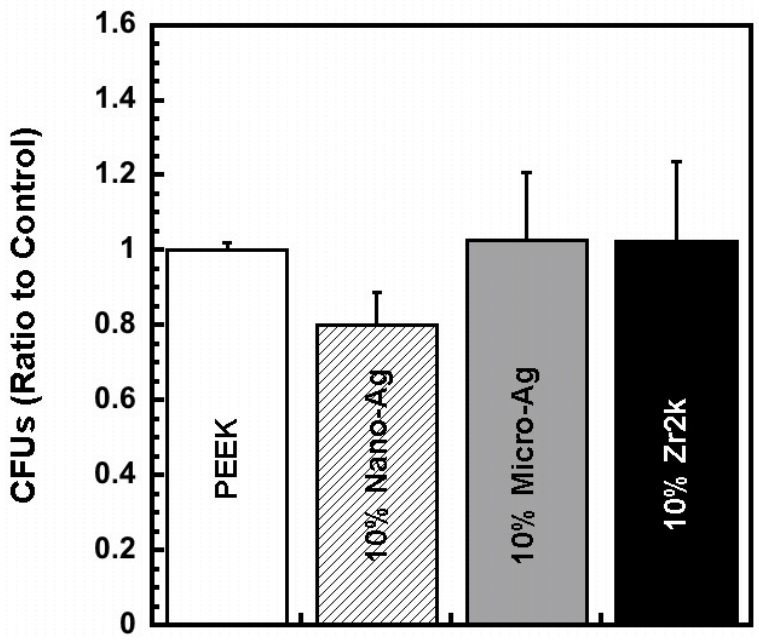

Figure 3-10: 10% Ag-PEEK composites were soaked in DI H_2O for 72 hr at 60ºC prior to incubation with *S. aureus* for 12 hr. No significant reduction in surface colonization was observed. Results were normalized to controls after cfu were harvested from surfaces and counted.

Biocidal Activity

To observe biocidal activity, *S. aureus* was incubated directly on material surfaces as described previously. Samples filled with Zr2K displayed either

complete eradication of all bacteria or >99% reduction in living bacteria (Figure 3-11a); effects of the nanoAg or μAg composites were small (p≥0.83). When the test was repeated with samples that had previously been hydrated for 72 hr, bacteria survived at levels similar to controls on all surfaces (p>0.8) (Figure 3-11b).

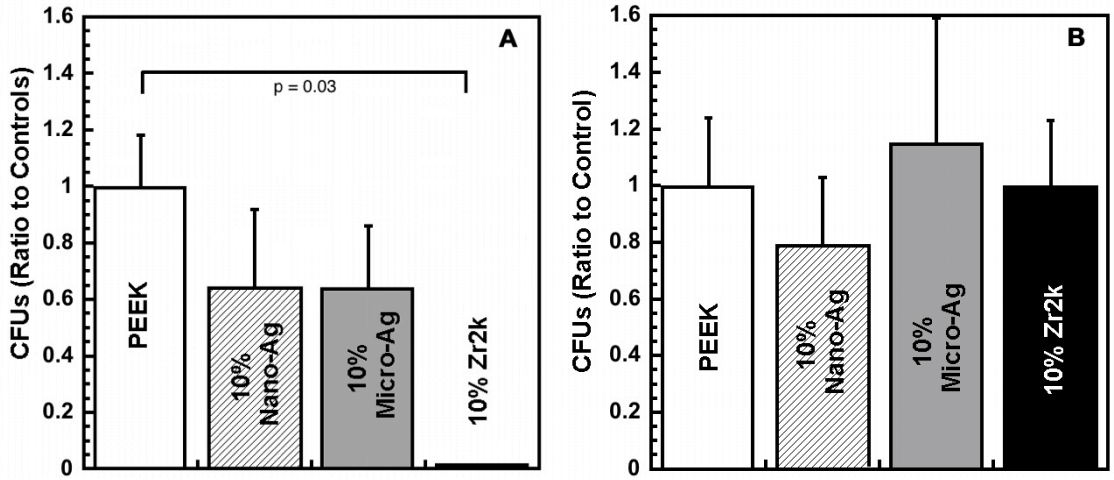

Figure 3-11: Biocidal activity was consistently observed in repeated trials with the 10%Zr2k (A). If the samples were soaked for over 72 hr before testing, no reduction in numbers of adherent bacteria was measured (B). Results were normalized to controls after cfu were harvested from surfaces and counted.

Ag Elution

Using atomic absorption spectroscopy, Ag^+ eluted to detectable levels from all 10% composites within 48 hr in either PBS or DI H_2O (Figure 3-12a & b). No Ag could be detected in the media incubated with unfilled PEEK. NanoAg and μAg composites show a consistent and near linear release ($R^2 \geq 0.99$) over the course of testing in both media. In contrast, Zr2k showed a burst release of Ag^+ within the first 48 hr in PBS, but tapered off so that no significant amounts of

Ag^+ were released by 200 hr. At 48 hr, the cumulative media concentration of Ag for 10% nanoAg, μAg, and Zr2k in PBS was 34 ± 8, 82 ± 15, and 449 ± 28 μg/l, respectively.

.

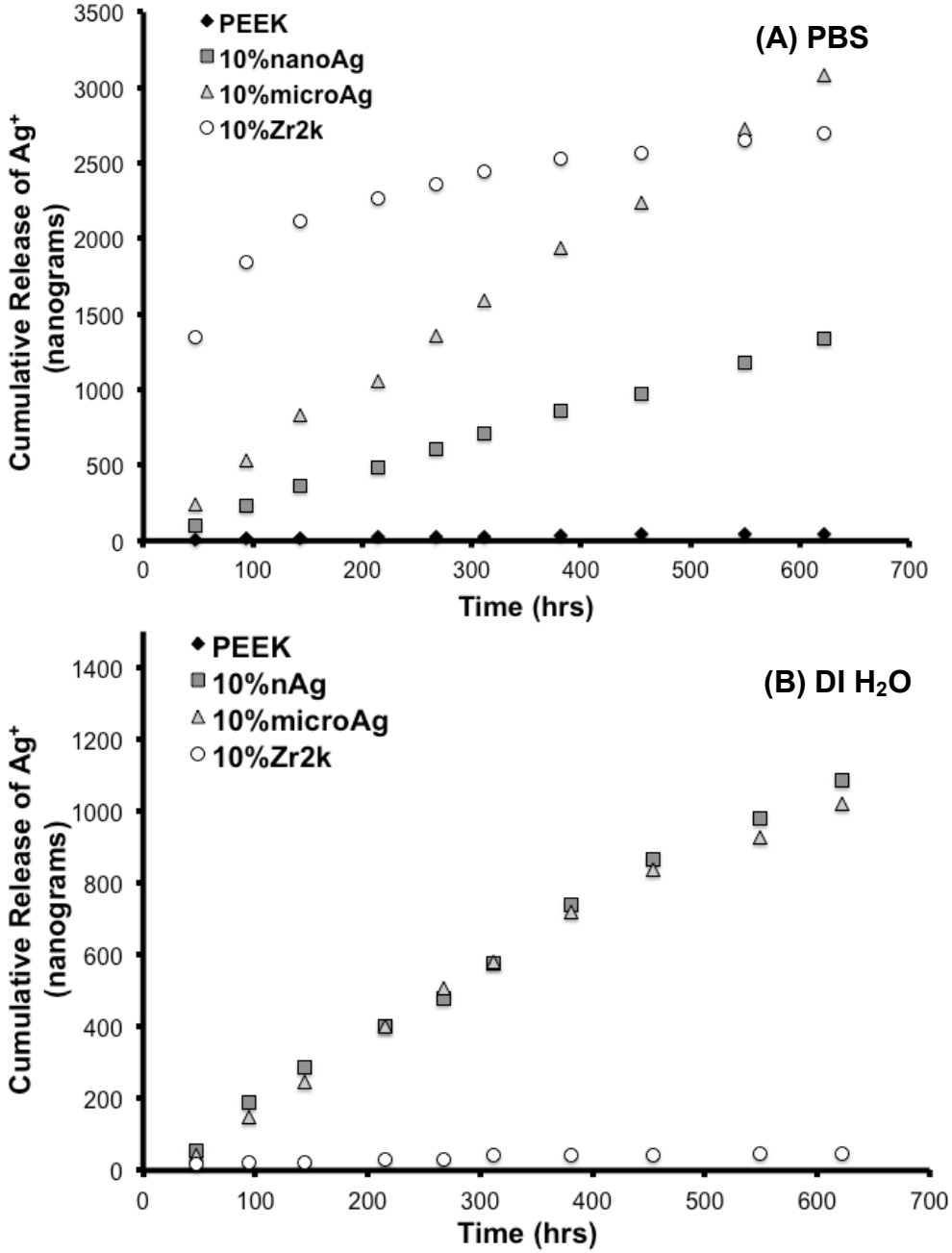

Figure 3-12: Ag elution from the 10% composite materials for 25 days is displayed as cumulative mass released in PBS (A) and in DI H_2O (B).

Theoretical Model Comparison

The experimental elution data was lower than predicted values from the model for nanoAg and μAg when modeled for a theoretical 10% or the actual loading ratios determined by density analysis (Figure 3-13 & 3-14). Lowering the loading ratio of Ag within the model did not reduced to the predicted elution to similar levels as the experimental data. Data comparison with alternate activation energy values, E_a, is included in the Appendix E.

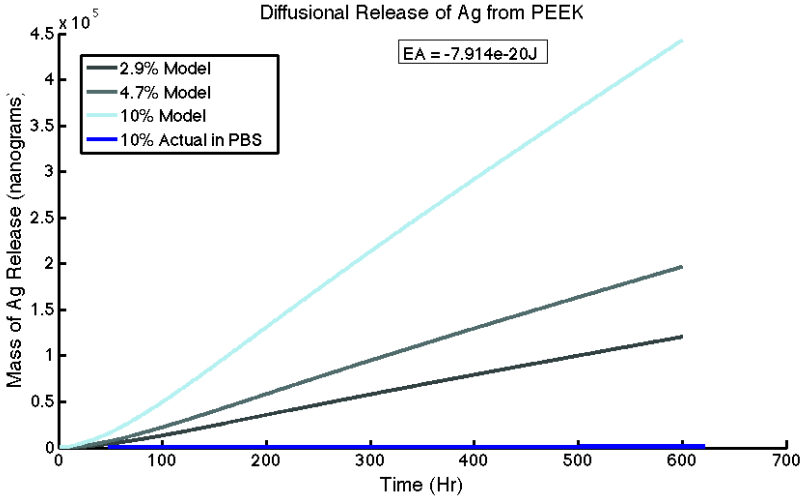

Figure 3-13: Experimental elution data was compared to model predictions for 2.9, 4.7, and 10% nanoAg loading ratios.

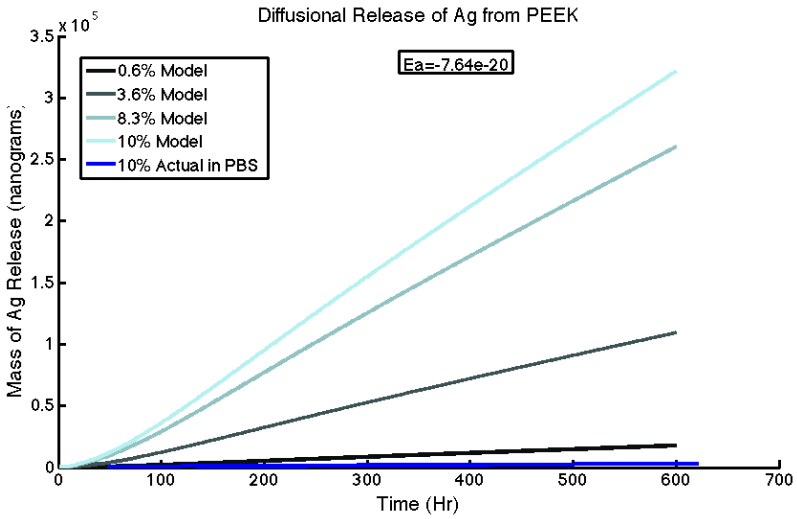

Figure 3-14: Experimental elution data was compared to model predictions for 0.6, 3.6, 8.3, and 10% μAg loading ratios.

The model comparison highlights the fact that the reduced Ag^+ elution is due to more than merely lower than targeted loadings. The measure release is an order of magnitude lower than the model; however, the 0.6% loading ratio profile was similar to the experimental results for the targeted 10% μAg elution trial. For model fitting, the actual value for matrix loading determined by density analysis for both 10%nanoAg (4.7% or 0.063 g/ml) and 10%μAg (8.3% or 0.115 g/ml) was the assumed loading ratio. To account for the differences between the model predictions and experimental data, the diffusion coefficient, D, was modified based on the results since the exact value was unknown for Ag^+ in PEEK. The model could not fit "D" if the bounds to the variable were held at $-\infty$ and ∞. When the boundary limits were set within the range of diffusion coefficient values published for PEEK ($7.2x10^{-6}$ to $3.55x10^{-4}$ cm^2/hr), a poor fit was produced in all cases (R^2<-6094), where the fitted valued for D was held at the lower bound of the limits (Table 3-5, Figure 3-15). If the lower bound was

expanded to $7.2x10^{-10}$ cm^2/hr, the fit only became slightly better (R^2=-5) and was still fixed at the lower bound.

Table 3-5: Fitted coefficient values and measured error between the fitted model and the experimental data.

Material	Variable Fitted	Variable Fit				Error	
		Agglomeration Factor "z"	Confidence bounds	Diffusion Coefficient	Confidence bounds	SSE	Adjusted R^2
NanoAg	D	N/A		7.20E-6	fixed at bound	3.1E+11	-1.86E+5
	z	0.002	(0.001701, 0.001906)	N/A		3.49E+4	0.9764
	z & D	0.004	(-6.1e+06, 6.1e+06)	7.43E-6	(-2.065e+04, 2.065e+04)	3.49E+4	0.9735
μAg	D	N/A		7.20E-6	fixed at bound	5.4E+11	-3.27E+5
	z	0.001	(0.001283, 0.001438)	N/A		3.49E+4	0.9764
	z & D	0.003	(-1.641e+07, 1.641e+07)	7.37E-6	(-1.646e+04, 1.646e+04)	3.49E+4	0.9735

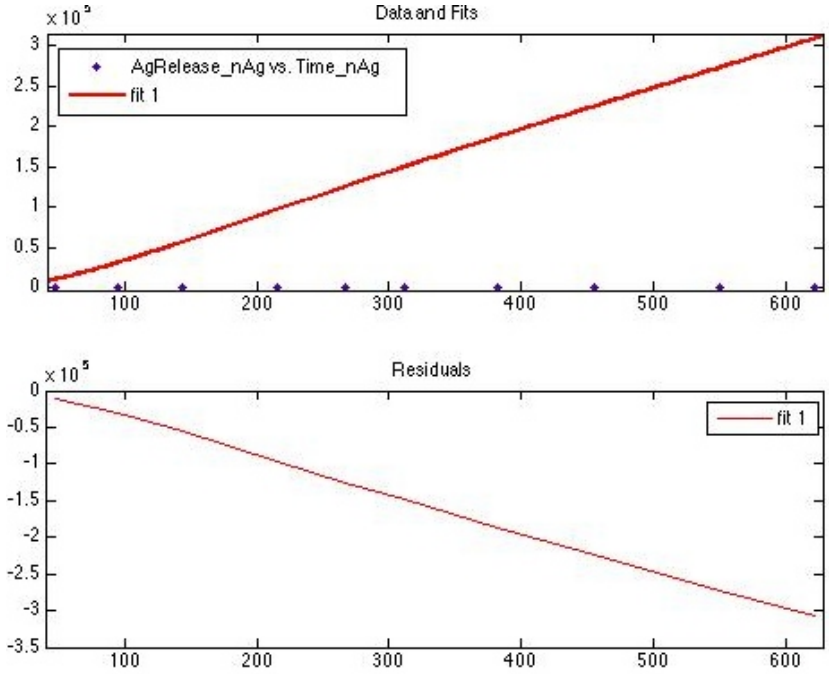

Figure 3-15: Model fit and residuals after fitting experimental nanoAg elution data for diffusion coefficient, D.

Diffusion coefficient coupled with lower Ag loadings, did not compensate for the lower release from Ag composites. For this reason and based on results from previous sections, an agglomeration coefficient, “z”, was incorporated into

the model as directly proportional to "C" or $[Ag]_{initial}$. A value of "1" would indicate that all particles are uniformly dispersed and there is no aggregation. "0" would indicate that all particles aggregated into masses larger than 100 μm in diameter. 100 μm was chosen because this is the larger particle size observed on Ag-PEEK composite surfaces. In addition Ag particles greater than 45 μm in diameter exhibited little to no antibacterial properties in Chapter 2. Experimental data was fitted for "z" independently with D set as the diffusion coefficient of water (0.000044 cm^2/hr). For all cases of fitting z, the model fit had high correlation coefficients (adjusted R^2=0.97, SSE=3.5x10^4, Table 3-5, Figures 3-16 & 3-17) and suggested a high agreement between the model prediction and experimental data. If the model was fitted for both z and D, similar values for z were obtained as in the previous fit (range: 0.001 to 0.004, Table 3-5); however, D was only slightly higher then the lower bound (~7.4x10^{-6} cm^2/hr).

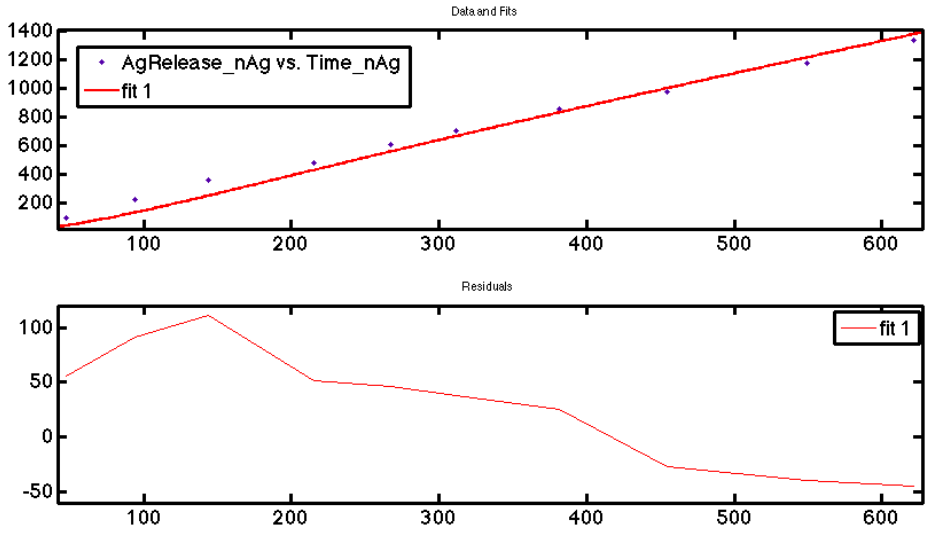

Figure 3-16: Model fit and residuals for nanoAg elution trials when fit for agglomeration coefficient "z" independently while D was the diffusion coefficient of water (0.000044 cm^2/hr).

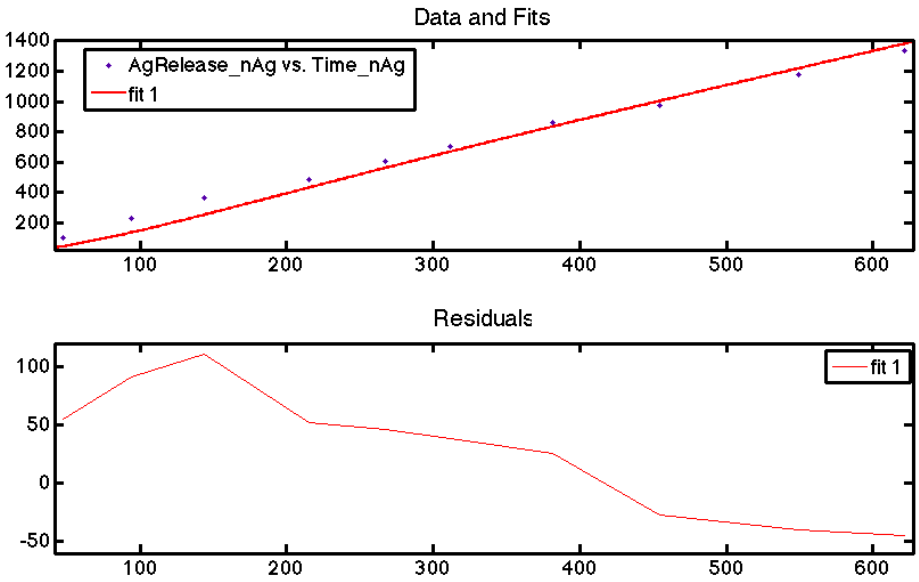

Figure 3-17: Model fit and residuals for nanoAg elution trials when fit for agglomeration coefficient, z, and diffusion coefficient, D.

Discussion

The consequences of periprosthetic infection can be devastating and include aggressive antimicrobial treatments, increased hospital stay, elevated costs, and multiple surgical interventions. These infections are especially difficult to treat because the implant surface provides an ideal substrate for bacterial adherence and biofilm formation. Once adherent and encased within a biofilm, these bacteria become sequestered from the immune system and are difficult to treat without removal of the implant, aggressive antimicrobial treatment, and ultimately re-implantation of the device; reinfection rates can be as high as 50% for these implant-associated infections [14, 24, 76, 125, 136]. Because PEEK has increasingly been used across the spine and orthopaedic industries, we have

asked if we can impregnate PEEK with different forms of Ag to prevent bacterial attachment and biofilm formation. While these Ag-PEEK composite materials were unable to reduce bacterial adhesion at lower loading ratios (2-5%), higher loading ratios of Ag significantly reduced *S. aureus* attachment (>50%) in half of the trials; these materials sustained linear, long-term Ag^+ release.

All composites used in this study were manufactured using a twin-screw extrusion method similar to industry techniques for creating PEEK composites. Unfortunately, this method led to nonhomogeneous dispersion of the Ag particulates. Melt processing such as twin-screw extrusion was considered first because it is economically feasible and these fabrication techniques are already successfully used [137]. In addition, due to equipment restrictions, the 2-5% composites were injection molded in a separate facility than the 10% composites, perhaps resulting in variability in the crystallinity and melt flow processing. To control for this difference, experimental samples were compared to unfilled PEEK controls produced in the same facility. While slight differences in crystallinity can be expected on the basis of this [77, 99, 138], we used strict manufacturing guidelines to minimize any changes. An additional limitation in the characterization of the material was in the detection of Ag^0 associated with a particle vs. the Ag^+ in solution. Atomic absorption spectroscopy can only detect the total concentration of Ag in solution and we think it is unlikely that this Ag concentration is due to particulate Ag as the high density, 1.3 g/cm^3, and low porosity of PEEK makes it unlikely that particles of the sizes used in this study would be able to be released from the bulk of the material. It is possible that

superficial particles could be dislodged within the first 48 hr of elution and be included in the atomic absorption values; we would not expect these surface-associated events to influence the later time points within the study.

In previously published studies, 2, 4, and 8 w/w% of Ag was loaded into polyamide to produce successful antimicrobial constructs [76, 125, 126]. Since PEEK is denser and less porous than other biomaterial polymers previously used with Ag, we reasoned that higher amounts of Ag might be required to achieve the desired release for antimicrobial effects [76, 126]. Therefore, loading ratios of 2%, 5% and 10% were selected. This is consistent with our previous work with our implant retrieval program where antibiotic bone cement spacer loads were as high as 8.7 to 12% [24]. As shown by density analysis, composites did not reach the target filler ratios for any of the loading ratios or particulate types. Furthermore, the twin-screw extrusion process was unable to prevent aggregation of Ag particles and promote uniform dispersion. In fact, independent of the loading ratios, large agglomerations of Ag were present as detected by SEM and μCT. Extruding with pellet grad material also resulted in decreased loading where <1% and <3% loading was measured for the targeted 2% and 5% composites for nanoAg. Furthermore, filler composition may also be important as filler can affect the cooling rate, which influences crystalline region growth. Specifically, slower cooling from melt induces crystal formation and a higher degree of crystallinity [77, 138]. Interestingly, incorporation of filler did not influence the crystallinity of the PEEK matrix for the nanoAg or μAg composites. However, an increase in crystallinity was reported in Zr2k, especially with a

loading of 10% (47% crystallinity). This increased crystallinity may occur because the Zr2k particle, which consists of 90% sodium hydrogen zirconium phosphate, may act as an insulator in the matrix causing slower cooling during the injection molding process. Presumably because of the different facilities, a small but significant difference in crystallinity ($p=0.02$) was also measured between the controls (unfilled PEEK) for the 2-5% and 10% molded groups (25% and 28% crystallinity respectively). Overall, all crystallinity values for the controls as well as the composites, other than the 10% Zr2k, were within normal ranges for injection molded PEEK. As mold temperatures can range from 170 to 210°C, small differences in crystallinity are most likely due to localized differences in mold temperatures which in turn slightly alter the cooling rates.

It has been previously shown in Chapter 1 that the most sensitive parameter to changes in PEEK materials is peak load [131]. Therefore, the results imply that the loading of the PEEK matrix does not have a significant impact on the static mechanical properties of the material before plastic deformation. Minimal to no changes should be expected since a mass loading ratio of 10% would only be a volume ratio of ~1%. However, further studies would have to be performed to fully characterize the influence of Ag fillers on dynamic and fatigue properties. In contrast though, ultimate displacement and thus energy to failure was significantly lower for most composites when compared to controls (343 to 413 mJ respectively). Since peak load and stiffness (slope of the linear elastic region of the curve) were not significantly different from controls for most groups, ultimate displacement would be linked to energy to failure and is

calculated as the area beneath the load-displacement curve. As samples reach similar peak loads, the ultimate displacement (or the displacement at material failure) would define the extent of plastic deformation and energy required to fracture the material. The addition of filler material, which is not bonding to the matrix, could increase brittleness and reduce plastic deformation potential of the composite [81, 82, 139]. The unfilled PEEK is able to deform longer before defects (i.e., the Ag particles) encourage breaking and failure of the material. These findings would be significant if the specimens were deformed beyond yielding and began plastic deformation. However, in most medical application for which PEEK is used, implants should be engineered to endure stress without yielding. Once a material has gone beyond yielding, the implant has most likely already failed for load bearing applications.

Bacterial adhesion was not significantly reduced using 2-5% composites. Similar results were obtained with composites incubated in alternative media or with machined surfaces. When loading was increased to a target of 10%, significantly fewer adherent bacteria (>50%) were recovered, although there was variability between trials. Machined surfaces, which accounted for a polymer-skin phenomenon that can cause low surface deposition of Ag, did not normalize the antimicrobial effects of the composites. Assuming that Ag^+ are the primary antimicrobial form of Ag, the results would imply that injection molded surfaces provided no extra barrier to Ag^+ release. One potential cause for the variability in antibacterial activity (and by implication, elution) lies in the presence of the many different particle sizes that are present both superficially and throughout the

material. Previous studies have shown that particle aggregation (which reduces accessible surface area) lowers Ag elution rates. Specifically, dispersal of a given amount of Ag into smaller particles will result in a larger specific surface area and increased potential for oxidation of $Ag^0 \rightarrow Ag^+$[48, 49, 65]. When monitoring direct Ag^+ elution from Ag nanoparticles, Zhang et al. noted aggregation influenced particle size distribution and altered the ion release kinetics by altering the available surface area [65]. Thus the combined effects of lower than targeted Ag loading with increased agglomeration greatly reduced the potential for Ag^+ generation from these composite materials. We suggest that the variability that we saw in antimicrobial properties of the Ag-PEEK was at least in part due to the inconsistent Ag aggregation and matrix loading.

Implant-associated infection involves both planktonic bacteria and implant-adherent bacteria that can encase themselves in a biofilm to cause persistent infection. In this report, we initially measured the effects of the composite surface on adhesion of bacteria. We then used ISO 22196 to measure the biocidal potential of these composites against a known number of bacteria, where the diluted media sustains bacterial viability without encouraging proliferation and logarithmic growth. As in the case of the adherent bacteria, the results from the biocidal testing were variable with the nanoAg and µAg composites. This is in contrast to 10%Zr2k, which reproducibly decreased the number of viable bacteria by at least 10-fold. Because this bactericidal effect was not observed when the composites had been pre-incubated, we surmise that the 10%Zr2k may be exhibiting a rapid elution, perhaps from the particles directly on the surface,

followed by an attenuated elution, which is insufficient to retard bacterial colonization.

Our elution trials supported the interpretation of the biocidal testing. During the initial 48 hr, release of Ag was greatest for the Zr2k composites but subsequently, elution rapidly declined below the levels for the nanoAg and μAg composites; release from the Zr2k plateaued by day 6. These data further confirm that the antimicrobial mechanism for these Ag composites was dependent on Ag^+ release. In addition, because the 10% Zr2k had crystallinity levels averaging 47%, the density of this material compared to a material at normal levels of crystallinity (25-32%) [77, 99] would be higher and pose additional barriers to diffusion/elution from the bulk of the composite. Therefore, with the waning of Ag^+ elution, the biocidal activity also wanes, limiting the extended use of this material.

As originally proposed, 10% nanoAg and 10% μAg materials were able to sustain a long-term linear release of Ag over the 26 days monitored. The steady release from the pure Ag-composite materials implies that water uptake into the bulk material was able to maintain oxidation of Ag to produce Ag^+ and sustain release. Despite the long-term steady release, reduction in bacterial adhesion was still inconsistent. Media concentration of Ag by 48 hr ranged from 34 to 82 μg/l. Jung et al. reported the minimum inhibitory concentration (MIC) of Ag^+ for 10^5-10^6 cfu to be approximately 50 μg/l for both *S. aureus* and *E. coli* [44]. The MIC falls directly in the mid range of our measurements for elution of Ag^+ from the pure Ag-composites after 48 hr.

The model proposed in Chapter 2 was able to predict the release of Ag^+ from nanoAg and μAg with a high correlation (adjusted R^2=0.97); however, this was only possible when an agglomeration coefficient, z, was introduced into the model. Adjusting the diffusion coefficient alone produced a poor correlation between the model and the data. Agglomeration coefficient values ranged from 0.001-0.004, which implies the particles are highly aggregated within the matrix. These results supported the hypothesis that the particle agglomeration directly influenced the elution capabilities of Ag-PEEK composites. The diffusion coefficient can play a role in the elution potential of Ag composite materials, but to a limited extent and must be combined with multiple factors to compensate for lower elution.

The results reported lay an important foundation in developing bactericidal PEEK composites with a reservoir of antibacterial agents for long-term release. This paper serves as a proof of concept for that scenario, and future studies must focus on optimizing a manufacturing process for the Ag-PEEK composites to yield a material that consistently produces Ag^+ in levels above bacterial MICs

Conclusion

Compositing of Ag particulate with PEEK had minimal to no significant effect on crystallinity of matrix or static mechanical behavior. Reduction in bacterial adhesion to the 10%-Ag-PEEK composites surfaces occurred but was

variable, and most likely due to nonhomogeneous distributions of Ag aggregates. 10%nanoAg and 10%μAg PEEK produced linear, long-term release of Ag^+ at concentrations slightly below or within the bactericidal ranges for *S. aureus* and *E. coli*. Zr2k composites released Ag^+ rapidly within the first 48 hr at biocidal levels; however, this release decreased quickly beyond 96 hours. These data suggest that an optimized manufacturing process could potentially yield a Ag-PEEK biomaterial with antimicrobial properties and long-term Ag^+ elution potential.

Conclusions

This dissertation detailed the development of silver-PEEK (Ag-PEEK) composites to prevent bacterial colonization and the techniques designed to characterize and model new composite materials. Overall, Ag-PEEK materials were able to sustain long-term Ag^+ release at potentially inhibitory concentrations with minimal impact to the structure and mechanical properties of the base PEEK material.

The studies in Chapter 1 established techniques for the micro-characterization of PEEK materials and allowed for smaller-scale material development to be conducted on expensive and limited materials. For many PEEK implants, standard characterization techniques for crystallinity and mechanical properties may not be applied due to complex/non-uniform dimensions and limited material quantities. Chapter 1 first established specular reflectance Fourier transform infrared spectroscopy (R-FTIR) as a tool for characterizing the level of crystallinity for PEEK and PEEK composites within as small an area as 300 μm^2. The R-FTIR method was non-destructive in nature and could be universally applied to unfilled, carbon fiber reinforced, and radiopaque PEEK grades without interference of signal. Though able to measure crystallinity in virgin PEEK forms, the standard measurement technique, wide-angle x-ray scattering (WAXS), was more time intensive for testing, had larger dimensional restrictions, and involved complex curve-fitting procedures to obtain crystallinity measurements for filled materials such as radiopaque composites.

Additionally, Chapter 1 described the validation of the small punch test for micro-mechanical investigation of new PEEK materials. Because of its multi-directional nature, the small punch test detected alterations in the mechanical behavior with only a small amount of material required for analysis. Specifically, small punch testing reproducibly characterized the mechanical behavior of PEEK and distinguished differences in molding parameters, crystallinity, and filler material. Peak load was established as the most sensitive parameter to alterations in material, and ultimate displacement was found to negatively correlate with crystallinity. The results implied the higher crystalline materials were less ductile in nature.

In Chapter 2, the inherent antimicrobial properties of Ag particles were examined through minimum inhibitory concentration (MIC) testing on agar gels, which revealed a size-dependent effect on the reduction of bacterial growth. Ag particles >8μm in diameter exhibited little to no effect on bacterial growth, while the smallest particles (100 nm, nanoAg) displayed complete inhibition at lower concentrations. Previous studies have noted Ag nanoparticles have greater antimicrobial properties than larger diameter counterparts. The increased biocidal effects were due to larger surface area to mass ratio exposing more surface atoms for the oxidation of Ag^0 to Ag^+. This concept was confirmed after additionally observing significant bacterial inhibition with a larger diameter particle (8 μm) that was designed with a porous structure to have a similar surface area to mass ratio as 100 nm particles (5 m^2/g). Using the properties of the nanoAg or μAg particles, a model for Ag incorporation into PEEK was

developed by combining known models for the oxidation of Ag^0 to Ag^+, Fickian case I diffusion of H_2O into PEEK, and the Higuchi method of drug release from a solid polymer. The idealized model predicted Ag^+ release at levels above MIC for *E. coli* and *S. aureus* when PEEK matrices were incorporated with ≥1% of Ag particles.

In Chapter 3, three Ag-PEEK composites were fabricated with nanoAg, μAg, or Zr2k (commercial antimicrobial Ag-phosphate) particles at targeted loading ratios from 2-10%. Incorporation of Ag particles had minimal to no significant effect on crystallinity of matrix or static mechanical properties. Composite fillers had no significant impact on peak load measured by small punch testing; however, energy to failure and, thus plastic deformation, was slightly lower for Ag-PEEK materials. Bacterial adhesion to the 10% Ag-PEEK composites surfaces was significantly reduced, but the effect was variable (in ~5 out of 12 trials) and most likely cause by nonhomogeneous distributions of Ag aggregates. 10% nanoAg and 10% μAg PEEK produced linear, long-term release of Ag^+ at concentrations slightly below or within the minimum inhibitory ranges for *S. aureus* and *E. coli*. The analytical model for Ag^+ release from Ag-PEEK composites further supported results. The predicted release was an order of magnitude higher than experimental values and was only able to match experimental release profiles after the introduction of an agglomeration factor that directly influenced the initial matrix concentration of Ag. Zr2k composites released Ag^+ rapidly within the first 48 hr at biocidal levels, however, this release decreased quickly beyond 96 hours.

The results detailed in the previous chapters lay an important foundation in developing bactericidal PEEK composites with an integrated reservoir of antibacterial agents for long-term inhibitory effects. This dissertation serves as a proof of concept, and future studies should focus on a manufacturing process for the Ag-PEEK composites to yield a uniformly dispersed material. With process optimization, the Ag content of PEEK can be tuned to achieve sustainable, bactericidal levels of Ag^+ release. A potential manufacturing pathway for future studies could be pre-mixing PEEK powder and Ag particles in ethanol and ultrasonically dispersing particles prior to molding. This has previously been successful in uniformly dispersing nanoparticles and hydroxyapatite whiskers into polyaryletherketone polymers without particle agglomeration; although, this method excludes the use of industrial standard injection molding techniques for compression molding methods [81, 82, 137, 139]. Porogen materials, such as NaCl, could also be molded with Ag and PEEK to subsequently be leached out in solution. The porous surface created from the dissolved NaCl would increase exposed surface area and available Ag for oxidation [81, 139]. Alternatively, for Zr2k, the problem may stem from Ag^+ elution being stunted by high crystallinity (~47%). Increased mold temperature could compensate for the reduced cooling rate inducing crystal growth in Zr2k.

References

[1] Bozic KJ, Ries MD. The impact of infection after total hip arthroplasty on hospital and surgeon resource utilization. The Journal of bone and joint surgery. 2005;87:1746-51.

[2] Kurtz SM, Lau E, Schmier J, Ong KL, Zhao K, Parvizi J. Infection burden for hip and knee arthroplasty in the United States. J Arthroplasty. 2008;23:984-91.

[3] Kurtz SM, Ong KL, Lau E, Bozic KJ, Berry D, Parvizi J. Prosthetic joint infection risk after TKA in the Medicare population. Clinical orthopaedics and related research. 2010;468:52-6.

[4] Moriarty TF, Schlegel U, Perren S, Richards RG. Infection in fracture fixation: can we influence infection rates through implant design? J Mater Sci Mater Med. 2010;21:1031-5.

[5] Ong KL, Kurtz SM, Lau E, Bozic KJ, Berry DJ, Parvizi J. Prosthetic joint infection risk after total hip arthroplasty in the Medicare population. J Arthroplasty. 2009;24:105-9.

[6] Kubista B, Hartzler RU, Wood CM, Osmon DR, Hanssen AD, Lewallen DG. Reinfection after two-stage revision for periprosthetic infection of total knee arthroplasty. Int Orthop. 2011.

[7] Azzam K, McHale K, Austin M, Purtill JJ, Parvizi J. Outcome of a second two-stage reimplantation for periprosthetic knee infection. Clinical orthopaedics and related research. 2009;467:1706-14.

[8] Hanssen AD, Osmon DR. Evaluation of a staging system for infected hip arthroplasty. Clinical orthopaedics and related research. 2002:16-22.

[9] Darouiche RO. Treatment of infections associated with surgical implants. N Engl J Med. 2004;350:1422-9.

[10] Darouiche RO, Donovan WH, Del Terzo M, Thornby JI, Rudy DC, Hull RA. Pilot trial of bacterial interference for preventing urinary tract infection. Urology. 2001;58:339-44.

[11] Masse A, Bruno A, Bosetti M, Biasibetti A, Cannas M, Gallinaro P. Prevention of pin track infection in external fixation with silver coated pins: clinical and microbiological results. J Biomed Mater Res. 2000;53:600-4.

[12] Parameswaran AD, Roberts CS, Seligson D, Voor M. Pin tract infection with contemporary external fixation: how much of a problem? J Orthop Trauma. 2003;17:503-7.

[13] Collins I, Wilson-MacDonald J, Chami G, Burgoyne W, Vineyakam P, Berendt T, et al. The diagnosis and management of infection following instrumented spinal fusion. Eur Spine J. 2008;17:445-50.

[14] Antoci V, Jr., Adams CS, Parvizi J, Ducheyne P, Shapiro IM, Hickok NJ. Covalently attached vancomycin provides a nanoscale antibacterial surface. Clin Orthop Relat Res. 2007;461:81-7.

[15] Bjerkan G, Witso E, Bergh K. Sonication is superior to scraping for retrieval of bacteria in biofilm on titanium and steel surfaces in vitro. Acta Orthop. 2009;80:245-50.

[16] Lynch AS, Robertson GT. Bacterial and fungal biofilm infections. Annu Rev Med. 2008;59:415-28.

[17] Arciola CR, Campoccia D, Gamberini S, Donati ME, Montanaro L. Presence of fibrinogen-binding adhesin gene in< i> Staphylococcus epidermidis</i> isolates from central venous catheters-associated and orthopaedic implant-associated infections. Biomaterials. 2004;25:4825-9.

[18] Costerton JW, Cheng KJ, Geesey GG, Ladd TI, Nickel JC, Dasgupta M, et al. Bacterial biofilms in nature and disease. Annu Rev Microbiol. 1987;41:435-64.

[19] McAuley JP, Moreau G. Sepsis Etiology, Prophylaxis, and Diagnosis. In: Callaghan JJ, Rosenberg AG, Rubash HE, editors. The Adult Hip. Philadelphia: Lippincot-Raven; 1998. p. 1295-306.

[20] Dunne WM, Jr. Bacterial adhesion: seen any good biofilms lately? Clin Microbiol Rev. 2002;15:155-66.

[21] Parvizi J, Antoci V, Hickok NJ, Shapiro IM. Selfprotective smart orthopedic implants. Expert Review of Medical Devices. 2007;4:55-64.

[22] Jiranek WA, Hanssen AD, Greenwald AS. Antibiotic-loaded bone cement for infection prophylaxis in total joint replacement. Journal of Bone and Joint Surgery-American Volume. 2006;88A:2487-500.

[23] Webb JCJ, Spencer RF. The role of polymethylmethacrylate bone cement in modern orthopaedic surgery. Journal of Bone and Joint Surgery-British Volume. 2007;89B:851-7.

[24] Jaekel DJ, Day JS, Klein GR, Levine H, Parvizi J, Kurtz SM. Do Dynamic Cement-on-Cement Knee Spacers Provide Better Function and Activity During Two-stage Exchange? Clinical Orthopaedics and Related Research. 2012.

[25] Kyomoto M, Moro T, Konno T, Takadama H, Kawaguchi H, Takatori Y, et al. Effects of photo-induced graft polymerization of 2-methacryloyloxyethyl phosphorylcholine on physical properties of cross-linked polyethylene in artificial hip joints. J Mater Sci Mater Med. 2007;18:1809-15.

[26] Kyomoto M, Moro T, Takatori Y, Kawaguchi H, Nakamura K, Ishihara K. Self-initiated surface grafting with poly(2-methacryloyloxyethyl phosphorylcholine) on poly(ether-ether-ketone). Biomaterials. 2010;31:1017-24.

[27] Kyomoto M, Moro T, Takatori Y, Kawaguchi H, Nakamura K, Ishihara K. Self-initiated surface graft polymerization of poly(2-methacryloyloxyethyl phosphorylcholine) on PEEK and carbon fiber reinforced PEEK for orthopaedic and spinal applications. 2010 Orthopeadic Research Society Annual Meeting. New Orleans, LA2010.

[28] Spencer RC. Novel methods for the prevention of infection of intravascular devices. The Journal of hospital infection. 1999;43 Suppl:S127-35.

[29] Pai MP, Pendland SL, Danziger LH. Antimicrobial-coated/bonded and -impregnated intravascular catheters. Ann Pharmacother. 2001;35:1255-63.

[30] Schierholz JM, Yucel N, Rump AF, Beuth J, Pulverer G. Antiinfective and encrustation-inhibiting materials--myth and facts. Int J Antimicrob Agents. 2002;19:511-6.

[31] Rochford E, Jaekel D, Hickok N, Richards R, Moriarty T, Poulsson A. Bacterial Interactions with Polyaryletheretherketone. In: Kurtz SM, editor. PEEK Biomaterials Handbook. New York: Elsevier; 2011. p. 93-117.

[32] Adams CS, Antoci V, Jr., Harrison G, Patal P, Freeman TA, Shapiro IM, et al. Controlled release of vancomycin from thin sol-gel films on implant surfaces successfully controls osteomyelitis. J Orthop Res. 2009;27:701-9.

[33] Kuyyakanond T, Quesnel LB. The mechanism of action of chlorhexidine. FEMS Microbiol Lett. 1992;79:211-5.

[34] Mermel LA. New technologies to prevent intravascular catheter-related bloodstream infections. Emerg Infect Dis. 2001;7:197-9.

[35] Chen W, Liu Y, Courtney HS, Bettenga M, Agrawal CM, Bumgardner JD, et al. In vitro anti-bacterial and biological properties of magnetron co-sputtered silver-containing hydroxyapatite coating. Biomaterials. 2006;27:5512-7.

[36] Damm C, Munsted H, Rosch A. Long-term antimicrobial polyamide 6/silver-nanocomposites. Journal of Materials Science. 2007;42:6067-73.

[37] Kim J, Kwon S, Ostler E. Antimicrobial effect of silver-impregnated cellulose: potential for antimicrobial therapy. J Biol Eng. 2009;3:20.

[38] Perrelli G, Piolatto G. Tentative reference values for gold, silver and platinum: literature data analysis. Sci Total Environ. 1992;120:93-6.

[39] Ruparelia JP, Chatterjee AK, Duttagupta SP, Mukherji S. Strain specificity in antimicrobial activity of silver and copper nanoparticles. Acta Biomater. 2008;4:707-16.

[40] Lansdown AB. A review of the use of silver in wound care: facts and fallacies. Br J Nurs. 2004;13:S6-19.

[41] Lansdown AB, Williams A. How safe is silver in wound care? Journal of wound care. 2004;13:131-6.

[42] Hill JW. Colloidal Silver: Medical Uses, Toxicology and Manufacture: Clear Springs Press; 2009.

[43] Allaker R. The use of nanoparticles to control oral biofilm formation. Journal of dental research. 2010;89:1175-86.

[44] Jung WK, Koo HC, Kim KW, Shin S, Kim SH, Park YH. Antibacterial activity and mechanism of action of the silver ion in Staphylococcus aureus and Escherichia coli. Applied and Environmental Microbiology. 2008;74:2171-8.

[45] Samuel U, Guggenbichler JP. Prevention of catheter-related infections: the potential of a new nano-silver impregnated catheter. International Journal of Antimicrobial Agents. 2004;23:S75-S8.

[46] Furno F, Morley KS, Wong B, Sharp BL, Arnold PL, Howdle SM, et al. Silver nanoparticles and polymeric medical devices: a new approach to prevention of infection? . Journal of Antimicrobial Chemotherapy. 2004;54:1019-24.

[47] Holt KB, Bard AJ. Interaction of silver(I) ions with the respiratory chain of Escherichia coli: an electrochemical and scanning electrochemical microscopy study of the antimicrobial mechanism of micromolar Ag+. Biochemistry. 2005;44:13214-23.

[48] Lok CN, Ho CM, Chen R, He QY, Yu WY, Sun H, et al. Silver nanoparticles: partial oxidation and antibacterial activities. Journal of Biological Inorganic Chemistry. 2007;12:527-34.

[49] Raffi M, Hussain F, Bhatti T, Akhter J, Hameed A, Hasan M. Antibacterial characterization of silver nanoparticles against E. coli ATCC-15224. Journal of Materials Science and Technology. 2008;24:192-6.

[50] Sondi I, Salopek-Sondi B. Silver nanoparticles as antimicrobial agent: a case study on E. coli as a model for Gram-negative bacteria. Journal of colloid and interface science. 2004;275:177-82.

[51] Marambio-Jones C, Hoek EMC. A review of the antibacterial effects of silver nanomaterials and potential implications for human health and the environment. Journal of Nanoparticle Research. 2010;12:1531-51.

[52] Silver S. Bacterial silver resistance: molecular biology and uses and misuses of silver compounds. FEMS microbiology reviews. 2003;27:341-53.

[53] Gupta A, Silver S. Molecular Genetics: Silver as a biocide: Will resistance become a problem? Nature Biotechnology. 1998;16:888.

[54] Stevens KN, Knetsch ML, Sen A, Sambhy V, Koole LH. Disruption and activation of blood platelets in contact with an antimicrobial composite coating consisting of a pyridinium polymer and AgBr nanoparticles. ACS applied materials & interfaces. 2009;1:2049-54.

[55] Schierholz J, Lucas L, Rump A, Pulverer G. Efficacy of silver-coated medical devices. Journal of Hospital Infection. 1998;40:257-62.

[56] Riley DK, Classen DC, Stevens LE, Burke JP. A large randomized clinical trial of a silver-impregnated urinary catheter: lack of efficacy and staphylococcal superinfection. The American journal of medicine. 1995;98:349-56.

[57] Morris N, Stickler D. Encrustation of indwelling urethral catheters by Proteus mirabilis biofilms growing in human urine. Journal of Hospital Infection. 1998;39:227-34.

[58] Djokić S, Burrell R. Behavior of silver in physiological solutions. Journal of the Electrochemical Society. 1998;145:1426.

[59] Brehmer B, Madsen P. Route and prophylaxis of ascending bladder infection in male patients with indwelling catheters. The Journal of urology. 1972;108:719.

[60] Bechert T, Steinrucke P, Guggenbichler JP. A new method for screening anti-infective biomaterials. Nature medicine. 2000;6:1053-6.

[61] Bechert T, Boswald M, Lugauer S, Regenfus A, Greil J, Guggenbichler JP. The Erlanger silver catheter: in vitro results for antimicrobial activity. Infection. 1999;27 Suppl 1:S24-9.

[62] Alt V, Bechert T, Steinrucke P, Wagener M, Seidel P, Dingeldein E, et al. An in vitro assessment of the antibacterial properties and cytotoxicity of nanoparticulate silver bone cement. Biomaterials. 2004;25:4383-91.

[63] Alt V, Bechert T, Steinrucke P, Wagener M, Seidel P, Dingeldein E, et al. In vitro testing of antimicrobial activity of bone cement. Antimicrob Agents Chemother. 2004;48:4084-8.

[64] Devasconcellos P, Bose S, Beyenal H, Bandyopadhyay A, Zirkle LG. Antimicrobial Particulate Silver Coatings on Stainless Steel Implants for Fracture Management. Materials science & engineering C, Materials for biological applications. 2012;32:1112-20.

[65] Zhang W, Yao Y, Sullivan N, Chen Y. Modeling the primary size effects of citrate-coated silver nanoparticles on their ion release kinetics. Environmental science & technology. 2011.

[66] Liu TX, Zhang HF, Han P, Mo ZS, Na H, Cao JK, et al. Effect of heat treatment on the parameters of crystal structure and degree of crystallinity of poly(aryl-ether-ether-ketone). Chemical Journal of Chinese Universities-Chinese. 1996;17:1142-6.

[67] Russell A, Hugo W. 7 Antimicrobial Activity and Action of Silver. Progress in medicinal chemistry. 1994;31:351-70.

[68] Gibbard J. Public Health Aspects of the Treatment of Water and Beverages With Silver*. American Journal of Public Health and the Nations Health. 1937;27:112-9.

[69] Ho CM, Yau SKW, Lok CN, So MH, Che CM. Oxidative dissolution of silver nanoparticles by biologically relevant oxidants: A kinetic and mechanistic study. Chemistry–An Asian Journal. 2010;5:285-93.

[70] Liu J, Hurt RH. Ion release kinetics and particle persistence in aqueous nano-silver colloids. Environmental science & technology. 2010;44:2169-75.

[71] Morones JR, Elechiguerra JL, Camacho A, Holt K, Kouri JB, Ramirez JT, et al. The bactericidal effect of silver nanoparticles. Nanotechnology. 2005;16:2346-53.

[72] Kittler S, Greulich C, Diendorf J, Koller M, Epple M. Toxicity of silver nanoparticles increases during storage because of slow dissolution under release of silver ions. Chemistry of Materials. 2010.

[73] Asghari S, Johari SA, Lee JH, Kim YS, Jeon YB, Choi HJ, et al. Toxicity of various silver nanoparticles compared to silver ions in Daphnia magna. Journal of nanobiotechnology. 2012;10:14.

[74] Hardes J, Ahrens H, Gebert C, Streitbuerger A, Buerger H, Erren M, et al. Lack of toxicological side-effects in silver-coated megaprostheses in humans. Biomaterials. 2007;28:2869-75.

[75] Gray JE, Norton PR, Alnouno R, Marolda CL, Valvano MA, Griffiths K. Biological efficacy of electroless-deposited silver on plasma activated polyurethane. Biomaterials. 2003;24:2759-65.

[76] Kumar R, Munstedt H. Silver ion release from antimicrobial polyamide/silver composites. Biomaterials. 2005;26:2081-8.

[77] Chivers RA, Moore DR. The Effect of Molecular-Weight and Crystallinity on the Mechanical-Properties of Injection-Molded Poly(Aryl-Ether-Ether-Ketone) Resin. Polymer. 1994;35:110-6.

[78] Ostberg GMK, Seferis JC. Annealing effects on the crystallinity of polyetheretherketone (PEEK) and its carbon fiber composites. Journal of Applied Polymer Science. 1986;33:29-33.

[79] Skinner HB. Composite technology for total hip arthroplasty. Clin Orthop Relat Res. 1988:224-36.

[80] Kurtz SM, Devine JN. PEEK biomaterials in trauma, orthopedic, and spinal implants. Biomaterials. 2007;28:4845-69.

[81] Converse GL, Conrad TL, Merrill CH, Roeder RK. Hydroxyapatite whisker-reinforced polyetherketoneketone bone ingrowth scaffolds. Acta Biomater. 2010;6:856-63.

[82] Converse GL, Yue WM, Roeder RK. Processing and tensile properties of hydroxyapatite-whisker-reinforced polyetheretherketone. Biomaterials. 2007;28:927-35.

[83] Joyce TJ. Prediction of lubrication regimes in two-piece metacarpophalangeal prostheses. Medical engineering & physics. 2007;29:87-92.

[84] Cebe P, Lowry L, Chung SY, Yavrouian A, Gupta A. Wide-Angle X-Ray-Scattering Study of Heat-Treated Peek and Peek Composite. Journal of Applied Polymer Science. 1987;34:2273-83.

[85] Chalmers JM, Everall NJ, Hewitson K, Chesters MA, Pearson M, Grady A, et al. Fourier transform infrared microscopy: some advances in techniques for characterisation and structure-property elucidations of industrial material. Analyst. 1998;123:579-86.

[86] Chalmers JM, Gaskin WF, Mackenzie MW. Crystallinity in Poly(Aryl-Ether-Ketone) Plaques Studied by Multiple Internal-Reflection Spectroscopy. Polymer Bulletin. 1984;11:433-5.

[87] Jonas A, Legras R, Issi JP. Differential Scanning Calorimetry and Infrared Crystallinity Determinations of Poly(Aryl Ether Ether Ketone). Polymer. 1991;32:3364-70.

[88] Blundell DJ, Osborn BN. The Morphology of Poly(Aryl-Ether-Ether-Ketone). Polymer. 1983;24:953-8.

[89] Ostberg GMK, Seferis JC. Annealing Effects on the Crystallinity of Polyetheretherketone (Peek) and Its Carbon-Fiber Composite. Journal of Applied Polymer Science. 1987;33:29-39.

[90] Blundell DJ, Chalmers JM, Mackenzie MW, Gaskin WF. Crystalline Morphology of the Matrix of Peek-Carbon Fiber Aromatic Polymer Composites .1. Assessment of Crystallinity. Sampe Quarterly-Society for the Advancement of Material and Process Engineering. 1985;16:22-30.

[91] Fuziwara S, Ogawa K, Aso D, Yoshizawa D, Takata S, Denda M. Barium sulphate with a negative zeta potential accelerates skin permeability barrier recovery and prevents epidermal hyperplasia induced by barrier disruption. Br J Dermatol. 2004;151:557-64.

[92] Arzak A, Eguiazabal JI, Nazabal J. Effect of Annealing on the Properties of Poly(Ether Ether Ketone). Polymer Engineering and Science. 1991;31:586-91.

[93] Cebe P. Annealing Study of Poly(Etheretherketone). Journal of Materials Science. 1988;23:3721-31.

[94] Giddings VL, Kurtz SM, Jewett CW, Foulds JR, Edidin AA. A small punch test technique for characterizing the elastic modulus and fracture behavior of PMMA bone cement used in total joint replacement. Biomaterials. 2001;22:1875-81.

[95] Kurtz SM, Foulds JR, Jewett CW, Srivastav S, Edidin AA. Validation of a small punch testing technique to characterize the mechanical behaviour of ultra-high-molecular-weight polyethylene. Biomaterials. 1997;18:1659-63.

[96] Foulds JR, Woytowitz PJ, Parnell TK, Jewett CW. Fracture-Toughness by Small Punch Testing. Journal of Testing and Evaluation. 1995;23:3-10.

[97] Williams DF, McNamara A, Turner RM. Potential of polyetheretherketone (PEEK) and carbon-fibre-reinforced PEEK in medical applications. J Mat Sci Letters. 1987;6:188-90.

[98] Wilke HJ, Drumm J, Haeussler K, Mack C, Steudel WI, Kettler A. Biomechanical effect of different lumbar interspinous implants on flexibility and intradiscal pressure. European Spine Journal. 2008;17:1049-56.

[99] Jaekel DJ, Medel FJ, Kurtz SM. Validation of Crystallinity Measurements of Medical Grade PEEK Using Specular Reflectance FTIR-microscopy. Society of Plastics Engineers Annual Technical Conference. Chicago: Society of Plastics Engineers; 2009.

[100] ASTMF2778-09. Standard Test Method for Measurement of Percent Crystallinity of Polyetheretherketone (PEEK) Polymers by Means of Specular Reflectance Fourier Transform Infrared Spectroscopy (R-FTIR). West Conshocken, PA American Society for Testing and Materials; 2009.

[101] ASTMF2183-02. Standard test method for small punch testing of ultra-high molecular weight polyethylene used in surgical implants. West Conshocken, PA American Society for Testing and Materials; 2008.

[102] Edidin AA, Kurtz SM. Influence of mechanical behavior on the wear of 4 clinically relevant polymeric biomaterials in a hip simulator. J Arthroplasty. 2000;15:321-31.

[103] Boinard E, Pethrick R, McFarlane C. The influence of thermal history on the dynamic mechanical and dielectric studies of polyetheretherketone exposed to water and brine. Polymer. 2000;41:1063-76.

[104] Stober EJ, Seferis JC, Keenan JD. Characterization and exposure of polyetheretherketone (PEEK) to fluid environments. Polymer. 1984;25:1845-52.

[105] Invibio. PEEK-OPTIMA Image Contrast Grades. In: Invibio L, editor. Thornton Cleveleys, UK: Invibio, Ltd.; 2008.

[106] Abu Bakar MS, Cheng MHW, Tang SM, Yu SC, Liao K, Tan CT, et al. Tensile properties, tension-tension fatigue and biological response of

polyetheretherketone -hydroxyapatite composites for load-bearing orthopedic implants. Biomaterials. 2003;24:2245-50.

[107] Abu Bakar MS, Cheang P, Khor KA. Tensile properties and microstructural analysis of spheroid hydroxyapatite-poly (etheretherketone) biocomposites. Materials Science and Engineering. 2003;A345:55-63.

[108] Joseph K, Thomast S. Effect of chemical treatment on the tensile properties of short sisal fibre-reinforced polyethylene composites. Polymer. 1996;37:5139-49.

[109] Kim IY, Sugino A, Kikuta K, Ohtsuki C, Cho SB. Bioactive composites consisting of PEEK and calcium silicate powders. J Biomater Appl. 2009;24:105-18.

[110] Chen X, Schluesener HJ. Nanosilver: a nanoproduct in medical application. Toxicology letters. 2008;176:1-12.

[111] Atiyeh BS, Costagliola M, Hayek SN, Dibo SA. Effect of silver on burn wound infection control and healing: review of the literature. Burns : journal of the International Society for Burn Injuries. 2007;33:139-48.

[112] Martinez-Castanon G, Nino-Martinez N, Martinez-Gutierrez F, Martinez-Mendoza J, Ruiz F. Synthesis and antibacterial activity of silver nanoparticles with different sizes. Journal of Nanoparticle Research. 2008;10:1343-8.

[113] Hoskins JS, Karanfil T, Serkiz SM. Removal and sequestration of iodide using silver-impregnated activated carbon. Environ Sci Technol. 2002;36:784-9.

[114] Meulenkamp EA. Size dependence of the dissolution of ZnO nanoparticles. The Journal of Physical Chemistry B. 1998;102:7764-9.

[115] Measurement of antibacterial activity on plastics surfaces. Plastics. Switzerland: International Standard; 2007.

[116] Grayson MA, Wolf CJ. The solubility and diffusion of water in poly (aryl-ether-ether-ketone)(PEEK). Journal of Polymer Science Part B: Polymer Physics. 1987;25:31-41.

[117] Comyn J. Polymer permeability: Springer; 1985.

[118] Li X, Jasti BR. Design of controlled release drug delivery systems: McGraw-Hill Professional; 2006.

[119] Slifkin L. The physics of lattice defects in silver halides. Crystal Lattice Defects and Amorphous Materials. 1989;18:81-96.

[120] Boinard E, Pethrick RA, McFarlane CJ. The influence of thermal history on the dynamic mechanical and dielectric studies of polyetheretherketone exposed to water and brine. Polymer. 2000;41:1063-76.

[121] de Candia F, Michele A, Renzulli A. Molecular motions in polyetheretherketone (PEEK): NMR analysis of the low-temperature relaxation mechanism. Journal of Macromolecular Science, Part B, . 1994;33:307-16.

[122] Wolf CJ, Bornmann JA, Grayson MA. The absorption of organic liquids in poly (aryl-ether-ether-ketone)[PEEK]. Journal of Polymer Science Part B: Polymer Physics. 1991;29:1533-9.

[123] Law H, Fleming R, Gilmore M, McCarthy I, Hughes S. < i> In vitro</i> measurement and computer modelling of the diffusion of antibiotic in bone cement. Journal of biomedical engineering. 1986;8:149-55.

[124] Damm C, Munstedt H. Kinetic aspects of the silver ion release from antimicrobial polyamide/silver nanocomposites. Applied Physics A: Material Science and Processing. 2008;91:479-86.

[125] Kumar R, Munstedt H. Polyamide/silver antimicrobials: effect of crystallinity on the silver ion release. Polymer International. 2005;54:1180-6.

[126] Radheshkumar C, Munstedt H. Antimicrobial polymers from polypropylene/silver composites—Ag+ release measured by anode stripping voltammetry. Reactive & Functional Polymers. 2006;66:780-8.

[127] Antoci V, Jr., Adams CS, Hickok NJ, Shapiro IM, Parvizi J. Vancomycin bound to Ti rods reduces periprosthetic infection: preliminary study. Clin Orthop Relat Res. 2007;461:88-95.

[128] Donlan RM, Costerton JW. Biofilms: survival mechanisms of clinically relevant microorganisms. Clin Microbiol Rev. 2002;15:167-93.

[129] Russel AD, Chopra I. Understanding antibacterial action and resistance. 2nd ed. London: Ellis Horwood Limited; 1996.

[130] Feng QL, Wu J, Chen GQ, Cui FZ, Kim TN, Kim JO. A mechanistic study of the antibacterial effect of silver ions on Escherichia coli and Staphylococcus aureus. Journal of Biomedical Materials Research. 2000;52:662-8.

[131] Jaekel DJ, Macdonald DW, Kurtz SM. Characterization of PEEK biomaterials using the small punch test. Journal of the mechanical behavior of biomedical materials. 2011;4:1275-82.

[132] DeArmitt C, Hancock M. Filled Thermoplastics. In: Rothon RN, editor. Particulate-Filled Polymer Composites. 2 ed. Shawbury, UK: Rapra Technology Limited; 2003.

[133] Throne JL. Processing Thermoplastic Composites. In: Peters ST, editor. Handbook of Composites. 2 ed. London, UK: Chapman & Hill; 1998.

[134] Barth E, Myrvik QM, Wagner W, Gristina AG. In vitro and in vivo comparative colonization of Staphylococcus aureus and Staphylococcus epidermidis on orthopaedic implant materials. Biomaterials. 1989;10:325-8.

[135] Japanese Industrial Standard/Antimicrobial products—Test for antimicrobial activity and efficacy. Japanese standard association. Tokyo, Japan: Akasaka Minato-ku; 2000.

[136] Antoci V, Jr., Adams CS, Parvizi J, Davidson HM, Composto RJ, Freeman TA, et al. The inhibition of Staphylococcus epidermidis biofilm formation by vancomycin-modified titanium alloy and implications for the treatment of periprosthetic infection. Biomaterials. 2008;29:4684-90.

[137] Naffakh M, López V, Zamora F, Gómez MA. Novel Melt-Processable Nanocomposites Based on Isotactic Polypropylene and Carbon Nitride: Morphology, Crystallization, and Dynamic Mechanical Properties. Soft Materials. 2010;8:407-25.

[138] Velisaris CN, Seferis JC. Heat transfer effects on the processing-structure relationships of polyetheretherketone (PEEK) based composites. Polym Eng Sci. 1988;28:583-91.

[139] Converse GL, Conrad TL, Roeder RK. Mechanical properties of hydroxyapatite whisker reinforced polyetherketoneketone composite scaffolds. J Mech Behav Biomed Mater. 2009;2:627-35.

[140] Parvizi J, Wickstrom E, Zeiger AR, Adams CS, Shapiro IM, Purtill JJ, et al. Frank Stinchfield Award. Titanium surface with biologic activity against infection. Clin Orthop Relat Res. 2004:33-8.

[141] Edupuganti OP, Antoci V, Jr., King SB, Jose B, Adams CS, Parvizi J, et al. Covalent bonding of vancomycin to Ti6Al4V alloy pins provides long-term inhibition of Staphylococcus aureus colonization. Bioorganic & medicinal chemistry letters. 2007;17:2692-6.

[142] Ketonis C, Adams CS, Barr S, Aiyer A, Shapiro IM, Parvizi J, et al. Antibiotic modification of native grafts: improving upon nature's scaffolds. Tissue Eng Part A. 2010;16:2041-9.

[143] Noiset O, Schneider YJ, MarchandBrynaert J. Surface modification of poly(aryl ether ether ketone) (PEEK) film by covalent coupling of amines and amino acids through a spacer arm. Journal of Polymer Science Part a-Polymer Chemistry. 1997;35:3779-90.

[144] Briem D, Strametz S, Schroder K, Meenen NM, Lehmann W, Linhart W, et al. Response of primary fibroblasts and osteoblasts to plasma treated polyetheretherketone (PEEK) surfaces. J Mater Sci Mater Med. 2005;16:671-7.

[145] Schroder K, Meyer-Plath A, Keller D, Besch, W., Babucke G, Ohl A. Plasma-induced surface functionalization of polymeric biomaterials in ammonia plasma. Contns Plasma Phys. 2001;41:562-72.

Appendix

A: Plasma Deposition of Amines on PEEK for Antibiotic Surface Tethering

Introduction

A potential drawback to antibiotic-releasing or antimicrobial coatings is damage and coating removal during implantation. Surgeries, as in the orthopaedic field, apply high forces and surface friction against rigid boney surfaces. To alleviate some of these issues, antibiotics, notably vancomycin (VAN), as well as other antimicrobials, have been covalently bonded to the surface of titanium, titanium alloys, and bone allograft [14, 127]. [14, 127]. Importantly, because VAN reversibly inhibits peptidoglycan synthesis at the bacterial cell membrane, the surface can withstand multiple challenges to result in long-term antibiotic activity [136, 140]. The stable VAN functionalized surface eliminates toxicity issues associated with other antibiotic coatings because only small amounts of antibiotic are immobilized on the surfaces. Furthermore, the covalent nature of the bond ensures that removal of the antibiotic does not occur without sufficient mechanical force, and thus the risk of exposure of host tissue to sub-therapeutic doses is greatly lowered. In both in vitro and in vivo studies, VAN bonded surfaces have prevented or substantially inhibited the growth of *Staphylococcus epidermidis* and *aureus* [14, 32, 127, 136, 140-142] The first step in bonding VAN to bone or titanium surfaces is functionalizing amines (NH_2) groups on the surface of the material. The amines are then linked to two Fmoc-aminoethoxyethoxyacetate linkers for permanent tethering to VAN. NH_2 has only

been stably established on PEEK when surfaces were exposed to ammonia gas plasma in high vacuums or multi-day incubation in hazard chemical such as toluene, acetone, and dioxane. In an alternative approach, we attempted to establish a novel plasma technique to aminate PEEK substrates using a nitrogen/hydrogen gas mixture in atmospheric pressure. This method will reduce cost, lower manufacturing time, and increase safety while establishing a long-term antibacterial surface for PEEK biomaterials.

Methods and Materials

Materials and Plasma Treatment

For these studies, all samples tested were injection-molded, unfilled PEEK (Optima LT1, Invibio, Ltd, U.K). Prior to modification, PEEK samples were washed thoroughly in acetone (3x) and then rinse in deionized (DI) water (5x). To generate amine (NH_2) groups on PEEK surfaces, specimens were exposed to an N_2/H_2 plasma mixture from a custom designed plasmtron/gliding arc reactor at atmospheric pressure. Pure N_2 and a H_2/He (40%/60%) mixture were first combined in a mixing chamber prior to entering the plasmatron. Gas ratio was controlled by flow rate where N_2 flow rate was constant at 10 l/min, and H_2 was set to 0.01, 0.1, 0.7, or 0.8 l/min. Flow rates higher than this were not attempted because of safety concerns. Samples were placed 1 inch from the plasmatron source and exposed from 10 to 50 minutes at a reactor power current of 100,

120, 140, or 500 mA. Samples were visually evaluated for any sign of melting or annealing.

Amine Detection (Ninhydrin Assay)

Surface concentration of NH_2 was measured by boiling plasma -reated samples in a solution of 1M sodium citrate (pH5, 100 µl), 3.5 M $SnCl_2$ (100 µl), DI H_2O (800 µl), and 4% Ninhydrin in EtOH (1 ml) for 15 minutes. NH_2 was quantified by measuring the absorbance change in solution at λ = 570nm and converting to concentration based on the Beer-Lambert law:

$c = \frac{A}{\varepsilon * l}$;

where c is concentration in mol/l, A is the absorbance value, *l* is the cuvette length, and ε is the absorbance coefficient ($1.5x10^4$ l/mol*cm). Untreated PEEK samples served as controls.

Covalently Bonding VAN and VAN Detection Assay

Once amine deposition was established, VAN was coupled to the surface via two membrane-soluble linkers. Specifically, PEEK-NH_2 was coupled sequentially with two Fmoc-aminoethoxyethoxyacetate linkers and vancomycin in the presence of O-(7-azabenzo-triazole-1-yl)-1,1,3,3-tetramethyluronium hexafluorophosphate and in N,N-dimethylformamide [14, 136] (Figure A1). Antibiotic distribution was determined by an ELISA assay using a commercially available anti-VAN antibody, followed by incubation with a secondary antibody

bearing horseradish peroxidase. After 24 hr incubation in the assay, levels of VAN were determined by absorbance at λ =405nm. Bone that had previously and successfully had VAN grafted to the surface was used as a positive control.

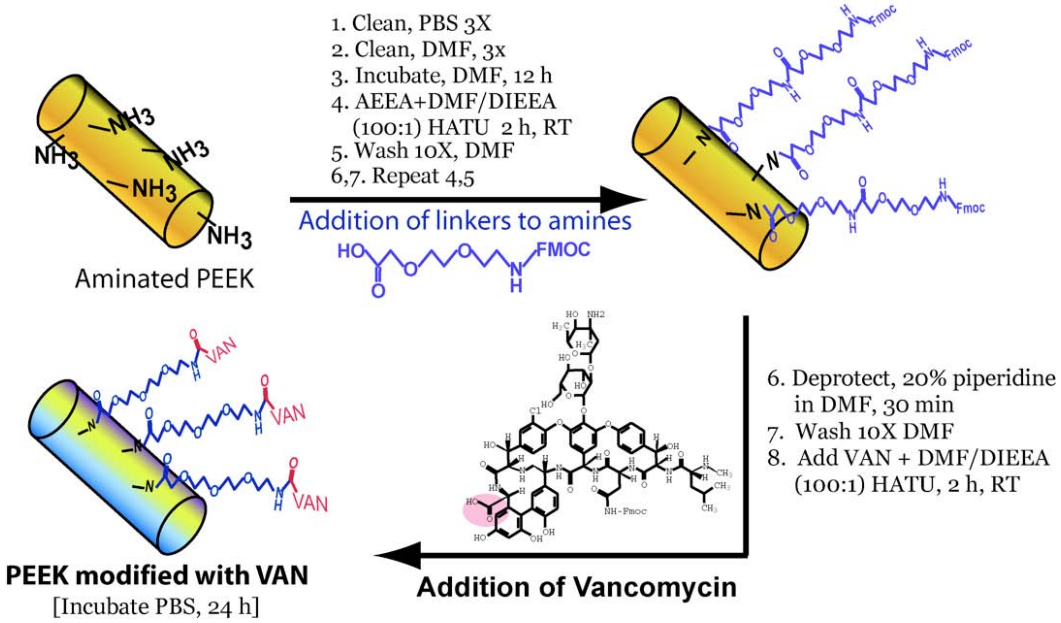

Figure A-0-1: Covalent bonding process of VAN onto PEEK.

Results

Despite exposure time or current, H_2/He flow rates <0.7L/min did not produce detectable levels of NH_2 deposition. Once the H_2/He flow rate was increased to between 0.7-0.8L/min, detectable levels of amines were observed and increased with exposure time and current (Table A1, Figure A2). VAN was successfully covalently bonded to PEEK samples exposed to N_2/H_2 plasma for 50 minutes with a current of 140 mA applied (Figure A3). However, if the current was increased to as high as 500 mA, melting was observed on PEEK surfaces.

VAN levels were much greater than controls, but less than previous bonded VAN-bone surfaces.

Table A-0-1: Deposited amine levels on PEEK substrates based on exposure time and current applied to plasma reactor.

H_2/He Flow Rate	Power (mA)	Exposure Time (min)	NH_2 (Molecules/nm^2)
0.7 L/min	120	25	-0.27
		50	6.40
	140	50	12.53
0.8 L/min	140	50	9.95

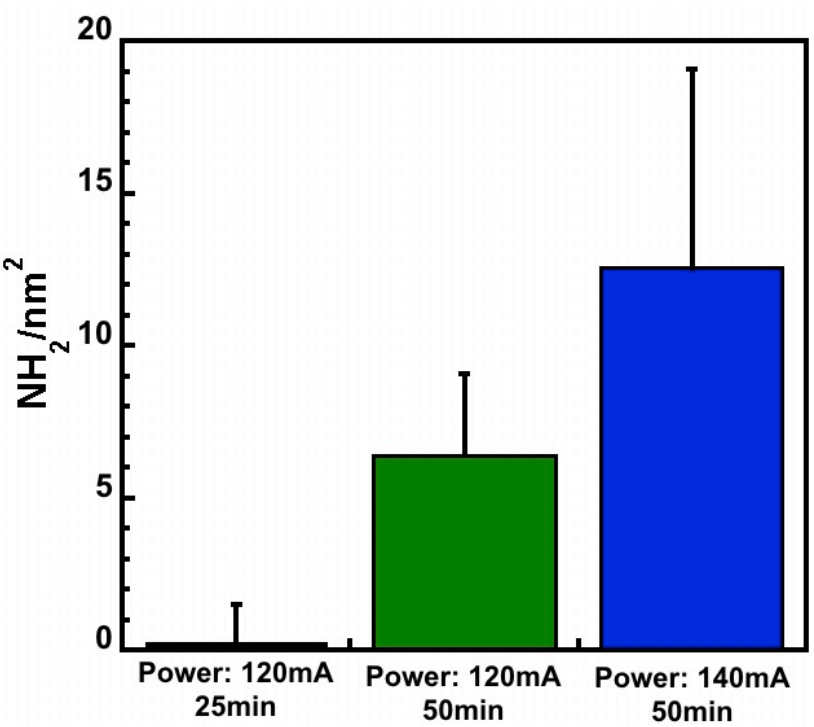

Figure A-0-2: Amine surface deposition on PEEK substrates.

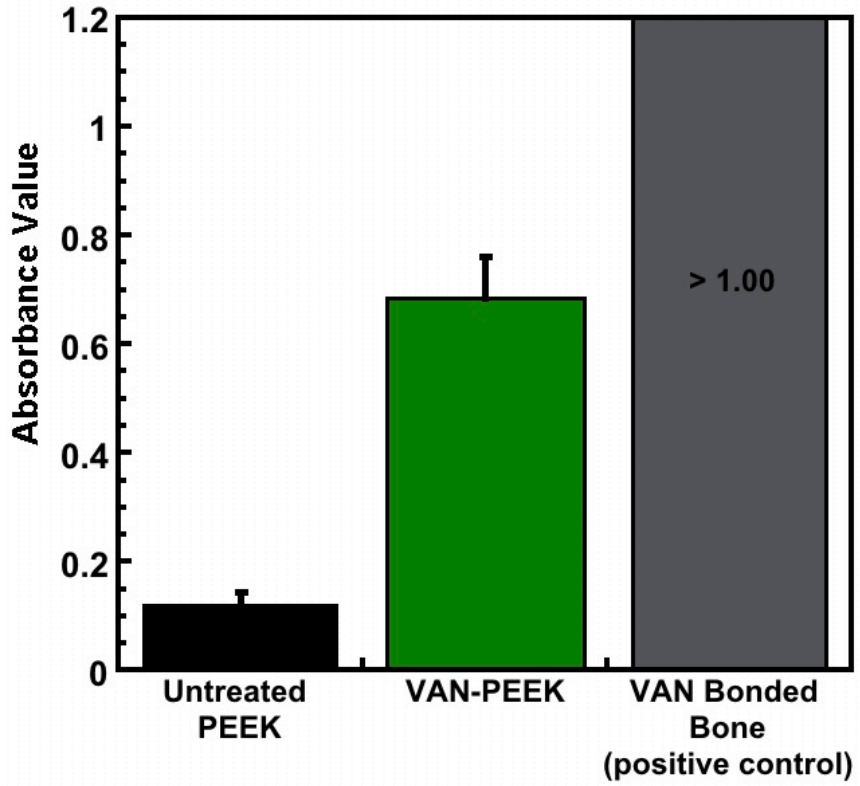

Figure A-0-3: VAN levels on N_2/H_2 plasma treated surface as compared to controls.

Discussion and Conclusion

A gas mixture of N_2 and H_2 was tested for its ability to aminate PEEK, and in the process reduce the difficulty and increase the safety of the amination process as compared to other methods in the production of NH_2. Previously, NH_2 had not been established on PEEK surfaces without the use of high vacuum plasma with ammonia gas or a multi-day incubation process with toluene and dioxanne [143-145]. The results show that NH_2 can be established on a polymer surface at sufficient levels when combining these two commercially available and common gases. VAN-PEEK surface abundance was lower than that measured for the positive control bone surfaces, however, the VAN-bone was more porous

structurally and hence had more sites for potential VAN bonding. This method has been highly successful in creating a long-term antibacterial surface for titanium and bone, but has never been transfer to a polymer material. The initial work detailed in this study established a baseline for creating antibiotic-bonded-PEEK materials with a rapid and industrially relevant plasma treatment method. Further work has to be done to optimize the plasma treatment process for increased amounts of PEEK and to maximize NH_2 surface deposition. This will provide suitable quantities of materials for bacterial adhesion testing and future biocompatibility trials.

B: Additional Figures

1. Ag-Agar MIC Tests with *S. Aureus* ATCC 25923

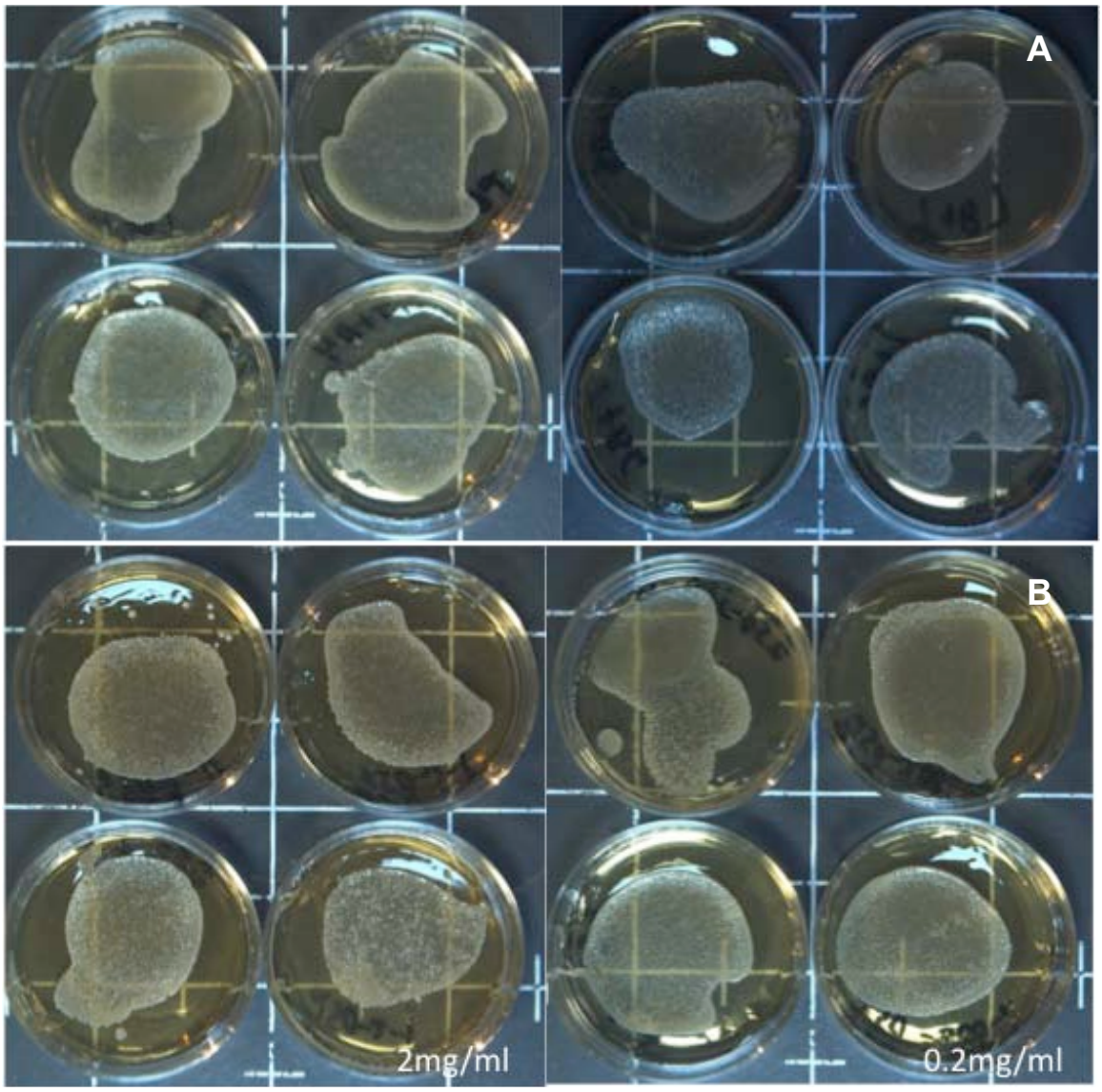

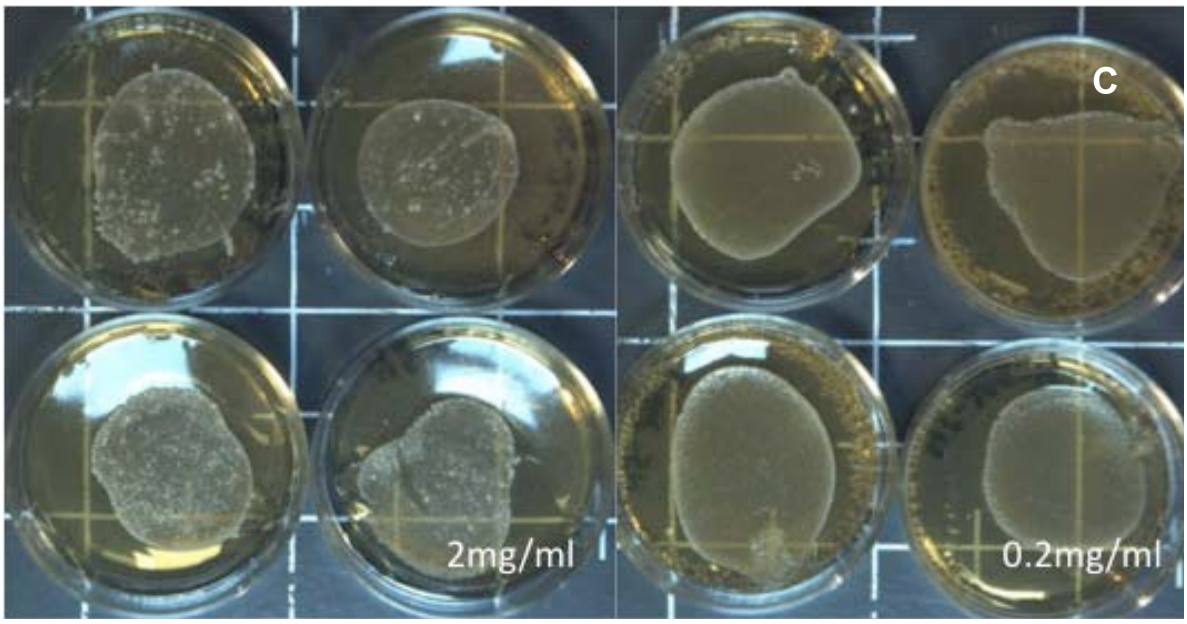
C
2mg/ml
0.2mg/ml

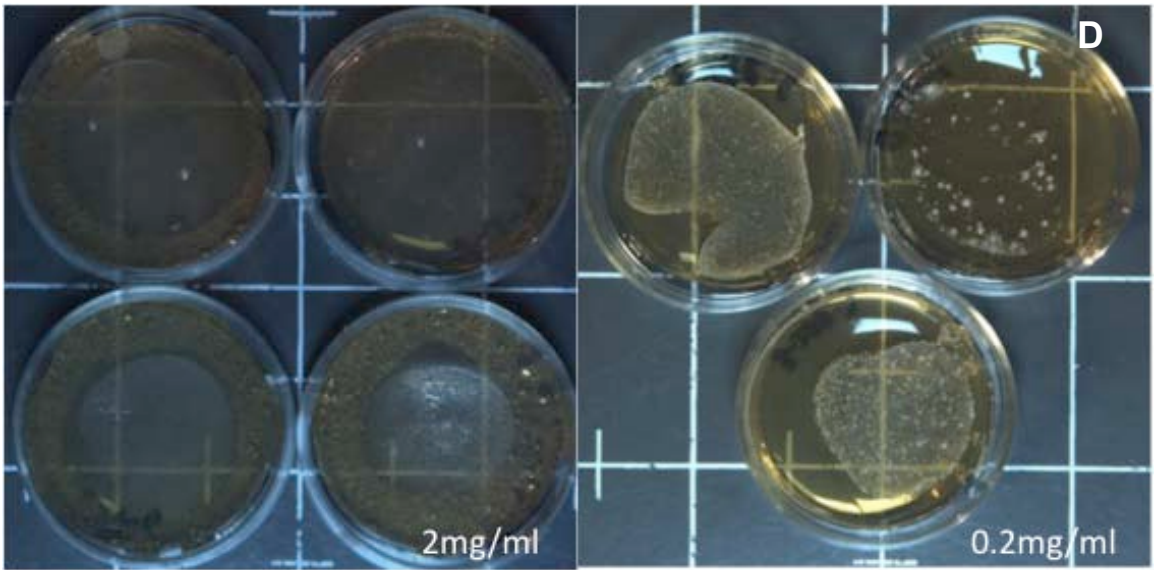
D
2mg/ml
0.2mg/ml

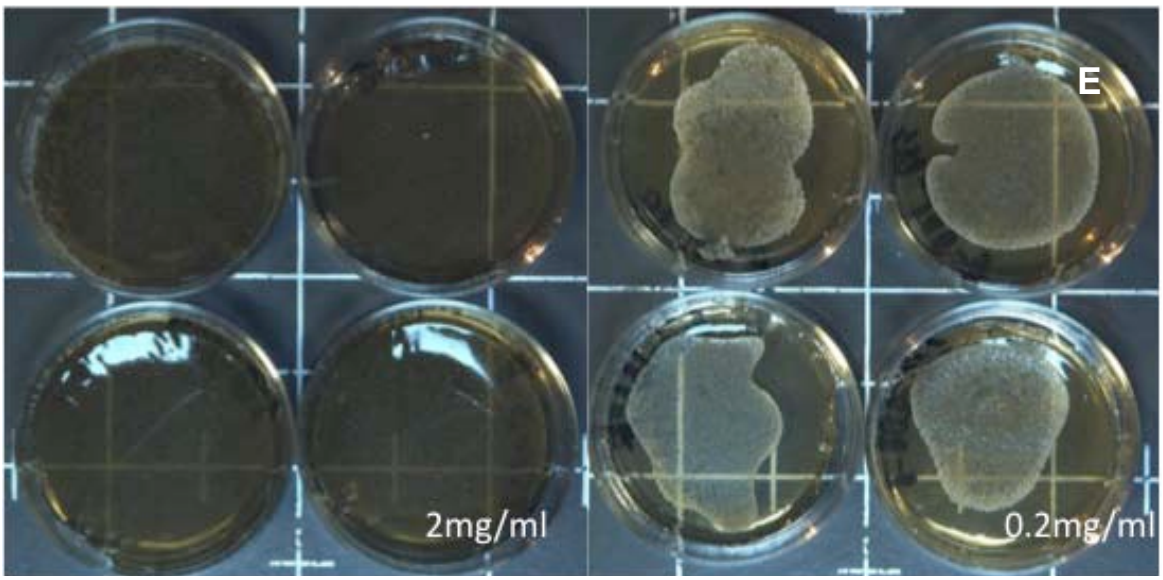
E
2mg/ml
0.2mg/ml

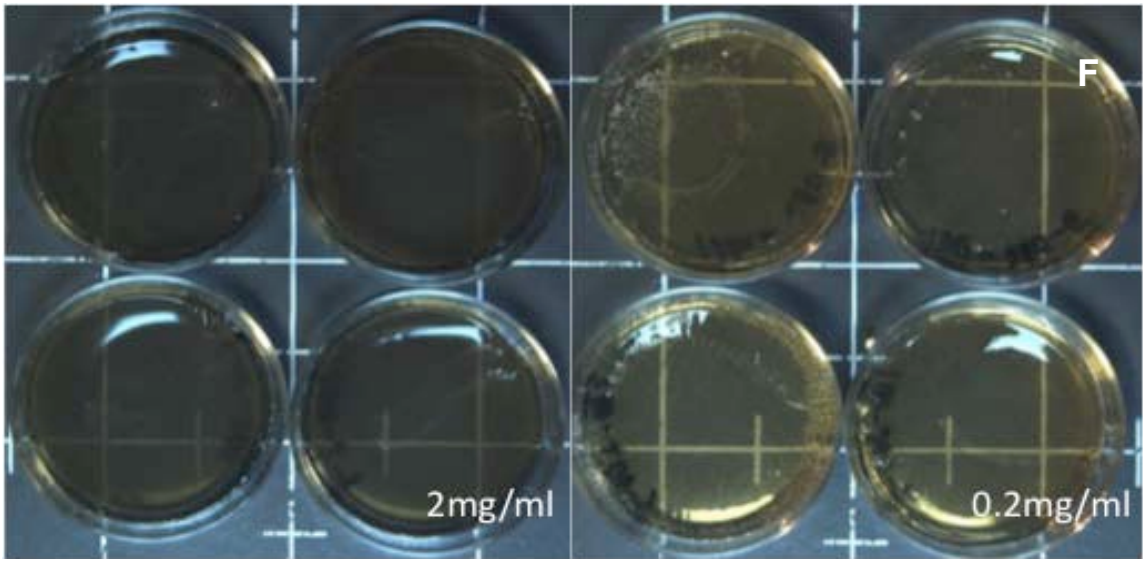
F
2mg/ml
0.2mg/ml

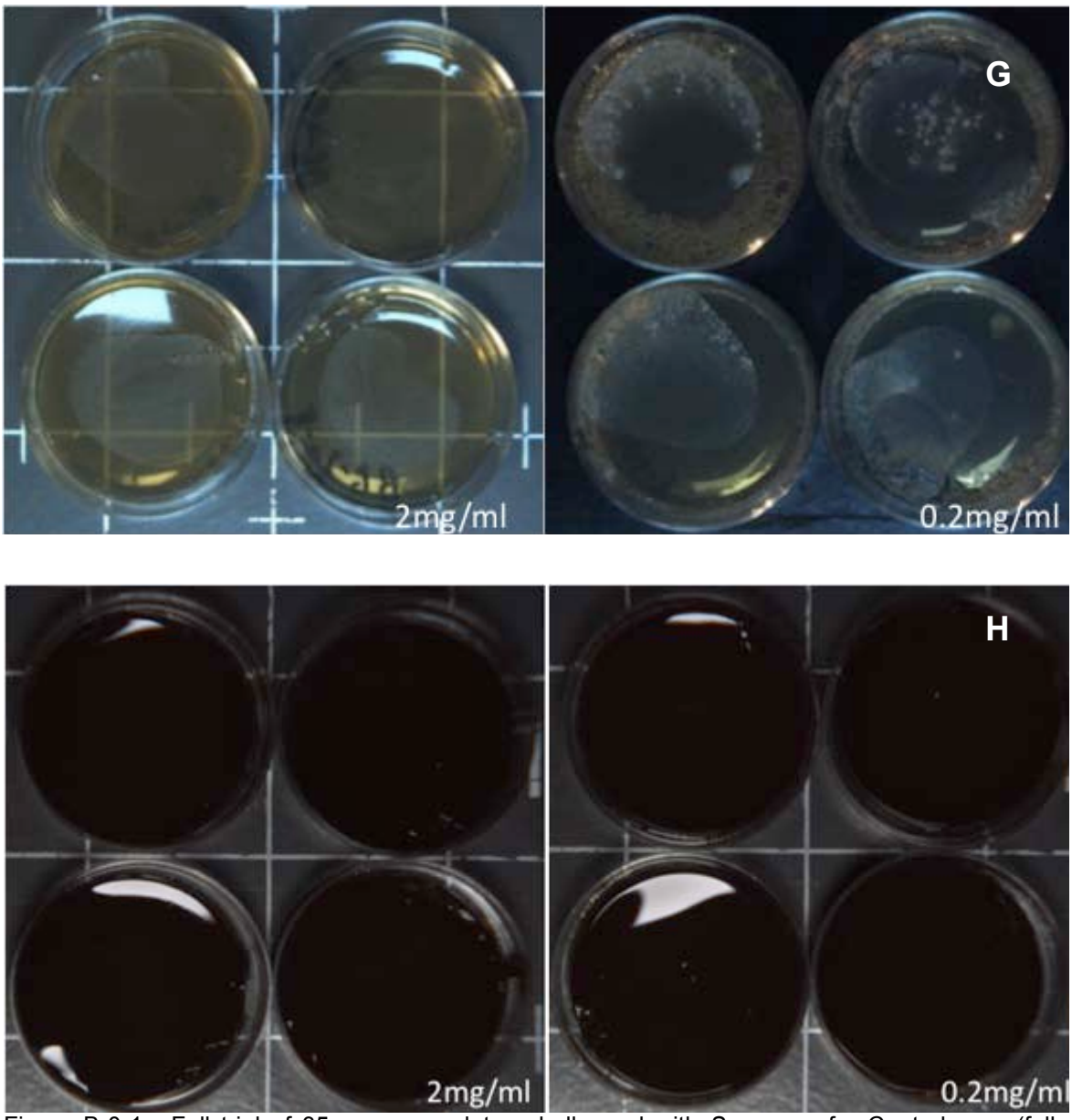

Figure B-0-1: Full trial of 35 mm agar plates challenged with *S. aureus* for Control agar (full growth) (A), 250 µm diameter (B), 45 µm diameter (C), 5-8 µm diameter (D), 150 nm diameter (E), 100 nm diameter (F), BioGate HyMedic 4000 (G), and Zr2k particle (H).

2. Ag-Agar MIC Tests with *E. Coli* ATCC 25925

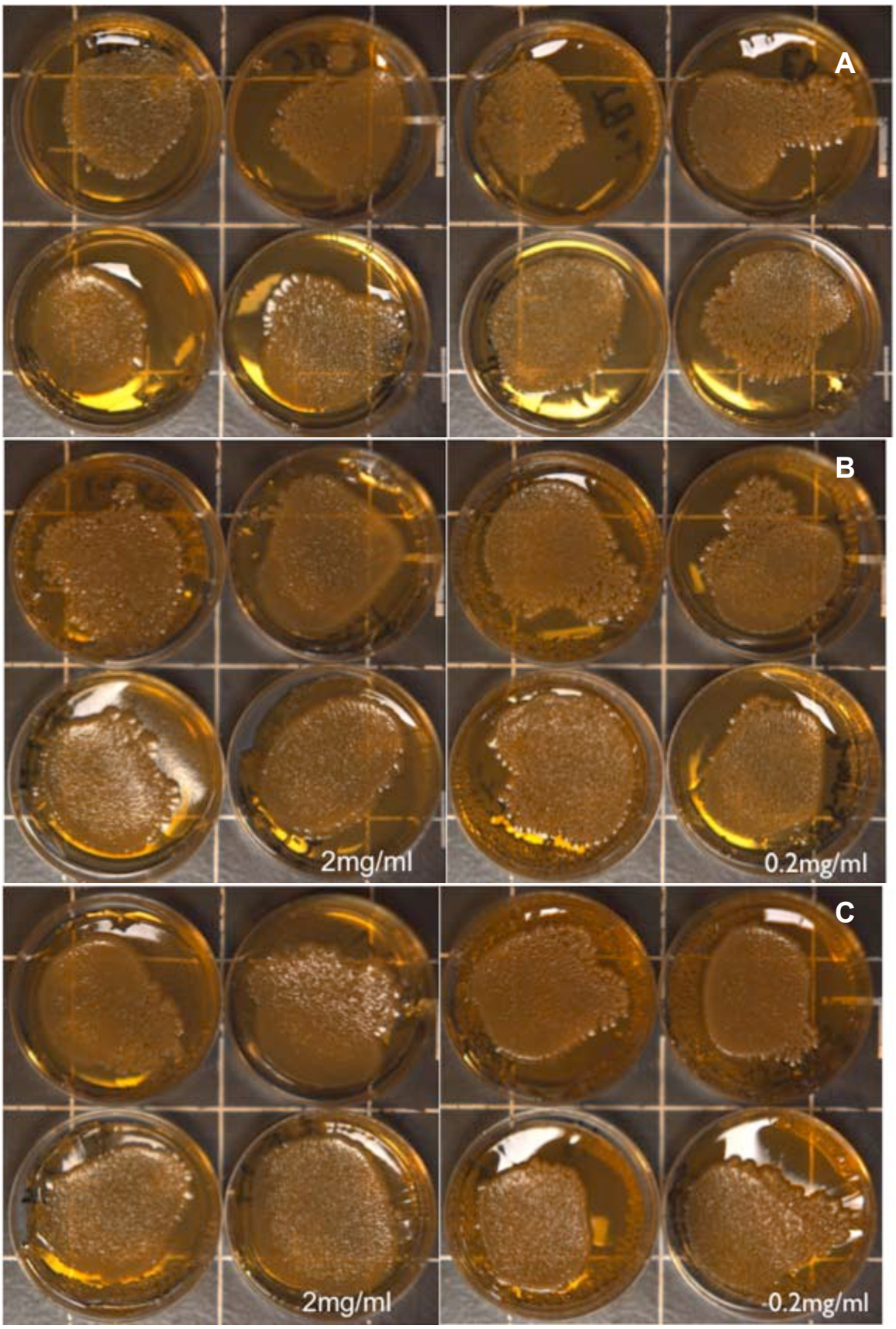
A
B
2mg/ml
0.2mg/ml
C
2mg/ml
0.2mg/ml

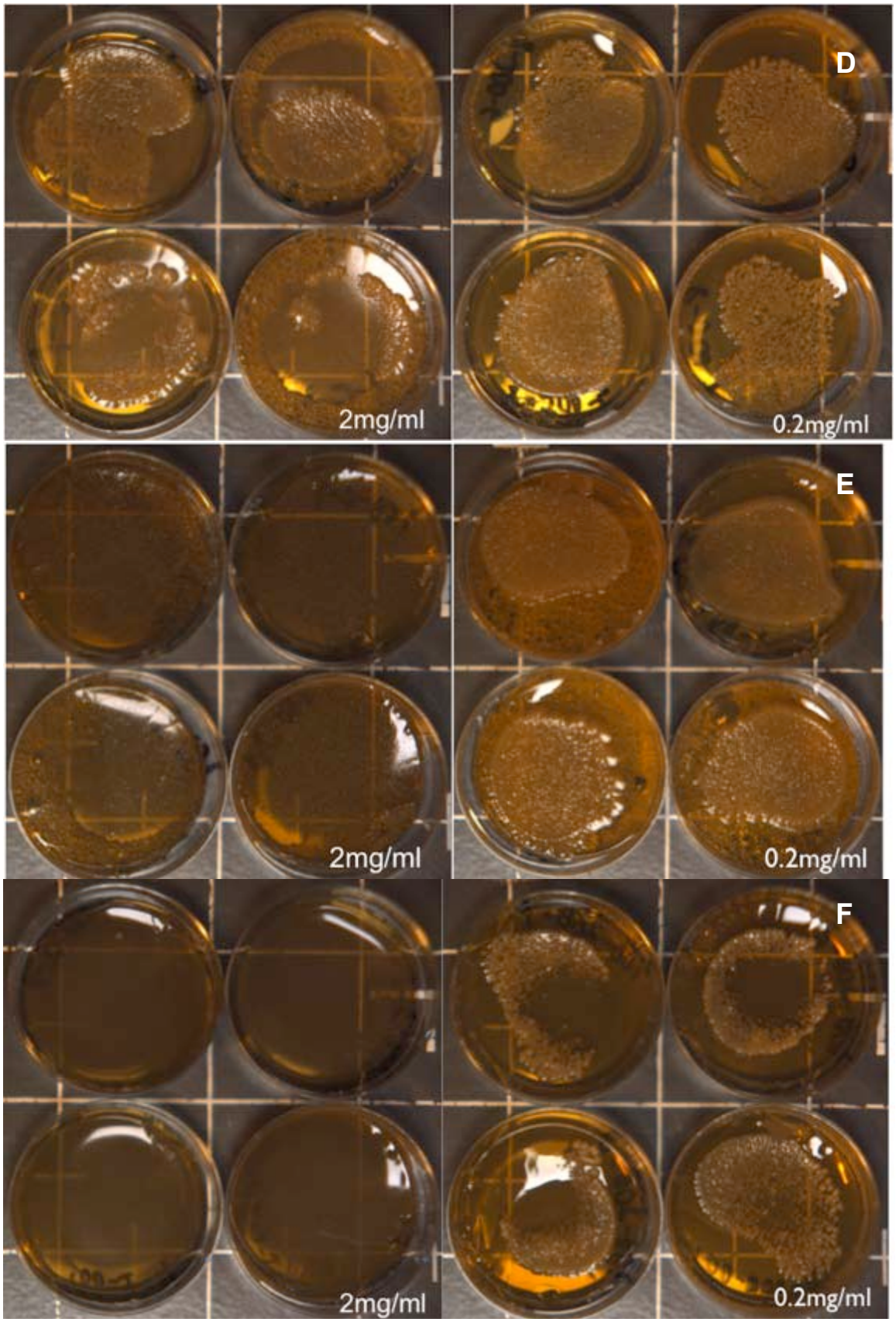
D
2mg/ml
0.2mg/ml
E
2mg/ml
0.2mg/ml
F
2mg/ml
0.2mg/ml

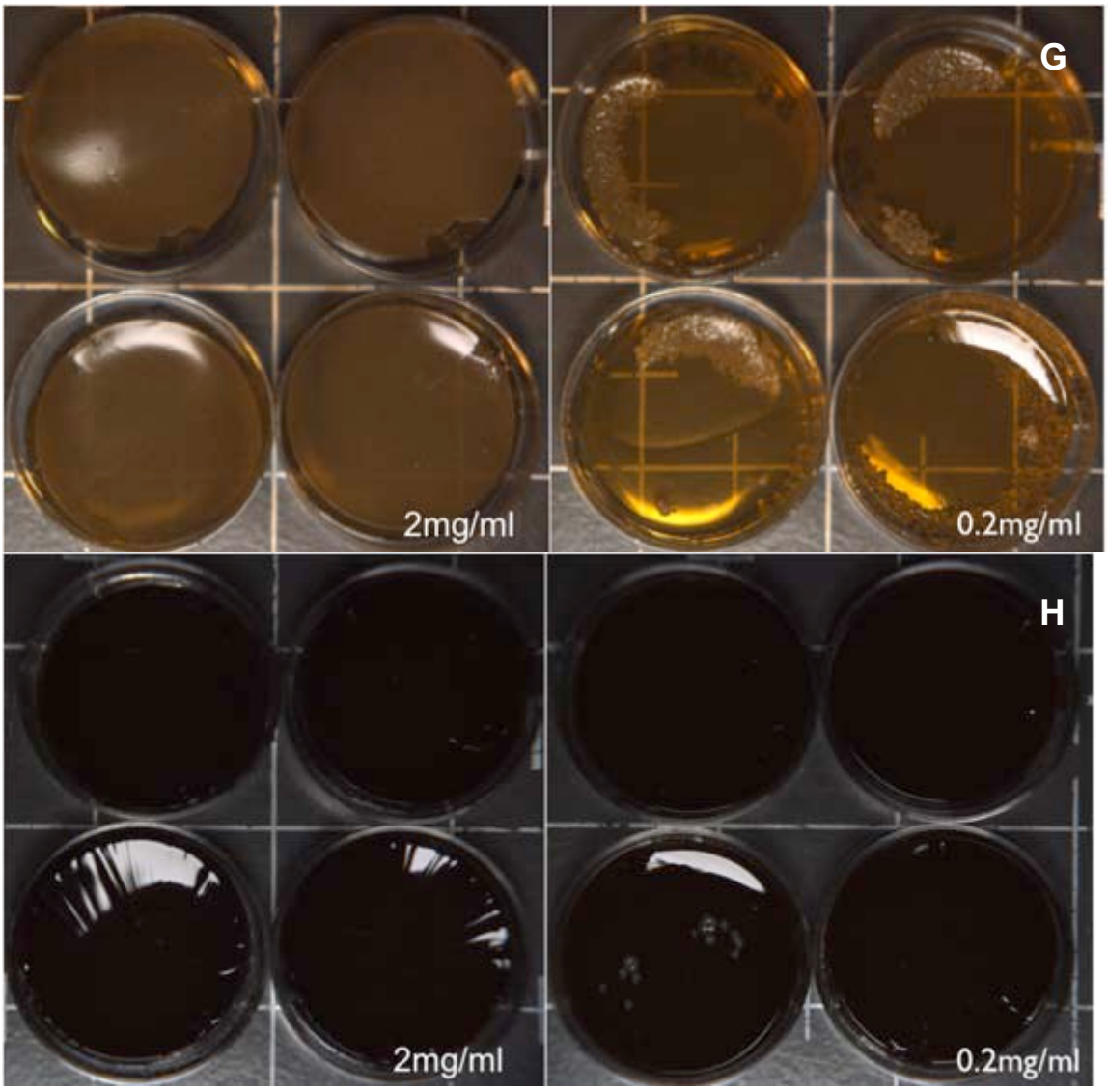

Figure B-0-2: Full trial of 35 mm agar plates challenged with *E. coli* for Control agar (full growth) (A), 250 µm diameter (B), 45 µm diameter (C), 5-8 µm diameter (D), 150 nm diameter (E), 100 nm diameter (F), BioGate HyMedic 4000 (G), and Zr2k particle (H).

C: Matlab Scripts for Modeling Ag^+ Release.

1. Model code for calculating E_a values from Zhang et al.

```
%Ag Ion Release inµgrams/l
T=310.15; %Temperature in kelvin (37C)
kb=1.38*(10^(-23)); %Boltzman constant in (J/K)
Pd=10.5; %Density (g/cm^3)
r=80*10^(-7); %radius of Ag particle (cm)
Ea=-5.4985*(10^-20); %Ea= value based on calculating from Zhang et al. paper %Activation Energy (J)
%Ea for Ag bromide is 0.29?0.33 eV or (0.29?0.33)*1.602e?19 J
Mb = 2*15.999*1.660538921*(10^-24); %molecular weight of dissolved O2  (g)

DO = 0.0078; %Dissolved oxygen concentration(0.0078 in zhang et al.) (g/l)

pH=7; %5.6 in the Zhang et al.
H = (1/(10^pH))*(1.660538921*(10^-24))*1.00794*(6.0221415*10^23);
%(mol/l)  mol to grams = 6.0221415◊10^23 (molecules) * 1.00794 (atomic mass
%units for H+)*1.660538921◊10^?24 (AMU to g conversion)

%Agint = 0.0006; %Initial Concentration of Ag (g/l)
%Agint = 0.000045038; %(g/l)
Agint = 45.038; %fitted from Zhang et al. was 45.038 (microgramsg/l)
a=0.75*(((8*kb*T)/Mb)^0.5)*(Pd^(-1))*exp((-Ea)/(kb*T))*(r^-1)*(DO^0.5)*(H^2);
%a=0.0487;
%b=-3.80751;


Ag = zeros(1,2);

Ag1=0;


for t=1:1:400 %units is currently hours (hrs)



   Ag1=Agint*(1-exp(-a*t));
   %Ag1=Agint-exp(b-a*t);


   Ag(t,2) = Ag1;
   Ag(t,1) = t;

end

figure
```

```
hold on
plot(Ag(:,1),Ag(:,2),'Color','g','LineWidth',4);
%
% legend('x=3','x=2.5','x=2','x=1.5','x=1','x=0.5','x=0','Location','South');
title('Diffusional Release of Ag ions from PEEK  ','fontsize',20);
xlabel('Time (Hr)  ','fontsize',20);
ylabel('Concentration of Ag Ions Release (micrograms/l)  ','fontsize',20);
```

2. Code for complete idealized model for Ag^+ release from PEEK matrix with water diffusion incorporation

```
%Higuchi Equation Parameters
C = 0.142; %(units = g/ml) Based on Concentration of Nano-Ag in PEEK at 10w/w%
D = 0.000044; %units Cm^2/h DIffusion coefficient of ion out of polymer (baed on desporption coefficient of water
%Cp = 0.00646;  %(units = g/ml) Solubility of Drug in polymer
A = 4.32; %(cm^2) total surface are of the slab used in initial elution trials


%Ag Ion Creation Parameters
T=310.15; %Temperature in kelvin
kb=1.38*(10^(-23)); %Boltzman constant in (J/K)
Pd=10.5; %Density (g/cm^3)
r=80*10^(-7); %radius of Ag particle (cm)
Ea=-5.4985*(10^-20); %Ea= value based on calculating from Zhang et al. paper %Activation Energy (J)
Mb = 2*15.999*1.660538921*(10^-24); %molecular weight of dissolved O2  (g)
DO = 0.004*0.009;%0.4% of zhang et al value for Dissolved oxygen concentration(0.0078 in zhang et al) (g/l)
pH=7.2; %5.6 in the Zhang et al.
H = 0.004*(1/(10^pH))*(1.660538921*(10^-24))*1.00794*(6.0221415*10^23); %This is 0.5percent of the H ions in the pH
%(mol/l)  mol to grams = 6.0221415◊10^23 (molecules) * 1.00794 (atomic mass
%units for H+)*1.660538921◊10^?24 (AMU to g conversion)
%Agint = 0.0006; %Initial Concentration of Ag (g/l)
Agint = 0.142*(10^9); %(micrograms/l) this is now based on concentration of Ag within PEEK by theoretical density


%WATER DIFFUSION BY MASS
D2=0.0044;   %diffusion coefficient  D(brine)= 4.4*10^-3 (mm^2/h)
l=2; %thickness of sample in mm.



Mass = zeros(1,2);

Mass1=0;
```

```
for t=1:1:600 %units is currently hours (hrs)

            MassDiffusion=0;

                for n=0:1:100; %zero values produced beyond 5000

                 MassDiffusion = MassDiffusion + (1/((2*n)+1)^2)*exp((-
D2*t/(l^2))*(pi^2)*((2*n+1)^2));
                end


            x1 = 1-(8/(pi^2))*MassDiffusion;

   a=0.75*(((8*kb*T)/Mb)^0.5)*(Pd^(-1))*exp((-Ea)/(kb*T))*(r^-1)*((x1*DO)^0.5)*((x1*H)^2);

   Cp=(Agint*(1-exp(-a*t)))/(10^9); %The "*10^9 was added to convert (micrograms/l) to g/mL

   Mass1 =((D*t*Cp*((2*C-Cp)))^(0.5))*A/(10^-9);


   Mass(t,2) = Mass1;
   Mass(t,1) = t;
end
figure
hold on
plot(Mass(:,1),Mass(:,2),'Color','g','LineWidth',4);
%
% legend('x=3','x=2.5','x=2','x=1.5','x=1','x=0.5','x=0','Location','South');
title('Diffusional Release of Ag from PEEK ','fontsize',20);
xlabel('Time (Hr)','fontsize',20);
ylabel('Mass of Ag Release (nanograms) ','fontsize',20);
```

D: Additional model fits for Ag^+ release from Ag particles

If the concentration is increased to 2000 µg/l and held constant with a pH of 7, a more linear fit is observed. E_a values for nano and µAg were **-6.469e-20J** and **-6.258e-20J** respectively. This value is still higher than original fitted value for the data of -5.5e-20J.

For nanoAg
Coefficients (with 95% confidence bounds):
Ea = -6.469 (-6.541, -6.397)

Goodness of fit:
SSE: 1.419e+04
R-square: 0.6369
Adjusted R-square: 0.6369
RMSE: 33.04

For µAg
Coefficients (with 95% confidence bounds):
Ea = -6.258 (-6.304, -6.213)

Goodness of fit:
SSE: 2270
R-square: 0.8854
Adjusted R-square: 0.8854
RMSE: 13.21

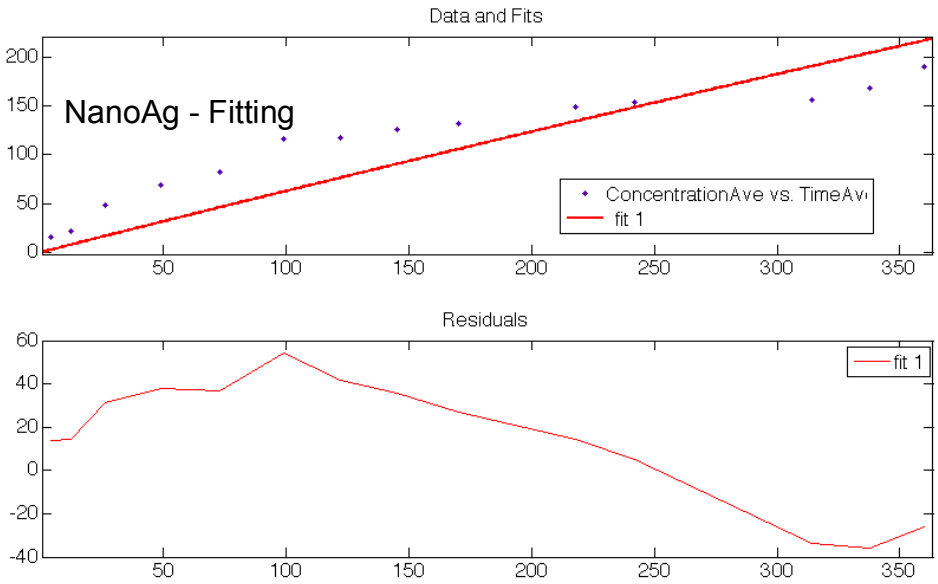

Figure D-0-1: Model fit for nanoAg elution data when $[Ag]_{initial}$ is held constant.

1. Fitting for nanoAg ion release

Model was fitted for nanoAg elution, so the limit ($[Ag]_{Initial}$) was set to 200 µg/l. This was first attempted by using all the measured values except the pH was set to 6. (A pH of 6 was chosen based on the original data from Zhang et al.) E_a was varied with a starting point of -5.5e-20. E_a starting point was actually set to -5.5 while the equation was filled with "E_a*10^-20" because the matlab curve fitting tool was not able to perform iterations for such low numbers.

Fit for pH of 6:

General model:

```
f(x) = 200*(1-exp(-(21502.43853*(exp((-Ea*10^(-20))/(4.28007e-21)))*(((1/(10^6)
       )*(1.660538921*(10^-24))*1.00794*(6.0221415*10^23))
       ^2))*x))
```

Coefficients (with 95% confidence bounds):

Ea = -5.421 (-5.471, -5.37)

Goodness of fit:

SSE: 1647
R-square: 0.9579
Adjusted R-square: 0.9579
RMSE: 11.25

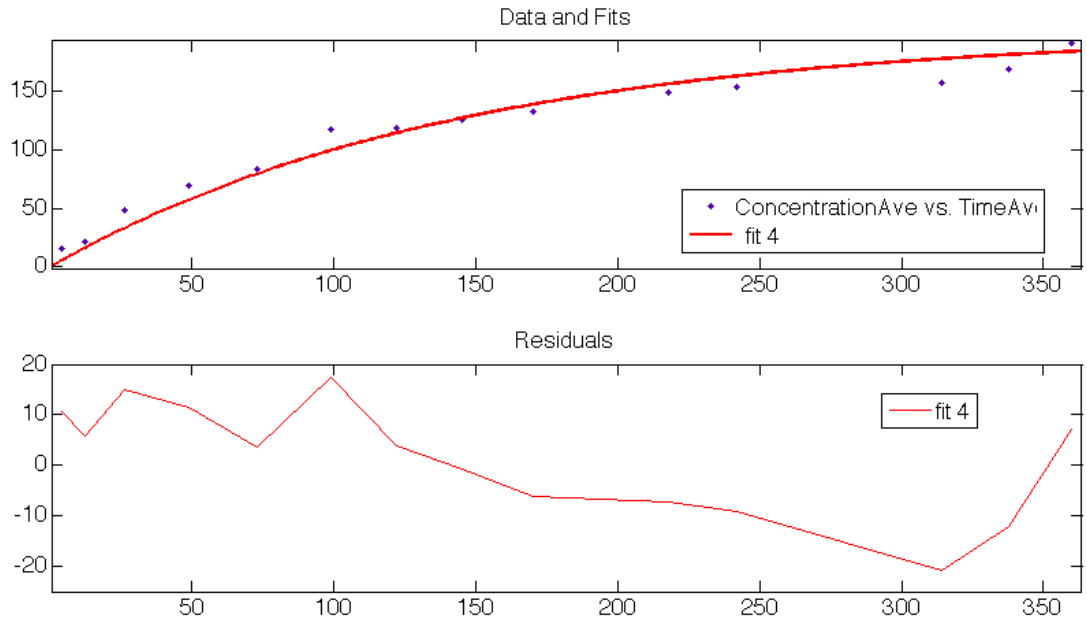

Figure D-0-2: Alternative Model fit for nanoAg elution data for when $[Ag]_{initial}$ is held constant and pH is 6.

The model is then allowed to fit for both $[Ag]_{Initial}$, Ea, and pH values. The [Ag] is allowed to be fitting due to similar problems that were observed in Zhang et al.'s study, where to fit the model, Zhang observed that the values of the initial concentration had to be lowered. This is not only because of the aggregation of particles, but also because the Ag particles did not completely dissolve during testing

If pH and $[Ag]_{initial}$ are allowed to fit with pH start point of 6, and [Ag] of 200:

General model:

```
f(x) = a*(1-exp(-(21502.43853*(exp((-Ea*10^(-20))/(4.28007e-21)))*(((1/(10^pH)
       )*(1.660538921*(10^-24))*1.00794*(6.0221415*10^23))
       ^2))*x))
```

Coefficients (with 95% confidence bounds):

Ea = -5.549 (-1.981e+06, 1.981e+06)
a = 176.1 (130.3, 221.8)
pH = 6 (-1.005e+06, 1.005e+06)

Goodness of fit:
SSE: 1002
R-square: 0.9743
Adjusted R-square: 0.9697
RMSE: 9.545

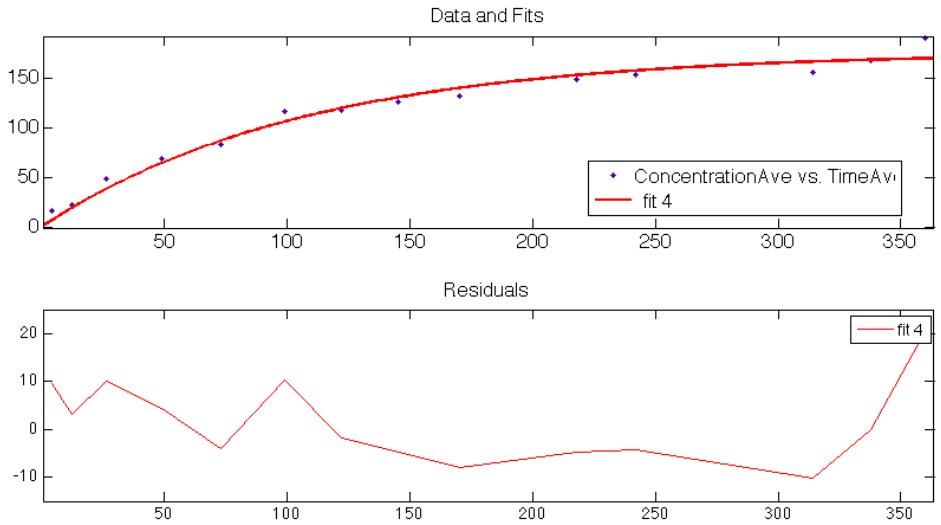

Figure D-0-3: Alternative Model fit for nanoAg elution data for when $[Ag]_{initial}$ and pH are variables.

2. Fitting for µAg ion release

Model was fitted for µAg elution, so the limit $[Ag]_{initial}$ was set to 110 µg/l (based on the upper limit of elution). This was first attempted by using all of the measured values except the pH was set to 6. The E_a was varied with a starting point of -5.5e-20. E_a starting point was actually set to -5.5 while the equation was filled with "E_a*10^-20" because the matlab curve fitting tool was not able to perform iterations for such low numbers.

Fit for pH of 6:
General model:

f(x) = 110*(1-exp(-(21502.43853*(exp((-Ea*10^(-20))/(4.28007e-21)))*(((1/(10^6)
)*(1.660538921*(10^-24))*1.00794*(6.0221415*10^23))
^2))*x))
Coefficients (with 95% confidence bounds):
Ea = -5.474 (-5.54, -5.409)

Goodness of fit:
SSE: 801.6
R-square: 0.9595
Adjusted R-square: 0.9595
RMSE: 7.853

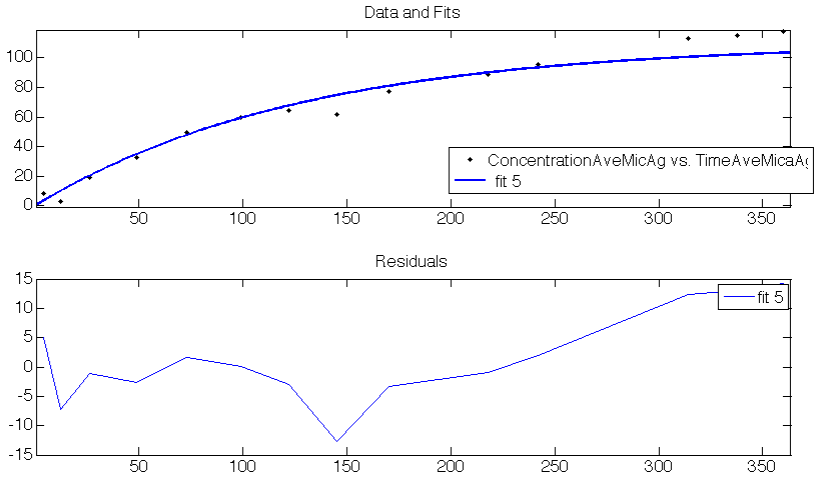

Figure D-04: Alternative Model fit for μAg elution data for when $[Ag]_{initial}$ is held constant and pH is 6.

The model is then allowed to fit for both $[Ag]_{initial}$, E_a, and pH values. The [Ag] is allowed to be fitting due to similar problems that were observed in Zhang Et al.'s study, where to fit the model, Zhang observed that the values of the initial concentration had to be lowered. This is due not only because of the aggregation of particles, but also because the Ag particles did not completely dissolve during testing

If pH and initial [Ag] are allowed to fit with pH start point of 6, and [Ag] of 90:

General model:
f(x) = a*(1-exp(-(21502.43853*(exp((-Ea*10^(-20))/(4.28007e-21)))*(((1/(10^pH)
)*(1.660538921*(10^-24))*1.00794*(6.0221415*10^23))
^2))*x))
Coefficients (with 95% confidence bounds):

Ea = -5.38 (-4.159e+06, 4.159e+06)
a = 140.4 (-3.837, 284.6)
pH = 6.053 (-2.11e+06, 2.11e+06)

Goodness of fit:
SSE: 277.1
R-square: 0.986
Adjusted R-square: 0.9835
RMSE: 5.019

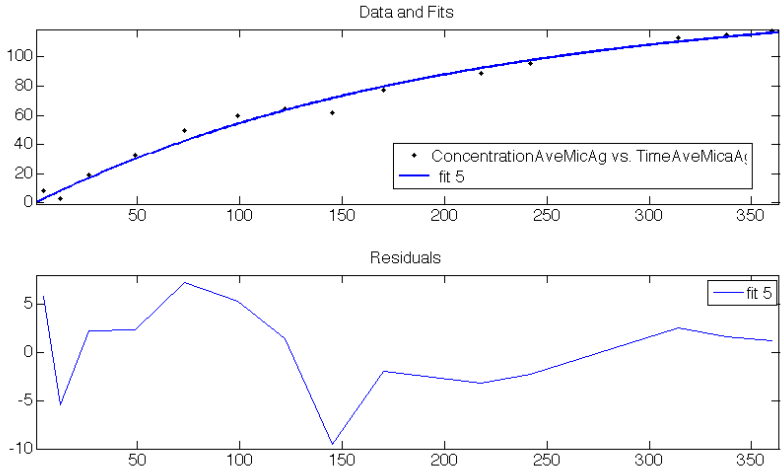

Figure D-0-5: Alternative Model fit for μAg elution data for when $[Ag]_{initial}$ and pH are variables.

E: Ag^+ release profiles for varying Ag loading with alternate E_a values

a. NanoAg model for E_{a1} (6.469e-20J) – fitted with Constant $[Ag]_{initial}$

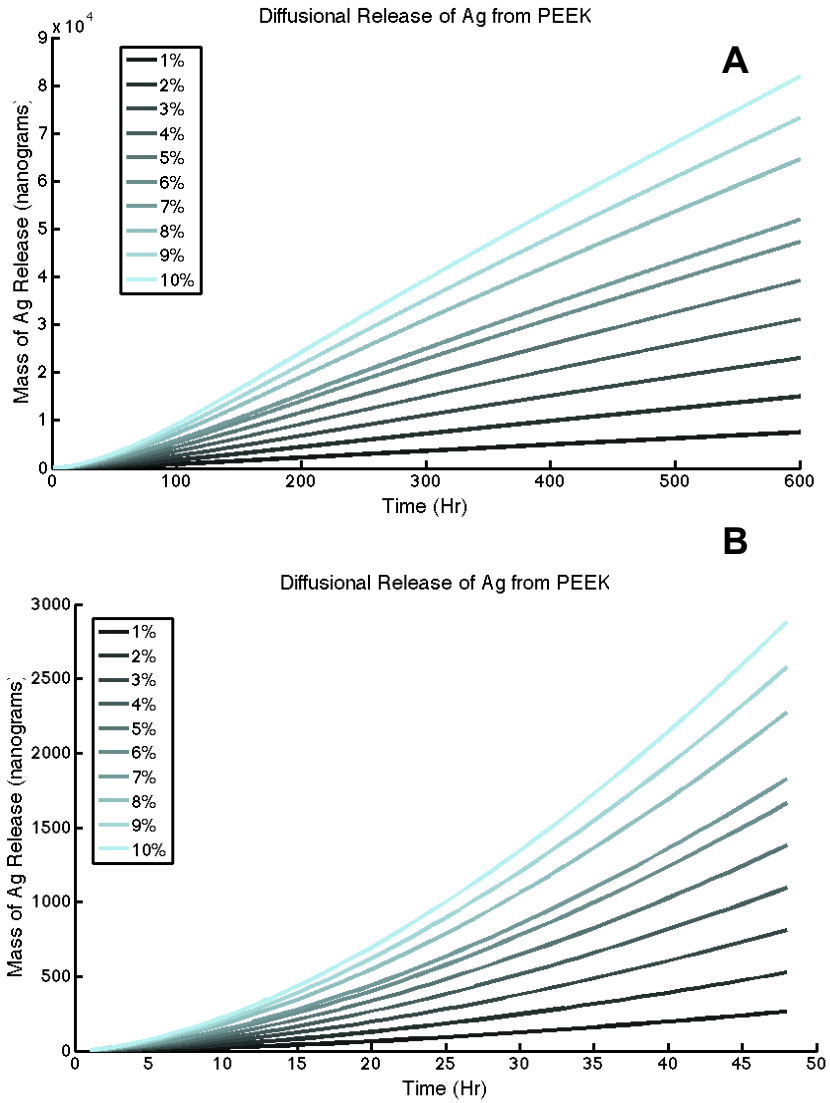

Figure E-0-1: Diffusional release profiles for nanoAg composite material at 50hr (A) and 600hr (B) for E_{a1} (6.469e-20J).

b. µAg model for E_{a1} (6.258e-20J) – fitted with Constant $[Ag]_{initial}$

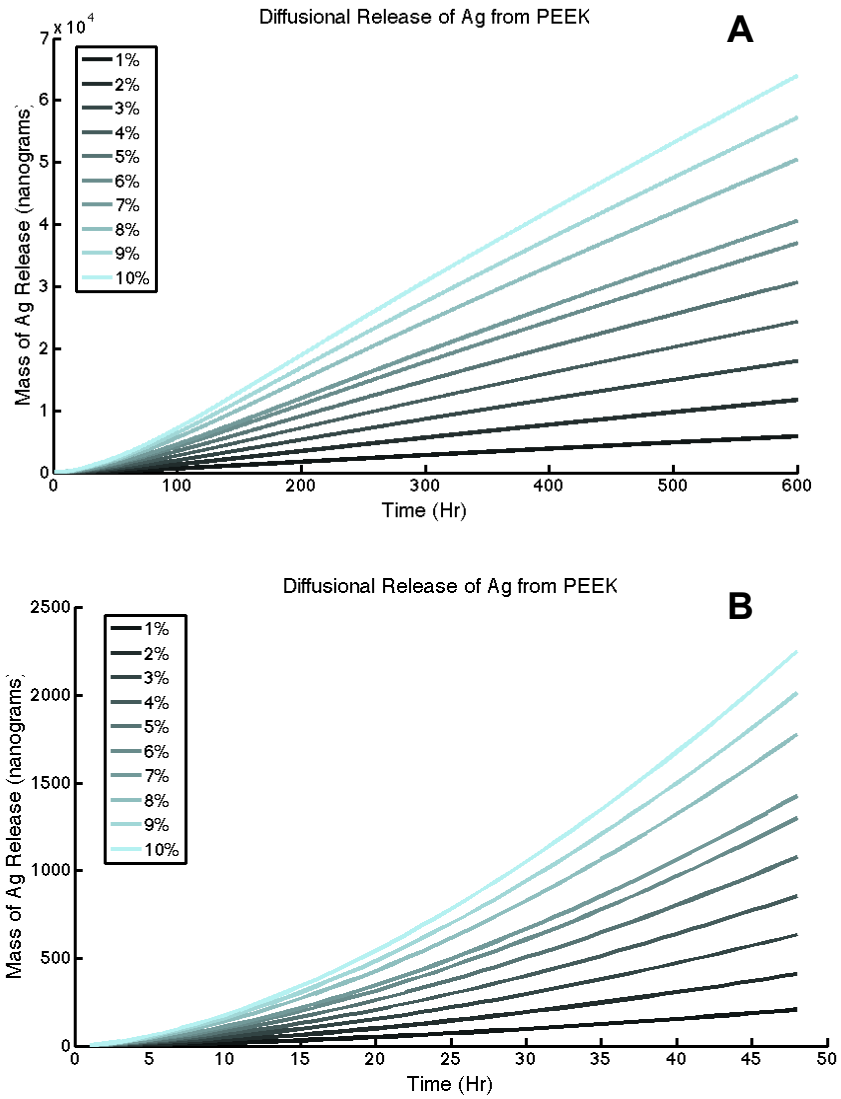

Figure E-0-2: Diffusional release profiles for μAg composite material at 50hr (A) and 600hr (B) for E_{a1} (6.258e-20J).

F: Elution predictions from model using alternative activation energy values

NanoAg

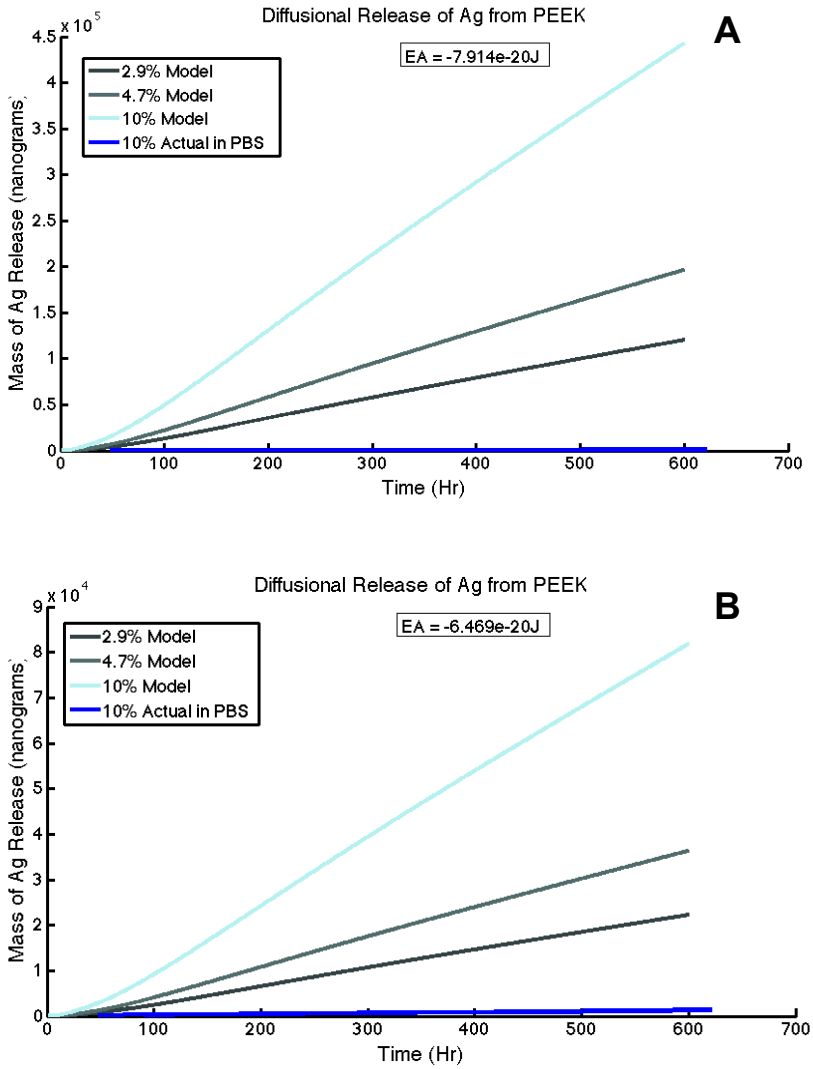

Figure F-0-1: Experimental elution data was compared to model predictions for 2.9, 4.7, and 10% nanoAg loading ratios for E_{a2} (-7.914e-20J) and E_{a1} (-6.258e-20J).

1. µAg

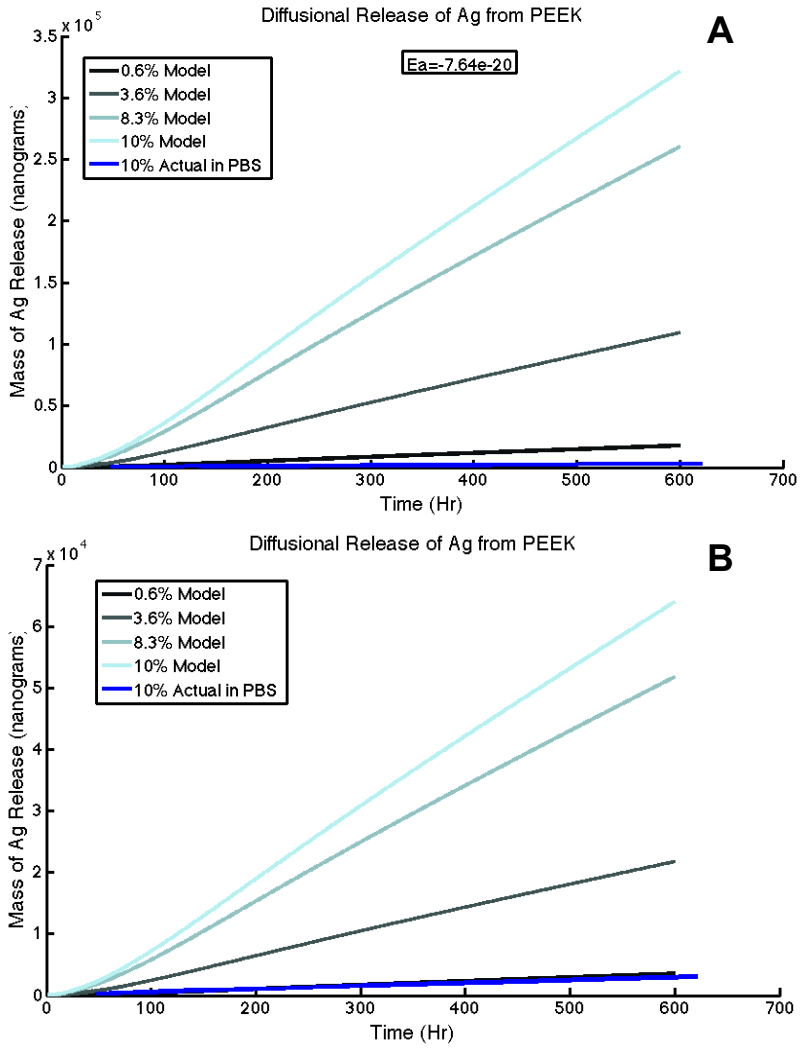

Figure F-0-2: Experimental elution data was compared to model predictions for 0.6, 3.6, 8.3 and 10% nanoAg loading ratios for E_{a2} (-7.64e-20J) and E_{a1} (-6.469e-20J)

Vita

David Joseph Jaekel, M.S.

Ph.D. (in process), Biomedical Engineering, Drexel University, 2012
M.S., Biomedical Engineering, Michigan State University, 2011
B.S., Mechanical Engineering, Michigan State University, 2003

European Society of Biomaterials Best Student Speak Award, 2010, Graduate Fellowship, 2007

Publications

Jaekel DJ, Davidson HM, Hickok NJ, Kurtz, SM, Fabrication and Analysis of Silver-PEEK Composite Biomaterials, Biomaterials, 2012 (*in review*)

Jaekel DJ, Ong KL, Lau EC, Kurtz, SM, The Epidemiology of Total Joint Arthroplasty Infections, in Rihard Trebše, Infected Total Joint Arthroplasty: The Algorithmic Approach, Springer; 2012 (*in review*)

Jaekel DJ, Klein GR, Day JM, Levine HB, Parvizi J, Austin M, Kurtz SM, Dynamic Cement-on-Cement Knee Spacers Improve Function and Activity During Two-Stage Exchange, Clinical Orthopaedics and Related Research, 2012 April 4 (*Epub ahead of print*)

Reitman M, Jaekel DJ, Siskey R, Kurtz S, 2011 Morphology and Crystalline Architecture of Polyaryletherketones, in Steven Kurtz Ph.D., PEEK Biomaterials Handbook, New York, Elsevier; 2011, 49-60,

Rochford E, Jaekel D, Hickok N, Richards R, Moriarty T, Poulsson A. Bacterial Interactions with Polyaryletheretherketone. In: Kurtz SM, editor. PEEK Biomaterials Handbook. New York: Elsevier; 2011, 93-117.

Jaekel DJ, MacDonald DM, Kurtz SM, Characterization of PEEK biomaterials using the small punch test, Journal of the Mechanical Behavior of Biomedical Materials, 4 (7), Oct 2011, 1275-1282

Jaekel DJ, Medel FJ, Kurtz SM. Validation of Crystallinity Measurements of Medical Grade PEEK Using Specular Reflectance FTIR-microscopy. Society of Plastics Engineers Annual Technical Conference. Chicago: Society of Plastics Engineers; 2009.